The Composition of Dense Matter from Neutron Star Observations

A Dissertation Presented for the

Doctor of Philosophy

Degree

The University of Tennessee, Knoxville

Satyajit Roy

May 2025

dedicated to my parents.
Their love and support made this work possible.

Acknowledgments

I would like to thank my advisor Dr. Andrew Steiner for his immense guidance throughout my career at UTK. His advice has made me not only a better physicist but a better person as well.

I am sincerely grateful to my colleagues in our research group and for the friends that I have made here who were always there for me in my time of need. I had great discussions on both physics and life with them and have made some great memories that I will cherish. Especially Rizwanul and Anik, I am glad we are friends.

My committee members Dr. Mike Guidry, Dr. Bronson Messer, Dr. Lawrence Lee, and Dr. Vasileious Maroulas, thank you for your support and helpful discussions, and a special thanks to Dr. Dany Page for all his advice and suggestions for my work.

I am thankful to The Department of Physics and Astronomy of UTK for giving me an opportunity to hone my skills. I cannot emphasize enough the support that I have gotten during my time here from Chrissane Romeo, Tamria Cameron, and especially Showni Crump. Shwoni, I will always remember your kind words.

I would like to thank my family for being supportive of my decisions and I could not have made it without their trust and encouragement. Last but not least, my cat Yuumi was always there to lift my spirits.

This work has been supported by the National Science Foundation under grant no. PHY2103680 and PHY155487.

Abstract

Neutron stars are unique probes of the physics of hot and dense matter. Neutron star observations have begun to provide important constraints on the dense matter equation of state, e.g. the relationship between pressure and energy density. While there are few previous constraints on the composition of dense matter, we show that, presuming a model of dense matter that does not contain any exotic particles, observations of neutron star cooling constrain the number of protons per baryon to exceed ten percent at twice the density in the center of a nucleus. We present a combined analysis of the thermal evolution of isolated and accreting neutron stars and include nuclear measurements, mass-radius measurements of low-mass X-ray binaries, NICER and LIGO results, and the PREX experiment to constrain the equation of state and superfluidity inside a neutron star. Our analysis suggests that "enhanced cooling" methods are necessary for some neutron stars to explain the current multi-messenger observations. We briefly discuss the importance of combining different equations of state and the Modular Unified Solver of the Equation of State framework to predict zero temperature beta equilibrium matter and its future implications. Finally, we offer a short overview of how machine learning-based estimators could be utilized in nuclear astrophysics. We find that estimating neutron star cooling can significantly improve the efficiency of neutron star thermal evolution analysis. Finally, we propose some ideas that can be useful in future studies.

Table of Contents

1 Introduction **1**
- 1.1 Neutron Stars . . . 2
- 1.2 Neutron Star Structure and Composition . . . 2
- 1.3 Tolman-Oppenheimer-Volkoff (TOV) Equations . . . 4
- 1.4 Equation of State (EoS) . . . 5
  - 1.4.1 Relativistic Mean-Field EoS . . . 7
- 1.5 Neutron Star Cooling . . . 10
  - 1.5.1 Specific Heat . . . 16
  - 1.5.2 Accretion Effects . . . 17
- 1.6 Motivation . . . 18

2 Methodology **19**
- 2.1 The EoS and Superfluidity Parameters . . . 19
- 2.2 Constructing The Likelihood Function . . . 20
  - 2.2.1 Nuclear Structure . . . 20
  - 2.2.2 Multi-Messenger Astronomy . . . 21
- 2.3 Model Summary . . . 34
- 2.4 Bayesian Inference . . . 37
- 2.5 Kernel Density Estimation . . . 37

3 Results **39**
- 3.1 Discussion . . . 46

4 Modular Unified Solver of the Equation of State (MUSES) **48**
- 4.1 Calculation Engine . . . 48
- 4.2 Crust Density Functional Theory . . . 49
  - 4.2.1 Crust-DFT Integration . . . 49

5 Status and Outlook **52**
- 5.1 Machine Learning for Astrophysics . . . 52

5.1.1 Gaussian Process Regression . . . 52
5.1.2 Decision Tree Regression . . . 54
5.1.3 Neural Network Regression . . . 56
5.2 Preliminary results . . . 59
5.3 Future work . . . 64

6 Conclusions **65**

Bibliography **66**

Appendices **80**
A The Neutron star cooling code . . . 81
B Markov Chain Monte Carlo . . . 83
B.1 Metropolis-Hastings Algorithm . . . 84
B.2 Affine Invariant Sampling . . . 84
B.3 Ensuring Convergence . . . 85
C Extra plots . . . 87
D INS Observations . . . 93
E OpenAPI 3.0 For Crust-DFT . . . 95
F Pion Integration in Crust-DFT . . . 96
F.1 Pion Properties . . . 100

Vita **102**

List of Tables

1.1 The different neutrino emission processes and their emissivities [89]. The coefficients R's are control functions to incorporate the effects of pairing. $T9 \equiv T/(10^9\ \mathrm{K})$, efficiency of how fast the process cools the star is on the right side. 15

2.1 Parameter set for our MCMC and their brief descriptions 36

1 INS observations from Ref. [99]. 93

2 INS observations from Ref. [99] continued. 94

List of Figures

1.1 Simple illustration of a neutron star structure. In summary, NSs are composed primarily of neutrons in their core, a solid crust made of neutron-rich nuclei surrounding the core, and a thin atmosphere of lighter elements [60]. The composition of the inner core is still unknown. (A) shows the superfluidity in the crust, (B) shows a diagram of the various phases of matter in the crust and the transition into the core, and (C) has the structure of the outer core. 3

1.2 Different gap models (left axis) and the critical temperatures (right axis) as a function of the crust neutron Fermi momentum from Figure 9 in Ref. [144]. The crust-core transition is denoted as the vertical dotted line. The uncertainties in these models are by a factor of 2. 13

2.1 Theoretical cooling curves ($L_\gamma^\infty - t$) of isolated Neutron stars from Ref. [100] with observed age and luminosity data. Different mass values (denoted by different colors, noted at the bottom left of the figure) are used for multiple cooling curves. Non-accreted and accreted envelopes are in solid and dashed curves respectively. For superfluidity, the MSH+BS+TTav model is used with the BSk24 EoS. Arrows in the data points represent the upper limits of either luminosities or ages. With a fixed superfluidity and EoS, this model is not sufficient to explain stars on the top right quadrant of the figure. 23

2.2 A series of steady-state curves ($L_\gamma^\infty - \dot{M}$) for SXRTs from Ref. [47] using APR, HHJ, SLy4, and NL3 EoS with SFB-a-73 model for the superfluid gap. Observed luminosities and accretion rates are from Refs. [53, 13]. The hottest SXRT Axl X-1 is denoted by the cross on the upper right quadrant and the coldest SXRT SAX J1808 is the enlarged solid arrow (dotted arrows underneath show old data). Without enhanced cooling, it is hard to explain the colder stars. 26

2.3 Mass-radius relationship of the quiescent low mass X-ray binary stars in the globular clusters from Ref. [120]. The density plots show the hydrogen atmosphere on the left and the helium atmosphere on the right. The contours show 68%, 90%, and 99% confidence intervals. The helium atmosphere supports a larger radius. 29
2.4 Quiescent low mass X-ray binary stars from [120]. The QLMXB in ωCen globular cluster only has hydrogen atmosphere data available. 30
2.5 Mass-radius relationship of the quiescent low mass X-ray binary star X7 from Ref. [120] in the upper half with hydrogen atmosphere on the left and helium atmosphere on the right. Lower panels are from the NICER stars PSR J0030+0451 [104, 76] and PSR J0740+6620 [105, 77] both with hydrogen atmospheres. 31
2.6 Probability distribution of mass ratio q and tidal-deformability $\tilde{\Lambda}$ of GW170817 [2] using Kernel density estimation [5]. 33

3.1 Cooling curves and their 68% credible intervals for the isolated neutron stars (panels 1-11). The luminosities and ages inferred from observations are given, along with the bands for the posterior distributions. The color of the bands gives the posterior neutron star mass. Most of the stars cool via slower cooling processes and have a cooling curve that is flatter in the early stages. 40
3.2 Some stars, like J0007 (panel 4) and B1727 (panel 7) are cooling partially via the direct Urca process and thus cool much faster at earlier times. Panel 12 shows the SXRT luminosity as a function of their inferred time-averaged accretion rate. 41
3.3 The range between the minimum and maximum proton fraction of the KDE training set and 68% credible intervals for the number of protons per baryon, x_p, as a function of the baryon number density n_B. We find a very tight constraint on the composition of dense matter. 42
3.4 Panel (1) shows the posterior distribution for the maximum critical temperatures. Panel (2) shows the posterior distributions for the remaining superfluid parameters. Panel (3) shows the posterior for the specific heat as a function of mass and panel (4) shows the correlation between neutron star radius and specific heat of a 1.4 $M_\odot$ neutron star. This correlation is broken for higher masses because of the neutron triplet superfluid. 43

3.5 Approximate posterior distributions for the mass and luminosity of each of the INSs (triangles) and SXRTs (circles) with uncertainties. η represents the amount of light elements in the envelope. Below 1.4 $M_\odot$ luminosity has less dependence on stellar mass. Above 1.4 $M_\odot$, enhanced cooling processes are active, and the luminosity drops as a function of mass almost linearly. 44
3.6 The posterior INS neutron star mass function as approximated by a kernel density estimator applied to the INS mass posteriors. A bulk of NS is around the canonical mass of 1.4 $M_\odot$. The colder NS supports a larger mass ~ 2 $M_\odot$. 45

4.1 Speed of sound comparison from different EoS models of Crust-DFT. The Fiducial model has a kink in the speed of sound near 10^{-2} fm^{-3} which corresponds to the appearance of nuclei. The large $M_{\rm max}$ model has a higher speed of sound in lower densities, resulting in supporting a larger maximum mass. 51

5.1 A Decision tree example [Image Credit: Quelle: FU Berlin, RESEDA, https://blogs.fu-berlin.de/reseda/random-forest]. 54
5.2 A DNN with one hidden layer example [Image Credit: https://scikit-learn.org/1.5/modules/neural_networks_supervised.html] 58
5.3 A Decision tree regression comparison of predicted vs actual likelihood of INS. While the predicted values follow the real function's overall trend, the individual inaccuracies are large and affect the overall likelihood function negatively. This is due to the large number of INS in our population whose individual likelihoods add up to the sum. 60
5.4 A Decision tree regression comparison of predicted likelihood of all low mass X-ray binaries to computed likelihood. The likelihood is computed from partially known mass-radius relations. This is a far more accurate description of the likelihood function due to the smaller population of QLMXBs. 61
5.5 A Decision tree regression comparison of the radius of a 1.4 $M_\odot$ star predictions vs. the radius from TOV equations. 62
5.6 Computed cooling curves for 1, 1.4 and 2.0 $M_\odot$ stars. Note that 1.4 $M_\odot$ already has direct-Urca depending on the EoS making the cooling faster at times. 63
5.7 Predicted cooling curves 1, 1.4, and 2.0 $M_\odot$ stars. Stars with a mass on either end of the mass grid are quite accurate. Most of the inaccuracies lie in the cooling curves for 1.4 and 1.6 $M_\odot$ stars where the onset of direct Urca is sensitive to the EoS parameterizations. 63

1 Posterior mass-radius distribution of QLMXBs from the globular clusters 6397, M13, and M28. Left panels denote hydrogen atmospheres and the right panels are helium atmospheres. 87
2 Posterior mass-radius distribution of QLMXBs from the globular clusters ω Cen and X7. Left panels denote hydrogen atmospheres and the right panel is helium atmospheres. 88
3 Posterior mass-radius distribution of QLMXBs from globular clusters 6304 and M30 and the NICER stars J0030 and J0740. Here only M30 has a helium atmosphere. J0030 and J0740 have hydrogen atmospheres and 6304 prefers a hydrogen atmosphere from our analysis. 89
4 Posterior distribution of QLMXB atmospheres. 6304 (blue line) predominantly prefers a hydrogen atmosphere whereas M30 (purple line) and 6397 (orange dashed line) prefer helium atmospheres. 90
5 Posterior nuclear properties against baryon densities. 91
6 LIGO posterior for mass ratio q and tidal-deformability $\tilde{\Lambda}$. Here the stellar masses values of the NS-NS binary are quite close to one another. The tidal deformability $\tilde{\Lambda}$ has a value near 800 which is the low-spin prior from Ref. [2]. 92
7 Phase shift vs Center of mass momentum 98

Chapter 1

Introduction

Neutron stars (NS) are one of the most fascinating remnants of stellar evolution. The concept of NS began with the understanding of nuclear physics and the behavior of matter under extreme conditions. After Landau predicted their existence in 1931 [1] (even before the discovery of neutrons in 1932 by Chadwick), physicists explored the possibility of neutron degeneracy pressure counteracting the gravitational collapse of a star [36, 86]. Baade and Zwicky proposed in 1934 that a massive star can undergo a violent explosion process that can create conditions suitable for forming a compact star made mostly of neutrons with densities far above the density of terrestrial nuclear matter.

It was not until 1967 when the first NS was identified indirectly through the discovery of pulsars by Burnell and Hewish [54]. They observed regular radio pulses coming from a specific region in the sky. It was initially thought to be a signal from extraterrestrial life, earning it the nickname "Little Green Men." It was later determined to be the rotating NS PSR B1919+21 (also known as the Crab Pulsar). These intermittent signals originated from the polar caps of the NS as strong electromagnetic radiation due to the star's magnetic field. The rotation of the star was responsible for the signal's periodic nature.

Following this discovery, a series of orbital (Einstein, EXOSAT, ROSAT, ASCA, Hubble, etc.) and ground-based observatories (ESO-NTT, Keck, etc.) with X-ray and optical telescopes have detected thousands of NSs throughout the next 30 years that have aided our understanding of NSs [143]. In particular, knowledge of equation of state (EoS) and matter behavior at nuclear densities, advanced significantly throughout the 1970s and 1980s. According to theories, NSs do not only contain neutrons but could also include unusual forms of matter like quark matter [22] and hyperons [6]. In the early 21st century, X-ray observatories like Chandra and XMM-Newton have shaped the theory of NS with new discoveries. A new era in astronomy began in 2017 when LIGO discovered gravitational waves from NS mergers [2]. Furthermore, new observational data from the Neutron Star Interior Composition Explorer (NICER) mission in recent years has put current EoS theories to the

test. Riley et al. (2019) estimated the parameters of the neutron star PSR J0030+0451 using NICER observations, providing information on its mass and radius that may constrain the EoS [104].

NSs have been an interesting playground for both theoretical and experimental physicists for nearly a century now. They are intriguing from a theoretical perspective as all the fundamental forces are at play here [128]. Furthermore, they are appealing to nuclear physicists, as they offer unique insights into the nature of dense and hot matter that can not be replicated in a lab [64]. It is possible to model realistic NS structure and evolution given an EoS for dense nuclear matter. On a microscopic level, the nucleon-nucleon interactions describe the state of matter, and macroscopically, the EoS describes the relationship between energy density and pressure of a star. Then conversely by observing NS macroscopic properties, we can more precisely converge to the correct EoS that describes dense matter. An accurate description of NS requires these models to be grounded in nuclear physics and constrained by multi-messenger observations.

1.1 Neutron Stars

Neutron stars are among the densest objects in the universe (second only to black holes). A massive star ($\sim 8-20\ M_\odot$ [64]) can no longer resist gravitational collapse when its nuclear fuel runs out. Protons and electrons combine to become neutrons as the core collapses in the resulting supernova explosion. A neutron star is created as a result of this process [8]. They are primarily composed of neutrons, justifying the moniker.

NSs possess several remarkable characteristics. They typically have a radius $\sim 10-12$ km and a mass of $\sim 1.0-2.0\ M_\odot$. They are extremely dense, ranging from 10^{14} to 10^{15} gm/cm^{-3} in a neutron star's core. A neutron star's surface has an enormous gravitational field $\sim 10^{11}$ times greater than Earth's. The structure of the star and the behavior of nearby matter are both impacted by its strong gravity.

1.2 Neutron Star Structure and Composition

As a spherically symmetric cosmological object, a neutron star can be sorted into different regions radially, making the problem of structure and composition essentially a 1-D problem. As we go from the surface of a neutron star to its core, density increases rapidly compared to the saturation density $\rho_0 \sim 2.8 \times 10^{14}$ gm/cm^{-3} and depending on the density and the matter state we can categorize the star into different regions. Fig. 1.1 shows neutron star structure at a glance. A neutron star is widely considered to have three distinct zones [40, 135, 66, 142, 46]; an atmosphere, a crust, and a core.

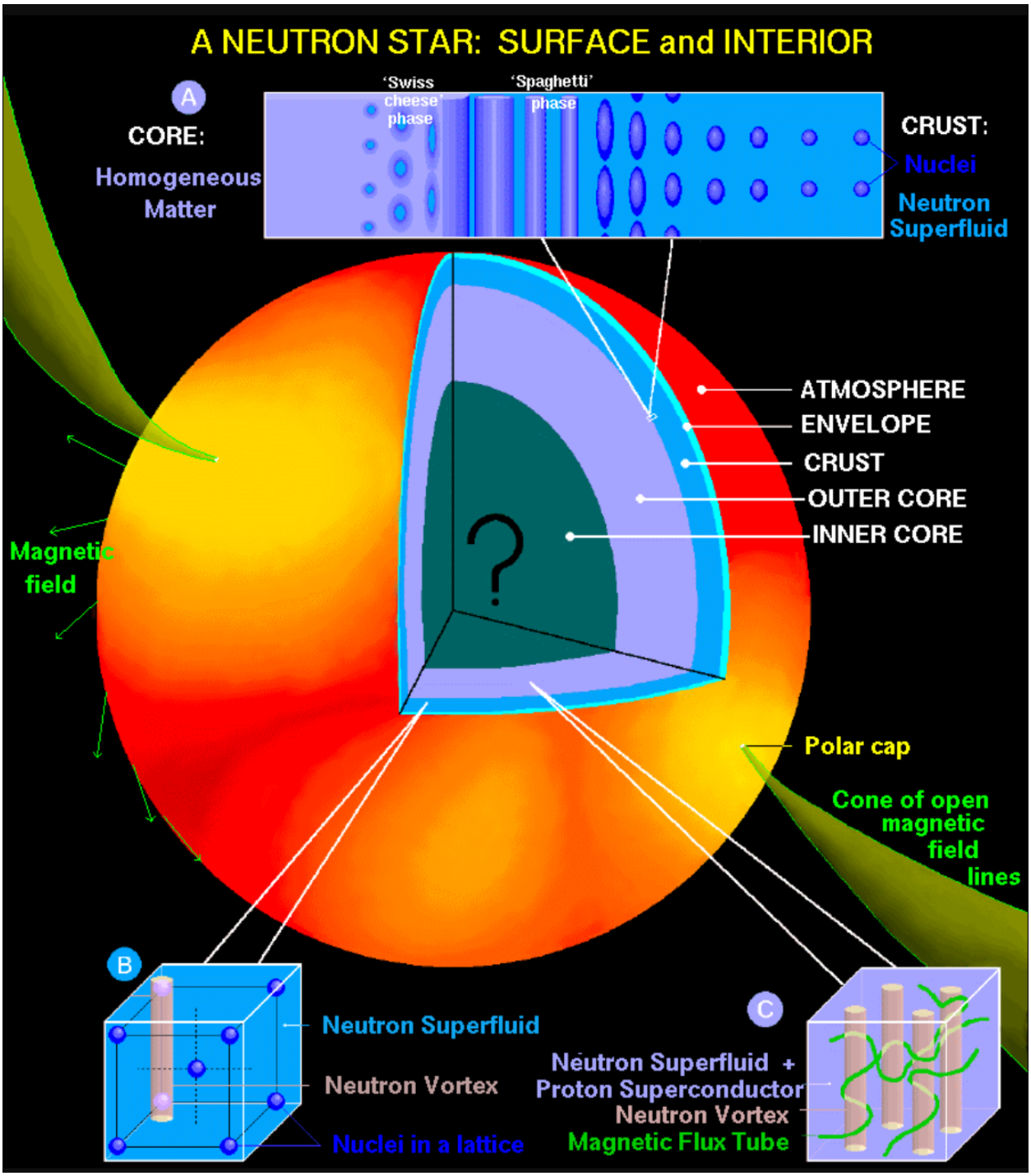


Figure 1.1: Simple illustration of a neutron star structure. In summary, NSs are composed primarily of neutrons in their core, a solid crust made of neutron-rich nuclei surrounding the core, and a thin atmosphere of lighter elements [60]. The composition of the inner core is still unknown. (A) shows the superfluidity in the crust, (B) shows a diagram of the various phases of matter in the crust and the transition into the core, and (C) has the structure of the outer core.

The atmosphere is the thinnest region at the surface (typically a few cm), and it is mostly made out of hydrogen, helium, or carbon. Some heavier elements may also be present depending on the stellar evolution, accretion, and sedimentation process after the supernova. This is the least dense region and this part of the star is responsible for the electromagnetic emissions we see through the X-ray detectors.

The crust is the region that resides between the atmosphere and the core, and it can be subdivided into two sections, an outer crust and an inner crust. The outer crust ($\sim$ 100 m) is made of nuclei and electrons. As we delve deeper into the star, with the increased density nuclei tend to become more neutron-rich via electron capture. At a density around $\rho_d \sim 4 \times 10^{11}$ gm/cm^{-3} neutrons start to drip from the nuclei and this marks the beginning of the inner crust. The inner crust ($\sim$ 1 km) has free neutrons along with neutron-rich nuclei and electrons [79, 95, 46, 142]. At the highest density of the inner crust ($\sim 0.5\rho_0$), we are left with a uniform nucleon fluid without any nuclei.

At the heart of the neutron star is a stellar core that can be classified into two sections. The outer core ($\sim 0.5\rho_0 - 2\rho_0$) is made out of mostly superfluid neutrons and a smaller fraction of protons and electrons [18]. Physics up to this point is well established and tested. Beyond this at densities $> 2\rho_0$, we enter uncharted territory in the inner core where conditions become even more extreme. The exact composition of the inner core is still a topic of research. It may contain exotic forms of matter such as hyperons (particles containing strange quarks) or even a quark-gluon plasma [66], where quarks are no longer confined within protons and neutrons. For a detailed summary see Refs: [140, 144].

The structure of neutron stars is heavily influenced by the equation of state (EoS), which describes how matter behaves under extreme densities and pressures. Various models exist, predicting different behaviors for neutron star matter. A soft equation of state predicts that neutrons can collapse under less pressure, resulting in lower maximum mass limits for neutron stars. Conversely, a stiff equation of state allows for greater stability and potentially higher maximum masses, enabling the existence of more massive neutron stars.

The stability of neutron stars is governed by the balance between gravitational collapse and neutron degeneracy pressure. Solving the internal structure of a NS requires solutions of the Tolman-Oppenheimer-Volkoff (TOV) equations.

1.3 Tolman-Oppenheimer-Volkoff (TOV) Equations

Neutron stars are relativistic spherically symmetric objects. Oppenheimer, Volkoff, and Tolman [86, 129] first solved the neutron star structure in 1939 by solving Einstein's equations for a relativistic static and spherically symmetric object.

In units where $c = 1$, a Schwarzschild metric captures the spherically symmetric nature of a NS.

$$ds^2 = -e^{2\phi(r)}dt^2 + e^{2\Lambda(r)}dr^2 + r^2 d\theta^2 + r^2 \sin^2\theta d\phi^2 \tag{1.1}$$

where θ and ϕ are the polar and the azimuthal angles respectively. The metric function Λ is

$$e^{2\Lambda} = \left(1 - \frac{2Gm}{r}\right)^{-1} \tag{1.2}$$

The other metric function, $\Phi(r)$ is the gravitational potential

$$e^{2\Phi} = \left(1 - \frac{2Gm}{r}\right) \tag{1.3}$$

The Tolman-Oppenheimer-Volkoff (TOV) equations are

$$\begin{aligned} \frac{dP}{dr} &= -\frac{G\epsilon m}{r^2}\left(1 + \frac{P}{\epsilon}\right)\left(1 + \frac{4\pi P r^3}{m}\right)\left(1 - \frac{2Gm}{r}\right)^{-1} \\ \frac{dm}{dr} &= 4\pi r^2 \epsilon \end{aligned} \tag{1.4}$$

Where $\epsilon(r)$, $P(r)$ and $m(r)$ are the energy density, pressure, and enclosed gravitational mass at radius r respectively (see Refs. [117] and ([109] chapter 10)). These two equations can be solved given an EoS ($P(\epsilon)$), defining the relation between pressure and energy density for the fluid.

The boundary conditions for this set of equations are that the pressure is zero at the stellar surface ($r = R$) and the central density ρ_{cen} must be finite. Different EoS can have unique and profound impacts on the solutions of these TOV equations, where each mass-radius relationship is unique for a given EoS and a unique central density. Hence, mass-radius observations can greatly constrain the EoS. Assuming there is only one true EoS, all the observations of NS mass-radius should fall on a single mass-radius curve from different central densities.

1.4 Equation of State (EoS)

The equation of state (EoS) of neutron stars has evolved significantly since the initial theoretical studies in the early 20th century. After the early proposal of the existence of neutron stars as a result of supernovae explosions [8], in the mid-20th century, polytropic models became popular for their simplicity and analytical tractability. These models express the pressure as a power-law function of the density. The most commonly used polytropic

EoS is the one-parameter family given by:

$$P = K\rho^{\gamma} \tag{1.5}$$

where P is pressure, ρ is density, K is a constant, and γ is the polytropic index. The work by Chandrasekhar (1931) on degenerate stars introduced such models for white dwarfs, which influenced later studies of neutron stars [20]. The concept of neutron stars as dense, degenerate objects is further developed [136] in the 1950s. By the 1960s, more sophisticated models of EoS began to emerge that included nuclear interactions. The introduction of the Skyrme interaction [116] allowed for a better description of the nuclear matter, leading to an improved understanding of neutron-rich systems.

In the 1980s the development of nuclear physics and many-body theory enabled more accurate calculations of neutron star EoS [10, 113]. While from 2000s-present, advances in observational astronomy and computational power have led to more precise measurements of neutron star masses and radii, constraining EoS models [64, 87].

The idea of unusual states of matter within neutron stars was further investigated once more massive neutron stars, such as PSR J0740+6620 ($2.072^{+0.067}_{-0.066}\ M_{\odot}$) [104], were discovered. Research shifted to models that included quark matter, pion condensation, and hyperons [64]. The impact of extra degrees of freedom in the dense interior of neutron stars is intended to be addressed by these models.

Ongoing research focuses on inverting stellar structure equations to determine EoS from observed neutron star properties [121], investigating non-perturbative treatments of quark matter in neutron stars [72], and exploring the implications of recent well-measured neutron star masses for EoS models [67]. Probing dense nuclear matter for its EoS is a challenging task and can be categorized into two different approaches: ab initio models and phenomenological models. Ab initio models employ quantum many-body interactions with few assumptions and can be typically systematically improved by including higher-order corrections. However, these models are often too computationally expensive for larger nuclei. Phenomenological models use more simplifying assumptions and enable faster calculations. Some of these phenomenological models depend on effective interactions and using them we can approximately reproduce nuclear matter properties. A summary of these models can be found in Ref. [34].

In our case, we use relativistic mean field (RMF) models, a phenomenological model of nuclei and nuclear matter. As mentioned in Ref. [34], RMF models have been quite successful, describing both nuclei and exotic nuclei (see, the references in Ref. [34] for a brief overview of different RMF parameterizations and their comparisons).

1.4.1 Relativistic Mean-Field EoS

The 1980s saw the development of relativistic mean field models, which incorporated relativistic effects and meson exchanges. Originally developed by Serot and Walecka, these models provide a self-consistent treatment of nucleons and mesons, leading to a more accurate representation of the EoS in dense matter [113].

Based on quantum hadrodynamics, the system consists of Dirac nucleons coupled with isoscalar (σ and ω) and isovector mesons (ρ) [113]. Here, the exchange of mesons describes the interaction between baryons. The full Lagrangian thus is a sum of individual Lagrangians of the Dirac nucleons (Ψ, nucleon field) and the meson fields (σ, ω, and ρ) with an interaction term.

$$\mathcal{L} = \mathcal{L}_{\text{Dirac}} + \mathcal{L}_{\sigma} + \mathcal{L}_{\omega} + \mathcal{L}_{\rho} + \mathcal{L}_{\text{int}} \tag{1.6}$$

Where the individual parts can be written as:

$$\begin{aligned}
\mathcal{L}_{\text{Dirac}} &= \bar{\Psi}_i \left[i\partial\!\!\!/ - g_\omega \omega\!\!\!/ - \frac{g_\rho}{2} \vec{\rho}\!\!\!/ \cdot \vec{\tau} - M_i + g_\sigma \sigma - e_i A\!\!\!/ \right] \Psi_i \\
\mathcal{L}_{\sigma} &= \frac{1}{2}(\partial_\mu \sigma)^2 - \frac{1}{2} m_\sigma^2 \sigma^2 - \frac{bM}{3}(g_\sigma \sigma)^3 - \frac{c}{4}(g_\sigma \sigma)^4 \\
\mathcal{L}_{\omega} &= -\frac{1}{4} f_{\mu\nu} f^{\mu\nu} + \frac{1}{2} m_\omega^2 \omega^\mu \omega_\mu + \frac{\zeta}{24} g_\omega^4 (\omega^\mu \omega_\mu)^2 \\
\mathcal{L}_{\rho} &= -\frac{1}{4} \vec{B}_{\mu\nu} . \vec{B}^{\mu\nu} + \frac{1}{2} m_\rho^2 \vec{\rho}^\mu . \vec{\rho}_\mu + \frac{\zeta}{24} g_\rho^4 (\vec{\rho}^\mu) . \vec{\rho}_\mu \\
\mathcal{L}_{\text{int}} &= g_\rho^2 f(\sigma, \omega) \vec{\rho}^\mu . \vec{\rho}_\mu
\end{aligned} \tag{1.7}$$

The nucleon masses are represented by M_i and q_i represents the charge. The meson masses are m_i, and meson-nucleon couplings are g_i ($i = \sigma, \omega, \rho$). The couplings c_i are related to g_i by

$$c_i = g_i / m_i \tag{1.8}$$

$M = 939$ MeV and b and c are couplings without units. They are related to κ and λ by:

$$\kappa = 2Mb \qquad \lambda = 6c \tag{1.9}$$

The function f is the coefficient of $g_r^2 \rho^2$

$$\begin{aligned}
f(\sigma, \omega) &= b_1 \omega^2 + b_2 \omega^4 + b_3 \omega^6 + a_1 \sigma + a_2 \sigma^2 \\
&+ a_3 \sigma^3 + a_4 \sigma^4 + a_5 \sigma^5 + a_6 \sigma^6
\end{aligned} \tag{1.10}$$

where the notation from Ref. [57] is:

$$f(\sigma,\omega) = \lambda_4 g_s^2 \sigma^2 + \lambda_\nu g_\omega^2 \omega^2 \tag{1.11}$$

This implies $b_1 = \lambda_\nu g_\omega^2$ and $a_2 = \lambda_4 g_s^2$. Additional couplings are from Ref. [123].

At equilibrium the field equations are:

$$\begin{aligned} -m_\sigma^2 \sigma &= -g_\sigma n_s(r) + bMg_\sigma^3\sigma^2 + cg_\sigma^4\sigma^3 - g_\rho^2\rho^2\frac{df}{d\sigma} \\ -m_\omega^2 \omega &= -g_\omega n(r) + \frac{\zeta}{6}g_\omega^4\omega^3 + g_\rho^2\rho^2\frac{df}{d\omega} \\ -m_\rho^2 \rho &= -\frac{g_\rho}{2}[n_n(r) - n_p(r)] + 2g_\rho^2\rho f + \frac{\epsilon}{6}g_\rho^4\rho^3 \end{aligned} \tag{1.12}$$

Given the equations of motion above for the mesons and the Lagrangian, we can derive important nuclear properties that are measurable in a lab for finite nuclei to test against theory.

Nuclear Properties

The saturation density is the critical density where the central density remains the same even if the system acquires more nucleons. This happens due to the close-range repulsive interactions between the nucleons. The saturation density $\rho_0 \sim 2.8 \times 10^{14}$ gm/cm^{-3} or 0.153 fm^{-3} in Ref. [41] and 0.16 fm^{-3} in Refs. [135, 29].

At saturation density, the system is at its ground state energy and the energy per baryon required to form the system is its binding energy, E/A. For symmetric nuclear matter, the binding energy per particle

$$\begin{aligned} \frac{E}{A} = \frac{1}{n_0}\Bigg[U(\sigma_0) + \frac{1}{2}m_\omega\omega_0^2 + \frac{\zeta}{8}(g_\omega\omega_0)^4 \\ + \frac{2}{\pi^2}\int_0^{k_f} dk k^2\sqrt{k^2 + M^{*2}}\Bigg] \end{aligned} \tag{1.13}$$

$$U(\sigma) = \frac{1}{2}m_\sigma^2\sigma^2 + \frac{bM}{3}(g_\sigma\sigma)^3 + \frac{c}{4}(g_\sigma\sigma)^4 \tag{1.14}$$

Where the Dirac effective mass is $M_i^* = M_i - g_\sigma\sigma_0$, $U(\sigma)$ is the scalar meson potential and k_f is the Fermi momentum [123, 117]. The binding energy value is given as -16.3 MeV/nucleon in Ref. [41] and -16.0 MeV/nucleon in Refs. [135, 29]

The nuclear incompressibility K at saturation density dictates how the energy density varies with changes in pressure [123, 117].

$$\begin{aligned} K &= 9\frac{g_\omega^2}{m_\omega^2}n_0 + 3\frac{k_F^2}{E_F^*} - 9n_0\frac{M^{*2}}{E_F^{*2}} \\ &\times \left[\left(\frac{1}{g_\sigma^2}\frac{\partial^2}{\partial\sigma_0^2} + \frac{3}{g_\sigma M^*}\frac{\partial}{\partial\sigma_0}\right)U(\sigma_0) - 3\frac{n_0}{E_F^*}\right]^{-1} \end{aligned} \tag{1.15}$$

The nuclear compressibility K is around 234 MeV according to Ref. [41], while Ref. [135] predicts K at 265 MeV [29].

Stable lower mass nuclei often prefer nearly equal neutron and proton numbers (symmetric nuclear matter) while heavy nuclei neutron numbers exceed the proton numbers due to Coulomb repulsion, resulting in neutron-rich nuclei. This asymmetry results in a variation of the binding energy and is represented by the symmetry energy [123, 117].

$$E_{sym} = \frac{k_F^2}{6E_F^*} + \frac{n}{8(g_\rho^2/m_\rho^2 + 2f(\sigma_0,\omega_0))} \tag{1.16}$$

Where σ_0, ω_0 are the mean field values of σ and ω respectively. The function f dictates how the symmetry energy varies as a function of density.

The slope L of the symmetry energy is defined as [117]:

$$L(n_B,\delta) \equiv 3n_B\frac{\partial E_{sym}(n_B,\delta)}{\partial n_B} \tag{1.17}$$

Where n_B is the total baryon number density, $\delta \equiv (n_n - n_p)/n_B$ is the asymmetry and $\epsilon \equiv (n_B - n_0)/3n_0$ with n_0 as the nuclear saturation density. The symmetry energy coefficient (arising from the isospin asymmetry) S is $31-33$ MeV according to Ref. [66] and 32.5 MeV according to Ref. [41, 135, 29].

Charge radius is a fundamental nuclear property that connects effective interactions with the structure of nuclei and is dependent on the root-mean-square (rms) radius of the proton. The rms radius is defined to be [56]:

$$R_{\text{rms}}^2 = 4\pi\int r^4\rho(r)dr \tag{1.18}$$

where $\rho(r)$ is the density of protons. When this density is replaced by the charge density, we get the charge radius. The charge density according to [56]:

$$\rho_{\text{ch}}(r) = \int dr'\rho_{\text{cd}}(r-r')\rho_P(r') \tag{1.19}$$

where $\rho_{\rm cd}(r)$ is the charge distribution of protons and $\rho_P(r)$ is point proton density.

Skin thickness of the nuclei is the difference between the rms radius of neutrons and protons [126]:

$$R_{\rm skin} = R_{{\rm rms},n} - R_{{\rm rms},p} \tag{1.20}$$

While RMF EoS is able to accurately predict nuclei properties up to twice the saturation density that can be checked by nuclear experiments, a neutron star can be much denser than is probed in laboratory experiments and only observations of neutron stars can help put constraints on the EoS in these regions. The thermal evolution of a neutron star depends greatly on the composition and the EoS. Simulating cooling using existing theory and comparing it with the observed age and luminosities of a neutron star can provide fundamental information on interior physics.

1.5 Neutron Star Cooling

Even before the discovery of the first NS, early theories of thermal emission from a cooling NS predicted the possibility of detecting their existence in the early 1960s [21]. Tsuruta and Cameron pioneered the cooling theory in 1966 [130] that laid the groundwork and would be the standard for years to come. NS are born from supernova explosions of massive stars, and they cool by neutrino and photon emissions [144]. After an initial thermal relaxation era after being born, the neutron star is isothermal throughout [114] and the cooling is dominated early by neutrino emission and later by photon emission. By solving the thermal evolution of a NS one can get the surface temperature and the luminosity of a NS as a function of time ($T_s^\infty(t)$ and $L_\gamma^\infty(t)$) henceforth termed as cooling curves. Given we have observations of stars with known age and luminosity/surface temperatures, the ideal EoS would be able to predict these observations with reasonable accuracy. Thorne provided the complete set of equations to solve the evolution of a NS in hydrostatic equilibrium in 1977 [127] that included general relativity (GR). Considering a spherically symmetric star, for a given EoS, one can solve the general relativistic equations of thermal evolution which are the energy balance and heat transport equations [90]:

$$\frac{e^{-\lambda-2\Phi}}{4\pi r^2}\frac{\partial}{\partial r}(e^{2\Phi}L_r) = -Q_\nu + Q_h - \frac{C_v}{e^\Phi}\frac{\partial T}{\partial t} \tag{1.21}$$

and

$$\frac{L_r}{4\pi\kappa r^2} = e^{-\lambda-\phi}\frac{\partial}{\partial r}(Te^\Phi) \tag{1.22}$$

Where L_r is the luminosity at radius r. The emissivities Q_ν and Q_h are from neutrino and reheating respectively. Heat capacity is C_v and κ is the thermal conductivity. The functions $\phi(r)$ and $\lambda(r)$ are the metric functions described in Ref. [144].

This propelled the development and refinement of cooling theory in the following years which included writing sophisticated codes with GR [39] and comparisons of different models [82, 83, 84]. In the following years, "standard cooling" was employed to try and explain the discovered cooling NSs. This model presumes that NS cooling happens primarily through modified Urca process from the neutrinos in the stellar core. Along with it, there is also some nucleon-nucleon bremsstrahlung involved. When the proton fraction in the stellar core is not large enough to allow for direct Urca, the momentum conservation condition is not met. However, by adding a spectator neutrino, a different reaction takes place that emits neutrinos and anti-neutrinos as a result. This is the modified Urca process [88].

$$\begin{aligned} n + n' &\to p + n' + e^- + \bar{\nu}_e \\ p + n' + e^- &\to n + n' + \nu_e \end{aligned} \tag{1.23}$$

However, this has much lower emissivity compared to direct Urca ($\sim 10^{-6}\epsilon_{\rm DU}$). Muons can appear in these reactions when the chemical potential is comparable to their mass and this produces similar reactions with electrons being replaced by the Muons. For detailed descriptions and emissivity rates take a look at Ref. [90].

Later on, it was suggested that "enhanced cooling" is possible inside a NS core if there are exotic particles present. This idea was kept in check after Lattimer discovered in 1991 that the Direct Urca process can occur even for standard nuclear matter for some EoS [63]. The direct Urca process (DU) is one of the fast neutrino emission processes that is β and inverse β decays when only nuclear matter is involved [88].

$$n \to p + e^- + \bar{\nu}_e \quad \text{and} \quad p + e^- \to n + \nu_e \tag{1.24}$$

Energy and momentum need to be conserved by these equations. Momentum conservation gives us the famous triangle rule:

$$p_{F,n} < p_{F,p} + p_{F,e} \tag{1.25}$$

Now the number density can be written as $n_i = \frac{k_{F,i}^3}{3\pi^2}$. This implies:

$$n_n^{1/3} \leq n_p^{1/3} + n_e^{1/3} = 2n_p^{1/3} \tag{1.26}$$

which provides the minimum proton fraction required for direct Urca to happen:

$$x_{p,\min} \equiv \frac{n_p}{n_n + n_e} \geq \frac{1}{9} \approx 11\% \tag{1.27}$$

Cooper (1956) and others [24] developed theoretical predictions of neutron superfluidity, laying the groundwork for understanding pairing mechanisms in fermionic systems (BCS theory). These theories were extended to the context of neutron stars, proposing that below a certain critical temperature $T_{\rm c}(\rho)$, neutrons in the stellar core could form Cooper pairs, leading to a superfluid state [75]. There is a gap $2\Delta(T)$ near the Fermi energy for the single particle excitations for the nucleons and the nucleons form Cooper pairs to populate the higher energy state and emit a neutrino antineutrino pair in the process.

$$\begin{aligned} p + p &\rightarrow [pp] + \nu + \bar{\nu} \\ n + n &\rightarrow [nn] + \nu + \bar{\nu} \end{aligned} \tag{1.28}$$

This pairing can occur in the ${}^1S_0$ channel for both neutrons and protons at lower energies and can happen in the ${}^3P_2$ channel for neutrons at higher energies. The gap function at zero temperature is related to the critical temperature by [92]:

$$\Delta(T = 0) \sim 1.75 k_{\rm B} T_{\rm c} \tag{1.29}$$

Pairing can have large effects on neutron star cooling. The specific heat and the neutrino emissivity from the predominant neutrino emission processes are suppressed exponentially as a function of the gap size, while the governing neutrino emissions come from the pair-breaking process which is also a lot weaker compared to the direct Urca emissivity ($\sim 10^{-6}\epsilon_{\rm DU}$). This PBF emissivity is at its strongest just below $T_{\rm c}$, and it gets weaker as the star cools down. Fig. 1.2 shows different superfluid gap models as a function of the Fermi momentum.

Page proposed the "minimal cooling" model [91] in 2009 that considered adding the neutrino emission processes arising due to superfluidity (pair-breaking formation) along with "standard cooling" and assumed all forms of direct Urca processes were prohibited. This was successful and was consistent with the observations that were available at the time. However, recent observations of cold neutron stars [53] challenge this model, and "enhanced cooling" must be explored in greater depth.

The presence of exotic matter and opening up the corresponding neutrino emission processes also affects the thermal evolution [88] and can be incorporated into these cooling models depending upon which processes are available. The various types of neutrino emission processes that can occur in a neutron star can be summarized in Table. 1.1. These processes

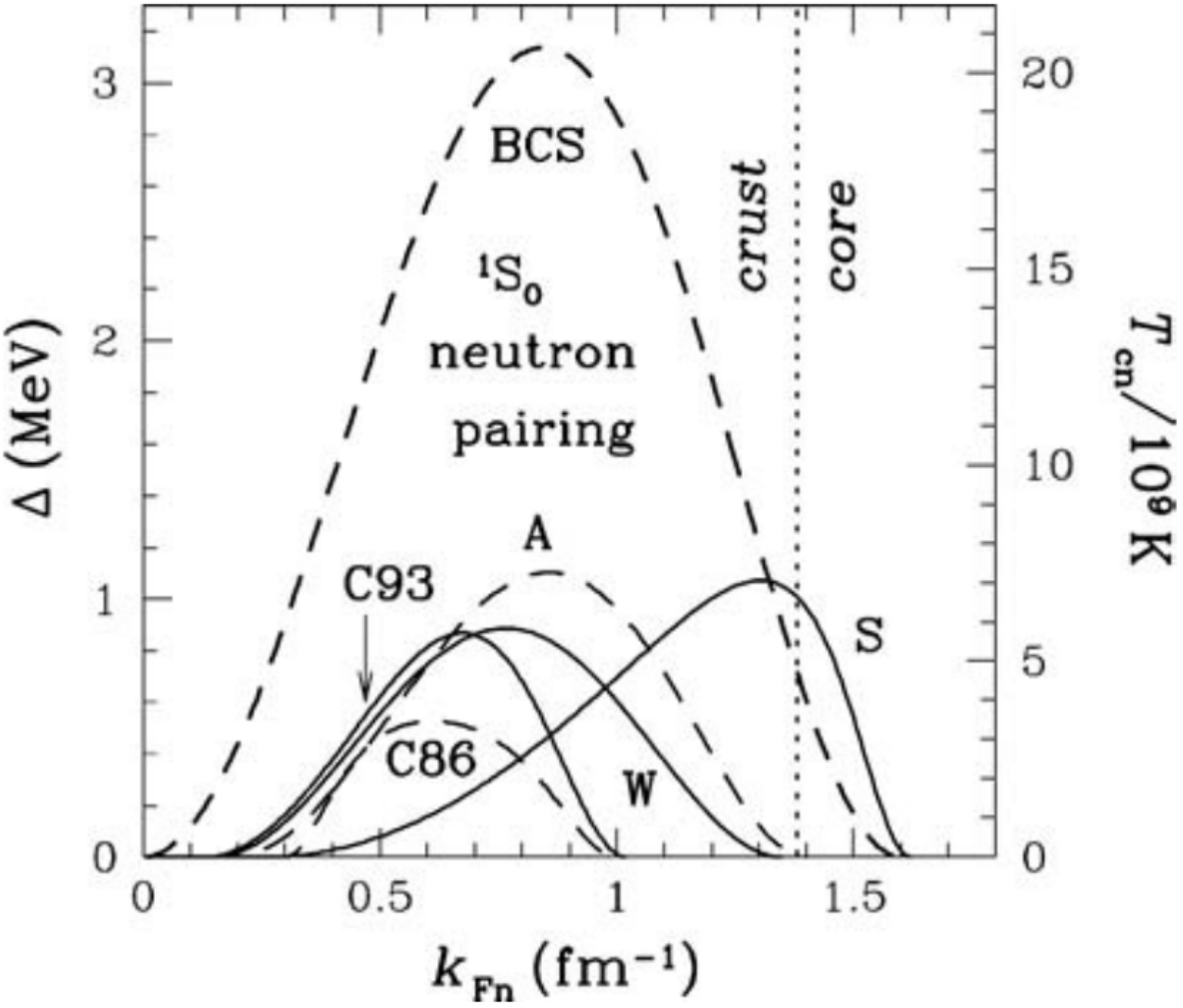


Figure 1.2: Different gap models (left axis) and the critical temperatures (right axis) as a function of the crust neutron Fermi momentum from Figure 9 in Ref. [144]. The crust-core transition is denoted as the vertical dotted line. The uncertainties in these models are by a factor of 2.

can be broadly categorized into two sections, slow emission processes and fast emission processes. Their emissivities can be written as [144]

$$Q_{\text{slow}} \propto T_9^8, \quad Q_{\text{fast}} \propto T_9^6, \tag{1.30}$$

Assuming $C_v = C_9 T_9$ (where $T_9 \equiv T/(10^9\ \text{K})$ and $C_9 \simeq 10^{39}\ \text{erg/K}^{-1}$ [92]), the neutrino and photon luminosities can be written as [88]:

$$L_\nu = N_9 T_9^8 \quad \text{and} \quad L_\gamma \equiv 4\pi R^2 \sigma_{SB} T_e^4 = S_9 T_9^{2+4\alpha} \tag{1.31}$$

Where $N_9 \simeq 10^{40}\ \text{erg/s}^{-1}$ and $S_9 \simeq 10^{33}\ \text{erg/s}^{-1}$ and α comes from the $T_e - T_b$ relationship [92]. The border between the envelope and outer crust is called the boundary and the effective temperature of the star T_e is related to this boundary temperature T_b like [44]:

$$T_e \simeq 10^6\ \text{K} \times \left(\frac{T_b}{10^8\ \text{K}}\right)^{0.5+\alpha} \tag{1.32}$$

With $\alpha \ll 1$. The energy balance equation becomes:

$$C_v \frac{dT}{dt} = -L_\gamma - L_\nu \tag{1.33}$$

Neutrino cooling era ($L_\nu \gg L_\gamma$): The neutron star is cooled by various neutrino emission processes, the strongest of them arising from its core.

$$\frac{dT_9}{dt} = -\frac{N_9}{C_9} T_9^7 \quad \rightarrow \quad t - t_0 \propto \left[\frac{1}{T_9^6} - \frac{1}{T_{0,9}^6}\right] \tag{1.34}$$

where at time t_0, the initial temperature is $T_{0,9}$. For $T_9 \ll T_{0,9}$

$$T_9 \propto t^{-\frac{1}{6}} \text{ and } T_e \propto t^{-\frac{1}{12}} \tag{1.35}$$

Photon cooling era ($L\nu \ll L_\gamma$): After the neutrino emission era, the star is cooled by photon emission from its surface, which in turn affects the internal temperature of the star [144].

$$\frac{dT_9}{dt} = -\frac{N_9}{S_9} T_9^{1+\alpha} \quad \rightarrow \quad t - t_0 \propto \left[\frac{1}{T_9^\alpha} - \frac{1}{T_{0,9}^\alpha}\right] \tag{1.36}$$

and this gives:

$$T_9 \propto t^{-1/\alpha} \quad \text{and} \quad T_e \propto t^{-1/2\alpha} \tag{1.37}$$

As the $T_e - T_b$ relationship is not dependent on the stars M or R explicitly, different envelope models have less drastic effects on the cooling of a neutron star [90]. However, since α signifies

Table 1.1: The different neutrino emission processes and their emissivities [89]. The coefficients R's are control functions to incorporate the effects of pairing. $T9 \equiv T/(10^9\ \mathrm{K})$, efficiency of how fast the process cools the star is on the right side.

Name	Process	Emissivity (erg cm^{-3} s^{-1})	
Modified Urca cycle (neutron branch)	$n+n \to n+p+e^-+\bar{\nu}_e$ $n+p+e^- \to n+n+\nu_e$	$\sim 2\times 10^{21} RT_9^8$	Slow
Modified Urca cycle (proton branch)	$p+n \to p+p+e^-+\bar{\nu}_e$ $p+p+e^- \to p+n+\nu_e$	$\sim 10^{21} RT_9^8$	Slow
Bremsstrahlung	$n+n \to n+n+\nu+\bar{\nu}$ $n+p \to n+p+\nu+\bar{\nu}$ $p+p \to n+p+\nu+\bar{\nu}$	$\sim 10^{19} RT_9^8$	Slow
Cooper pair formations	$n+n \to [nn]+\nu+\bar{\nu}$ $p+p \to [pp]+\nu+\bar{\nu}$	$\sim 5\times 10^{21} RT_9^7$ $\sim 5\times 10^{19} RT_9^7$	Medium
Direct Urca cycle (nucleons)	$n \to p+e^-+\bar{\nu}_e$ $p+e^- \to n+\nu_e$	$\sim 10^{27} RT_9^6$	Fast
Direct Urca cycle (Λ hyperons)	$\Lambda \to p+e^-+\bar{\nu}_e$ $p+e^- \to \Lambda+\nu_e$	$\sim 10^{27} RT_9^6$	Fast
Direct Urca cycle (Σ^- hyperons)	$\Sigma^- \to n+e^-+\bar{\nu}_e$ $n+e^- \to \Sigma^-+\nu_e$	$\sim 10^{27} RT_9^6$	Fast
π^- condensate	$n+<\pi^->\to n+e^-+\bar{\nu}_e$	$\sim 10^{26} RT_9^6$	Fast
K^- condensate	$n+<K^->\to n+e^-+\bar{\nu}_e$	$\sim 10^{25} RT_9^6$	Fast
Direct Urca cycle (u-d quarks)	$d \to u+e^-+\bar{\nu}_e$ $u+e^- \to d+\nu_e$	$\sim 10^{27} RT_9^6$	Fast
Direct Urca cycle (u-s quarks)	$s \to u+e^-+\bar{\nu}_e$ $u+e^- \to s+\nu_e$	$\sim 10^{27} RT_9^6$	Fast

the composition of the atmosphere and at later stages of photon cooling ($t \gg t_0$), due to its small value the exponent of eq. 1.29 gets larger, dictating how the star is cooled.

The cooling process is affected by various factors like the neutrino emission rate, the heat capacity of the stellar interior, etc.; which in turn depend greatly on the superfluidity inside the star and the choice of EoS. The envelope also plays a crucial role in thermal conduction and possible reheating due to accretion.

1.5.1 Specific Heat

Understanding a neutron star's thermal properties and evolutionary processes requires knowledge of its specific heat. The core, where density and pressure are extremely high and the matter is mostly formed of neutrons with an admixture of protons, electrons, and perhaps exotic particles, contributes the most to heat capacity. The specific heat of the star can vary significantly depending on the degrees of freedom present [72]. The total specific heat per volume for a neutron star core consisting of only neutrons, protons, and electrons can be expressed as [27]

$$c_v^{\text{core}} = c_{v,e} + c_{v,p} + c_{v,n} \tag{1.38}$$

Where,

$$c_{v,i} = \frac{K_B^2}{3\hbar^3} T \sqrt{K_{F,i}^2 + m_i^2} K_{F,i} \tag{1.39}$$

The contribution to specific heat from the outer crust has less impact than that of the core. In the outer crust, the specific heat is influenced by the presence of heavy nuclei and the dynamics of the surrounding electron gas [27].

$$c_v^{\text{crust}} = c_{v,e} + c_{v,n} + c_{v,\text{ion}} \tag{1.40}$$

With

$$c_{v,\text{ion}} = \frac{2\pi^2}{15} \left(\frac{T^3}{v_l^3} + \frac{2T^3}{v_t^3} \right) \tag{1.41}$$

Where v_l and v_t are the longitudinal and transverse velocities of the lattice photons. The interplay between these components can result in a complex thermal behavior [41]. Ref. [42] provides a comprehensive outline of how the crust's heat capacity contributes to the overall thermal properties of the star, especially at lower densities. As the temperature of a neutron star decreases, so does its specific heat, resulting in slower thermal evolution compared to less dense stellar remains [65].

The transition to a superfluid state at low temperatures introduces additional complexities in the specific heat calculation. Superfluid neutrons have a particular temperature dependency, which influences the star's thermal properties. Below a certain temperature,

the specific heat drops dramatically, indicating a phase change to a superfluid state [90]. This phenomenon is important for understanding cooling processes in neutron stars because superfluidity can reduce heat capacity and alter cooling rates.

1.5.2 Accretion Effects

The transient accreting stars generally have quiescence phases that last much shorter than the thermal relaxation timescale of neutron stars, which is approximately 10,000 years. Because of this, it's often reasonable to ignore thermal changes in the core and assume that their internal temperature remains stable and unaffected by transient accretion. Thermal evolution of transient NS in their quiescent phase (see Refs. [53, 141, 144, 142]) are discussed in details in Ref. [47] where the deep crustal heating [45, 46] due to accretion is radiated away by neutrino and photon emissions in its steady-state. The energy balance equation reads.

$$L_h^\infty(\dot{M}) = L_\nu^\infty + L_\gamma^\infty, \tag{1.42}$$

The red shifted deep-crustal heating $L_{\rm dh}$ [141] depends on the average accretion rate $\dot{M}$ according to

$$\begin{aligned} L_{\rm dh} &= Q \times \frac{\dot{M}}{m_{\rm N}} \\ &\approx 6.03 \times 10^{33} \left(\frac{\dot{M}}{10^{-10}\,{\rm M}_\odot\,{\rm yr}^{-1}} \right) \frac{Q}{\rm MeV} {\rm ergs}^{-1} \end{aligned} \tag{1.43}$$

$$L_{\rm dh}^\infty = L_{\rm dh}\sqrt{1-2GM/(c^2R)} \tag{1.44}$$

where Q is the heat released per accreted nucleon [47]. The red shifted photon and neutrino luminosities can be expressed as [47]

$$L_\gamma^\infty = 4\pi\sigma T_s^4 R^2(1-2GM/(c^2R)) \tag{1.45}$$

$$L_\nu^\infty = 4\pi \int_0^R \frac{{\rm d}r r^2 \epsilon_\nu e^{2\phi(r)}}{\sqrt{1-2Gm(r)/(c^2r)}} \tag{1.46}$$

solving the energy balance equation gives us the heating curves that is luminosity and temperature as a function of average accretion rates ($L_\gamma^\infty(\dot{M})$ or $T_s^\infty(\dot{M})$).

1.6 Motivation

Ref. [90] analyzed isolated neutron star cooling observations by constructing a "minimal model". This minimal model had as few parameters as possible, presumed a fixed EoS, and assumed that fast cooling processes were ruled out. However, these slower cooling processes were later discovered to be insufficient to explain the colder accreting neutron stars observed like SAX J1808 [53]. These colder accreting neutron stars appear to require fast neutrino emission processes like the direct Urca processes (see table. 1.1). The direct Urca processes cool the neutron star rapidly because the associated emissivity is 5-6 orders of magnitude higher than the minimal cooling model's thermal emissivity [70].

While fast neutrino cooling processes appear to be required to explain the observational data, nucleonic superfluidity has a dramatic effect on these neutrino emissivities. Migdal [75] first hinted at the existence of superfluidity inside neutron stars below a certain critical temperature T_c in 1959. Superfluidity has three main impacts. First, it suppresses the specific heat exponentially. Second, it exponentially suppresses many cooling processes that would otherwise require breaking a Cooper pair. Finally, it creates a new cooling process: the Cooper pair formation neutrino emissivity (see e.g. a recent review of the impact of superfluidity on cooling in Ref. [92]).

Previous works Ref. [12] and Ref. [47] provide valuable constraints on the superfluidity and direct Urca process and the interplay between them [13]. This work aims to add new isolated neutron stars observations from Ref. [100], LIGO data from GW170817 [2], updated neutron star mass-radius measurements for M30, two NICER pulsars J0030 [104, 76] and J0740 [105, 77]; and the PREX result [103] to get better constraints on the EoS and the nucleonic superfluidity.

Chapter 2

Methodology

In this article, we present one of the first applications of Bayesian inference with a detailed theoretical model for dense matter applied to a stellar evolution code that is specialized for the description of neutron star cooling. The inference is done with a Markov chain Monte Carlo (MCMC) simulation over a 151-dimensional parameter space, which solves the stellar evolution problem for different neutron star masses and different neutron star envelope compositions at every point. We render this large inference tractable with a machine learning-based proposal distribution.

2.1 The EoS and Superfluidity Parameters

For the EOS, we use the covariant theoretical model (also called relativistic mean-field theory, e.g. Ref. [113]) from Ref. [123] which differs from the typical formulation because it has additional parameters to model neutron-rich matter at high densities.

Starting from an IUFSU EoS, we parameterize the meson-nucleon couplings ($c_\rho, c_\sigma, c_\omega$), the σ meson mass (m_σ), the meson couplings from Ref. [78] (b, c, ζ, ξ) and we also have the additional higher-order meson couplings from Ref. [124] (b_1, b_2, b_3 and a_1, a_2, a_3, a_4, a_5, a_6). Initial values are set according to page 10 from Ref. [124].

As the calculations of the superfluid gap have uncertainties in them as different models like 'BCS', 'C86', 'C93' or 'A' provide different results, as can be seen in Fig. 1.2 (see Ref. [144] for more details), we assume that these gaps can be approximated by a Gaussian centered at the Fermi momentum:

$$T_c(k_F) = T_{c,\mathrm{peak}} \exp\left[\frac{(k_\mathrm{F} - k_{\mathrm{F,peak}})^2}{2\Delta k_\mathrm{F}^2}\right] \tag{2.1}$$

While we parameterize the height (critical temperature) $T_{c,\mathrm{peak}}$, the mean (peak-Fermi momentum) $k_{\mathrm{F,peak}}$ and the width Δk_F of the Gaussian for both neutrons and protons

separately (giving us total six parameters for our superfluidity). We apply the appropriate constraints explained in Ref. [11] and allow the enhanced cooling processes discussed in Refs. [90, 91].

2.2 Constructing The Likelihood Function

Our likelihood function is constructed from a data set that includes laboratory experiments on doubly-magic nuclei and neutron star observations. We include the binding energies and charge radii of doubly-magic nuclei (following Ref. [123]) and the parity-violated radius (PREX) experiment [4]. We include observations of gravitational waves from GW 170817A [2], photons from quiescent low-mass X-ray binary stars [119] (QLMXBs), photons from X-ray pulsars as observed by NICER [104, 76, 105, 77], photons from isolated neutron stars [100] (INSs), and photons from soft X-ray transiently accreting neutron stars (SXRTs; following Ref. [47]).

2.2.1 Nuclear Structure

The likelihood function for nuclear structure data is the product of two-dimensional Gaussians for the binding energy and charge radius of ^{208}Pb and ^{90}Zr (see Ref. [12]).

The recent measurement of the parity-violating asymmetry $A_{\rm PV}$ in ^{208}Pb by the PREX-2 collaboration (see [4]) provides a constraint to the skin-thickness (estimated 0.283 ± 0.071 fm). For our case, this adds another Gaussian for the skin-thickness to our likelihood and the total likelihood contribution from the nuclei looks like this:

$$\begin{aligned}
\mathcal{L}_{\rm nuclei} &= \exp\left[-\frac{\left(E_{\rm Zr}-\tilde{E}_{\rm Zr}\right)^2}{\left(0.02\tilde{E}_{\rm Zr}\right)^2}-\frac{\left(R_{\rm Zr}-\tilde{R}_{\rm Zr}\right)^2}{\left(0.02\tilde{R}_{\rm Zr}\right)^2}\right] \\
&\times \exp\left[-\frac{\left(E_{\rm Pb}-\tilde{E}_{\rm Pb}\right)^2}{\left(0.02\tilde{E}_{\rm Pb}\right)^2}-\frac{\left(R_{\rm Pb}-\tilde{R}_{\rm Pb}\right)^2}{\left(0.02\tilde{R}_{\rm Pb}\right)^2}\right] \\
&\times \exp-\frac{\left(R_{\rm skin}-\tilde{R}_{\rm skin}\right)^2}{\left(0.02\tilde{R}_{\rm skin}\right)^2}
\end{aligned} \tag{2.2}$$

Where E_i and $\tilde{E}_i$ are the calculated and the observed binding energies and R_i and $\tilde{R}_i$ are the calculated and observed charge radius respectively for ^{208}Pb and ^{90}Zr. $R_{\rm skin}$ and $\tilde{R}_{\rm skin}$ are the calculated and experimental skin-depth of ^{208}Pb.

Saturation Properties

Nuclear properties at saturation density are a product of the underlying EoS. We make sure these properties are physical and within observed constraints [41]. We restrict the saturation density n_0 between 0.14 fm^{-3} – 0.17 fm^{-3} and the binding energy E/A between -17 to -15 MeV. The compressibility K is constrained to lie between 220-260 MeV [37]. At the nuclear saturation density, we restrict the symmetry energy $S < 36$ MeV and the slope of the symmetry energy $L < 80$ MeV [68]. Any EoS that predicts any of these physical properties outside the bounds is rejected as a potential candidate for describing dense matter.

2.2.2 Multi-Messenger Astronomy

We have several different types of neutron stars in our population. Relatively new-middle-aged isolated neutron stars (INS) that do not have any accretion reheating, cool via neutrino and photon emissions. Old transient neutron stars that are thermally accreting (SXRT), quiescent low mass stars that are part of an X-ray binary (QLMXB) with partially known mass-radius data from observations of globular clusters. We also have 2 NICER stars and LIGO stars from GW170817.

The masses of these stars (apart from the stars in GW170817) are parameterized by m_f, the mass fraction, defined by, $m_f \equiv (M-1)/(M_{\rm max}-1)$, where M is the stellar mass and $M_{\rm max}$ is the maximum mass of a star allowed from solving the TOV-equations using our particular EoS. Naturally, m_f takes values between 0 and 1 as we consider 1 $M_\odot$ to be the lowest mass possible for a neutron star.

For our stars depending on their age, they can either have a light element envelope (H, He) or a heavy element envelope (C). INSs usually have their atmosphere from a natural sedimentation process after the supernova explosion while SXRTs and QLMXBs typically might accrete hot matter that accumulates onto their surface creating a light element layer on top of them. Stars with an envelope consisting of light elements cool faster than stars with an envelope of heavier elements due to better heat transport [90]. We parameterize the envelope as η, and it takes values from 10^{-7} to 10^{-17}, larger η represents the presence of more light elements in the envelope [11]. We choose fixed $\eta = 10^{-17}$ for stars older than 10^5 years or stars with spectra well fit by a black body spectrum as described in [100]. The cooling code computes eighteen different cooling curves, for six masses ($m = 1.0, 1.2, 1.4, 1.6, 1.8, 2.0\,{\rm M}_\odot$) and three η values ($\eta = 10^{-7}, 10^{-12}, 10^{-17}$). Results for other combinations of m and η are obtained through linear interpolation.

Isolated Neutron Stars

A neutron star not in a binary system have usually no accretion and cools down via neutrino and photon emissions mentioned above. X-ray-based observatories like Chandra can detect the pulses coming from these isolated neutron stars (INS) and sometimes the proper motion data of these stars are also available if they can be associated with a nearby supernova remnant. The pulse period P and its derivatives can be used to get a characteristic age or spin-down age of the star (defined by $t_c \equiv P/2\dot{P}$) and the proper motion is used to calculate the kinetic age t_k of the star.

We follow Ref. [100] and use the data set provided therein and eventually updated in Ref. [99]. This population consists primarily of weakly-magnetized thermal emitters and ordinary pulsars. We include four "high-B pulsars" which still have a magnetic field below 10^{14} G, four stars from the magnificent seven, two stars that have upper limits rather than two-sided constraints on their luminosities, and one middle-aged pulsar with hot spots. These are our isolated neutron stars (INS). Fig. 2.1 shows the luminosity L_γ^∞ plotted against ages t from Ref. [100] and some theoretical cooling curves for isolated neutron stars with different masses. Here the authors consider both non-accreted (solid curves) and accreted (dashed curves) envelopes.

Age (both t_k and t_c) and luminosity L data is in units of years and 10^{33} ergs/s respectively. These are converted to logarithmic scale with the new variables, $\hat{t}$ and $\hat{L}$ with their respective uncertainties $d\hat{t}$ and $d\hat{L}$ as often these uncertainties are presented in logarithmic scales.

$$\begin{aligned} \hat{t} &\equiv \frac{1}{5}\log_{10}\left(\frac{t}{10^2\ \text{yr}}\right) \\ \hat{L} &\equiv \frac{1}{4}\log_{10}\left(\frac{10^{33}\ L}{10^{30}\ \text{erg/s}}\right) \end{aligned} \tag{2.3}$$

This puts $\hat{t}$ in the range between 0 and 1. If the central value for the kinetic age is known, then it is used as $\hat{t}$ and the upper and lower limits of the kinetic age are used to determine $d\hat{t}$. If we do not know the age of the star accurately, but we have an upper and lower bound, then the mean of these bounds are taken as $\hat{t}$ and $d\hat{t}$ is calculated as before. If no information is available about the kinetic age and only the spin-down age is known, we treat the spin-down age as an upper limit, $d\hat{t}$ is set to zero and $\hat{t}$ is set as a parameter.

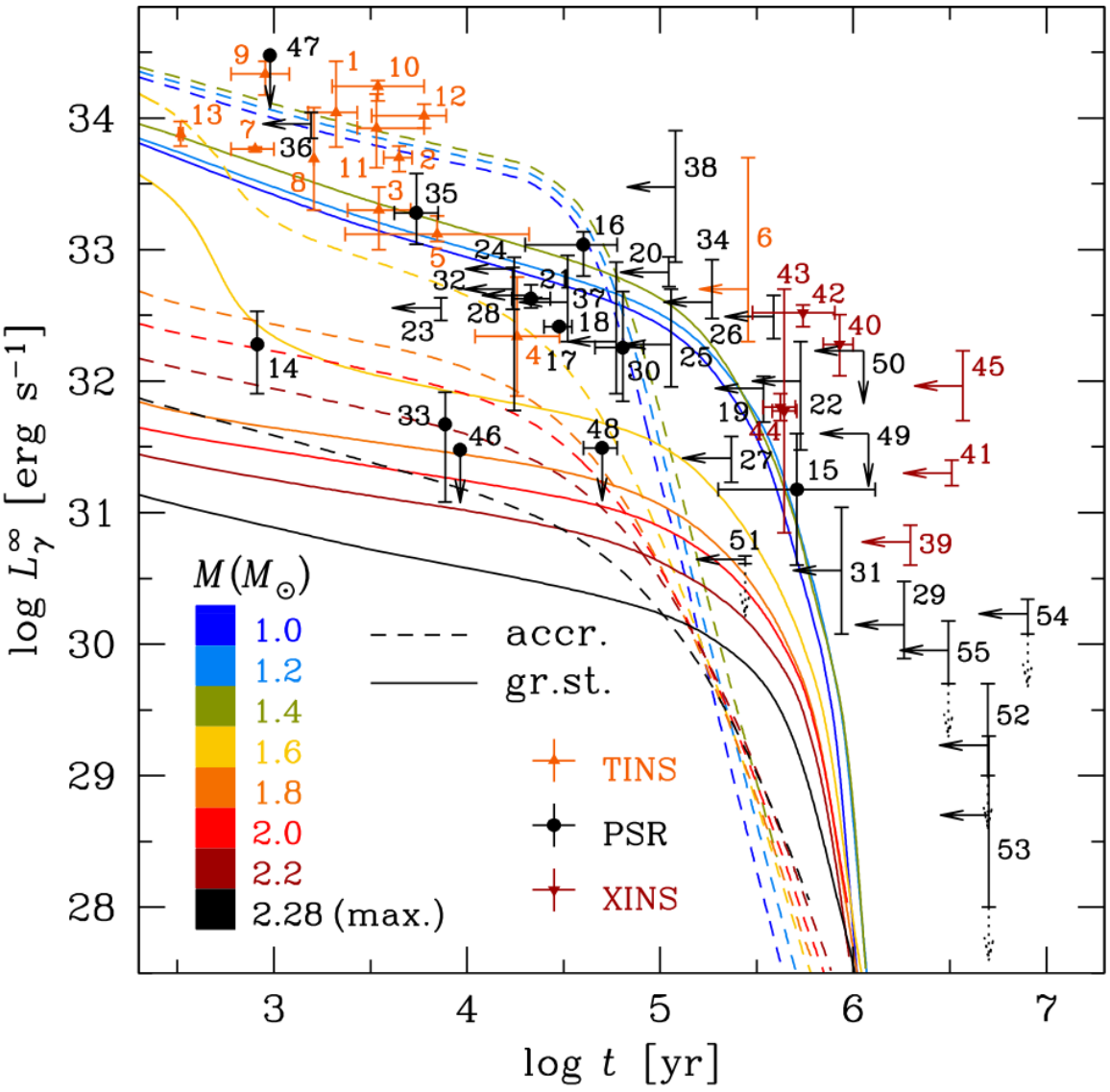


Figure 2.1: Theoretical cooling curves ($L_\gamma^\infty - t$) of isolated Neutron stars from Ref. [100] with observed age and luminosity data. Different mass values (denoted by different colors, noted at the bottom left of the figure) are used for multiple cooling curves. Non-accreted and accreted envelopes are in solid and dashed curves respectively. For superfluidity, the MSH+BS+TTav model is used with the BSk24 EoS. Arrows in the data points represent the upper limits of either luminosities or ages. With a fixed superfluidity and EoS, this model is not sufficient to explain stars on the top right quadrant of the figure.

The likelihood contribution from a star when both age and luminosity measurements are available is:

$$\mathcal{L}_{\mathrm{meas},j} \propto \sum_k \sqrt{\left\{\left[\frac{d\hat{L}(\eta_j)}{d\hat{t}}\right]^2 + 1\right\}} \exp\left\{\frac{-[\hat{t}_k - \hat{t}_j]^2}{2(\delta\hat{t}_j)^2}\right\} \times \exp\left\{\frac{-[\hat{L}_k(\eta_j) - \hat{L}_j]^2}{2(\delta\hat{L}_j)^2}\right\} \tag{2.4}$$

Where k runs over a uniform grid in $\hat{t} \in [0, 1]$ with grid size 100 (see [12] for details). $\hat{t}_j$ and $\hat{L}_j$ are the observed age and luminosity of the jth star. $\hat{t}_k$ and $\hat{L}_k$ are the calculated ages and luminosity at grid point k for that star.

If the age is an upper limit, the parameterized age is used to look up the luminosity from the cooling curve. In this case, there is no Gaussian contribution from age and

$$\exp\left\{\frac{-[\hat{t}_k - \hat{t}_j]^2}{2(\delta\hat{t}_j)^2}\right\} = 1, \tag{2.5}$$

the likelihood contribution from these stars is:

$$\mathcal{L}_{\mathrm{AUL},j} \propto \sum_k \sqrt{\left\{\left[\frac{d\hat{L}(\eta_j)}{d\hat{t}}\right]^2 + 1\right\}} \times \exp\left\{\frac{-[\hat{L}_k(\eta_j) - \hat{L}_j]^2}{2(\delta\hat{L}_j)^2}\right\} \tag{2.6}$$

Where AUL stands for age upper limit and k runs from 0 to the upper limit of that star.

A similar treatment is applied to the luminosity data as well. Only this time, we do not parameterize the luminosity in case of a luminosity upper-limit star and instead, just output the resulting luminosity for that particular star from our cooling calculations in our generated data files. These stars do not contribute to our likelihood functions directly for now and only act as a secondary constraint for the superfluidity and EoS in MCMC as we discard any point in the multidimensional parameter space that can not physically predict these stars' luminosities below the observed upper limits. So, for these luminosity upper limit (LUL) stars,

$$\begin{aligned} \mathcal{L}_{\mathrm{LUL},j} &= 0 \text{ when } \hat{L}_k > \hat{L}_j \text{ and} \\ \mathcal{L}_{\mathrm{LUL},j} &= 1 \text{ when } \hat{L}_k \leq \hat{L}_j \end{aligned} \tag{2.7}$$

So, suppose we have N number of INSs and among them, there are a number of stars with measured luminosities and ages, b number of stars with age upper limits, and c number of stars with luminosity upper limits such that:

$$N = a + b + c \tag{2.8}$$

The total likelihood contribution from N INSs look like

$$\mathcal{L}_{\rm INS} \propto \prod_{i=1}^{a} \mathcal{L}_{{\rm meas},i} \prod_{j=1}^{b} \mathcal{L}_{{\rm AUL},j} \prod_{k=1}^{c} \mathcal{L}_{{\rm LUL},k} \tag{2.9}$$

Thermally Emitting Accreting Neutron Stars

Soft X-ray transients (SXRTs) are a class of X-ray binary systems (typically a NS with a companion main sequence star) that usually remain in a quiescent, low-luminosity state but occasionally exhibit dramatic outbursts, during which the X-ray flux can increase by several orders of magnitude. During the quiescent phase, matter is accreted onto the accretion disk around the NS and eventually is absorbed by the NS releasing a burst of soft (low energy) X-ray emission. The thermal evolution of a SXRT in its quiescent phase closely resembles the cooling of an INS if the quiescent period is long enough except, this time deep crustal heating balances out the cooling from neutrino and photon emissions. After a prolonged period of accretion and quiescence, the star reaches a thermal equilibrium and by solving the energy balance equation (Eq. 1.42) we can find steady-state solutions that give a prediction of the heating curves ($L_\gamma^\infty(\dot{M})$). We use the cooling code to achieve thermal evolution of the SXRTs as the underlying physics is still the same [23, 141]. We presume half a decade of uncertainty in the time-averaged accretion rate for the SXRTs. Fig. 2.2 is a series of selected heating curves $\log_{10} L_\gamma^\infty - \log_{10}\dot{M}$ based on EoSs in [47] with superfluidity gap models "SFB-a-T73" and observational data taken from [53, 13].

The likelihood function for SXRT stars is constructed very similarly to our isolated neutron stars approach. For these stars, we have their luminosities L and accretion rates $\dot{M}$ as observed data in units of 10^{33} ergs/s and $M_\odot$/year respectively. The L and $\dot{M}$ are then converted to normalized log scale $\hat{L}$ and $\hat{\dot{M}}$.

$$\begin{aligned} \hat{L} &\equiv \frac{1}{4}\log_{10}\left(\frac{10^{33}\ L}{10^{30}\ erg/s}\right) \\ \hat{\dot{M}} &\equiv \log_{10}\dot{M} \end{aligned} \tag{2.10}$$

Stellar masses and the envelope environment are parameterized as mass fractions m_f and η for the MCMC. For very cold SXRTs SAX J1808.4-3658 [19, 52] and 1H 1905+000 [61], only

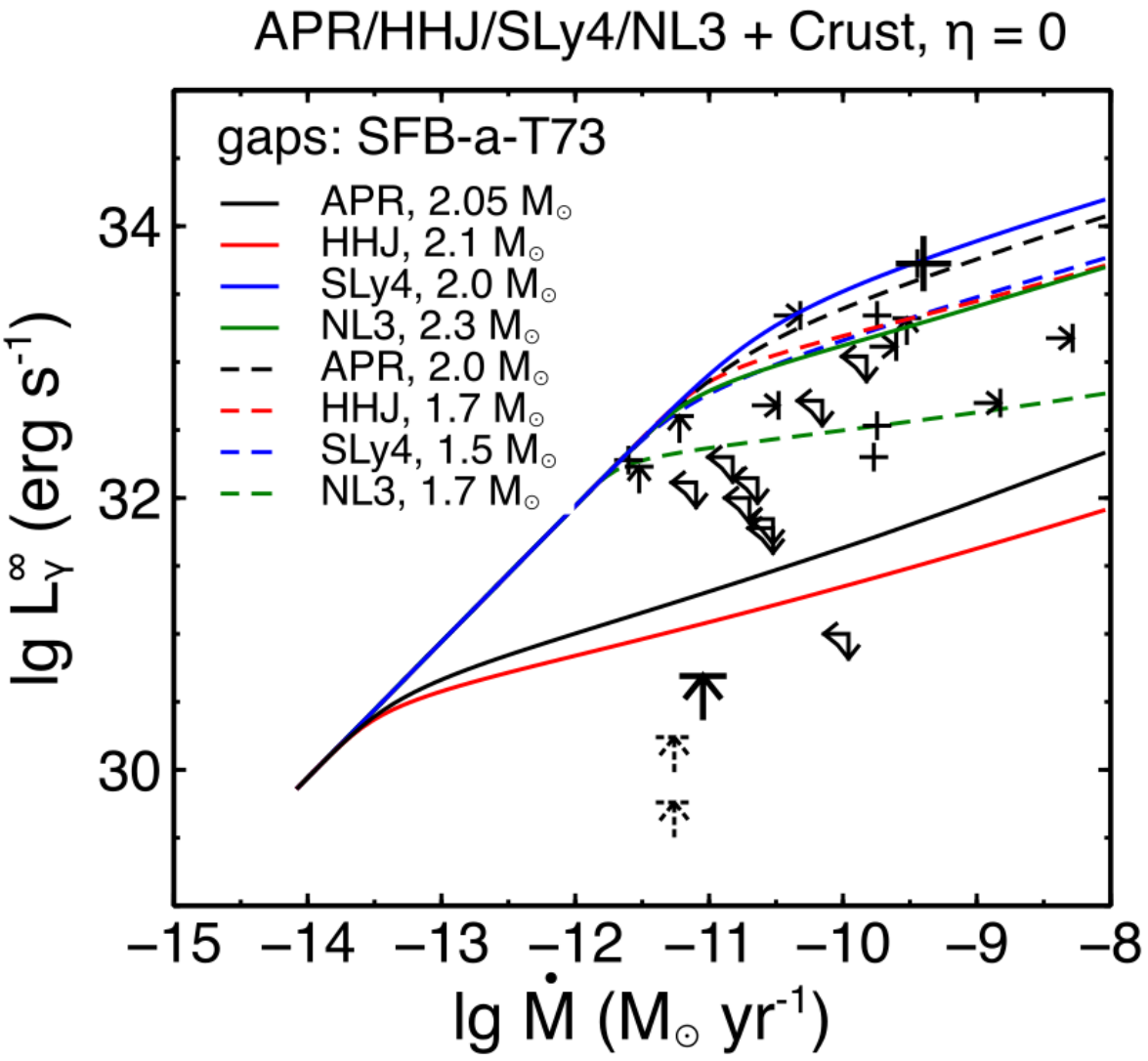


Figure 2.2: A series of steady-state curves ($L_\gamma^\infty - \dot{M}$) for SXRTs from Ref. [47] using APR, HHJ, SLy4, and NL3 EoS with SFB-a-73 model for the superfluid gap. Observed luminosities and accretion rates are from Refs. [53, 13]. The hottest SXRT Axl X-1 is denoted by the cross on the upper right quadrant and the coldest SXRT SAX J1808 is the enlarged solid arrow (dotted arrows underneath show old data). Without enhanced cooling, it is hard to explain the colder stars.

the upper limits of luminosities are known. In addition, for 1H 1905+000, $\dot{M}$ only provides an upper limit. These are also parameterized in the MCMC with appropriate uncertainties.

The cooling code calculates the steady-state curves for stars with masses ranging from 1-2 $M_\odot$, η ranging from $10^{-17} - 10^{-7}$ $M_\odot$ and $\dot{M}$ ranging from $10^{-14} - 10^{-8}$ $M_\odot$/yr. These results are stored in a 3-dimensional tensor grid which we use to interpolate and get luminosity for all different combinations of m, η, and $\dot{M}$.

Following Ref. [47] the likelihood contribution from each SXRT star for which luminosity and accretion rate are known measurements takes the form.

$$\begin{aligned}\mathcal{L}_{\mathrm{meas},j} \quad \propto \quad & \sum_k \sqrt{\left\{\left[\frac{d\hat{L}(\eta_j)}{d\hat{\dot{M}}}\right]^2 + 1\right\}} \\ & \times \exp\left\{\frac{-[\hat{\dot{M}}_k - \hat{\dot{M}}_j]^2}{0.5}\right\} \\ & \times \exp\left\{\frac{-[\hat{L}_k(\eta_j) - \hat{L}_j]^2}{0.5}\right\}\end{aligned} \tag{2.11}$$

where $\hat{L}_k$ and $\hat{\dot{M}}_k$ are the interpolated and $\hat{L}_j$ and $\hat{\dot{M}}_j$ are the observed luminosity and accretion rates respectively, and k runs over a uniform grid $[-12, 29]$ for $\log_{10}(\dot{M})$.

For SAX J1808 the luminosity is an upper limit and there is no Gaussian contribution from luminosity as long as the calculated luminosity is under the upper limit.

$$\begin{aligned}\exp\left\{\frac{-[\hat{L}_k(\eta_{1808}) - \hat{L}_{1808}]^2}{0.5}\right\} = 1 \quad \text{if} \quad \hat{L}_k \leq \hat{L}_{1808} \\ \exp\left\{\frac{-[\hat{L}_k(\eta_{1808}) - \hat{L}_{1808}]^2}{0.5}\right\} = 0 \quad \text{if} \quad \hat{L}_k > \hat{L}_{1808}\end{aligned} \tag{2.12}$$

and

$$\begin{aligned}\mathcal{L}_{1808} \quad \propto \quad & \sum_k \sqrt{\left\{\left[\frac{d\hat{L}(\eta_{1808})}{d\hat{\dot{M}}}\right]^2 + 1\right\}} \\ & \times \exp\left\{\frac{-[\hat{\dot{M}}_k - \hat{\dot{M}}_{1808}]^2}{0.5}\right\}\end{aligned} \tag{2.13}$$

Similarly, for 1H 1905, both luminosity and accretion rates are upper limits and hence both Gaussian contribute nothing when the calculated values are higher than their upper

limits.

$$\exp\left\{\frac{-[\hat{L}_k(\eta_{1905})-\hat{L}_{1905}]^2}{0.5}\right\}=1 \quad \text{if} \quad \hat{L}_k \leq \hat{L}_{1905}$$
$$\exp\left\{\frac{-[\hat{L}_k(\eta_{1905})-\hat{L}_{1905}]^2}{0.5}\right\}=0 \quad \text{if} \quad \hat{L}_k > \hat{L}_{1905} \tag{2.14}$$

and

$$\exp\left\{\frac{-[\hat{\dot{M}}_k-\hat{\dot{M}}_{1905}]^2}{0.5}\right\}=1 \quad \text{if} \quad \hat{\dot{M}}_k \leq \hat{\dot{M}}_{1905}$$
$$\exp\left\{\frac{-[\hat{\dot{M}}_k-\hat{\dot{M}}_{1905}]^2}{0.5}\right\}=0 \quad \text{if} \quad \hat{\dot{M}}_k > \hat{\dot{M}}_{1905} \tag{2.15}$$

So

$$\mathcal{L}_{1905} \propto \sum_k \sqrt{\left\{\left[\frac{d\hat{L}(\eta_{1905})}{d\hat{\dot{M}}}\right]^2+1\right\}} \tag{2.16}$$

So the total likelihood contribution form SXRT stars look like

$$\mathcal{L}_{\rm SXRT} \propto \prod_j \mathcal{L}_{{\rm meas},j} \times \mathcal{L}_{1808} \times \mathcal{L}_{1905} \tag{2.17}$$

Stars with Mass-Radius Measurements

Just like SXRTs, low-mass X-ray binaries (LMXBs, neutron stars with a low-mass companion) have intermittent accretion and quiescence phases. This accreted mass in the NS accretion disk eventually falls on the NS surface and causes energy outbursts that are observable in the X-ray regime and have high luminosities [120]. We use the seven QLMXBs detected by Chandra and XMM-Newton in the globular clusters described in Ref. [120] (see the references therein). These are the binary systems in the globular clusters ω Cen, NGC 6397, M28, M13, NGC 6304, X7 and M30. These stars can have both hydrogen or helium atmospheres except for the QLMXB in ω Cen, which is known to have a hydrogen atmosphere. Ref. [120] calculated mass-radius posterior distributions of these QLMXBs that are shown in Fig. 2.3, 2.4 and 2.5. We use more recent data for M30. Additionally, two NICER pulsars PSR J0030+0451 [104, 76] and PSR J0740+6620 [105, 77] were recently analyzed by Riley and Miller to have hydrogen atmospheres, and they are included in our analysis. Their mass-radius distribution is depicted in Fig. 2.5.

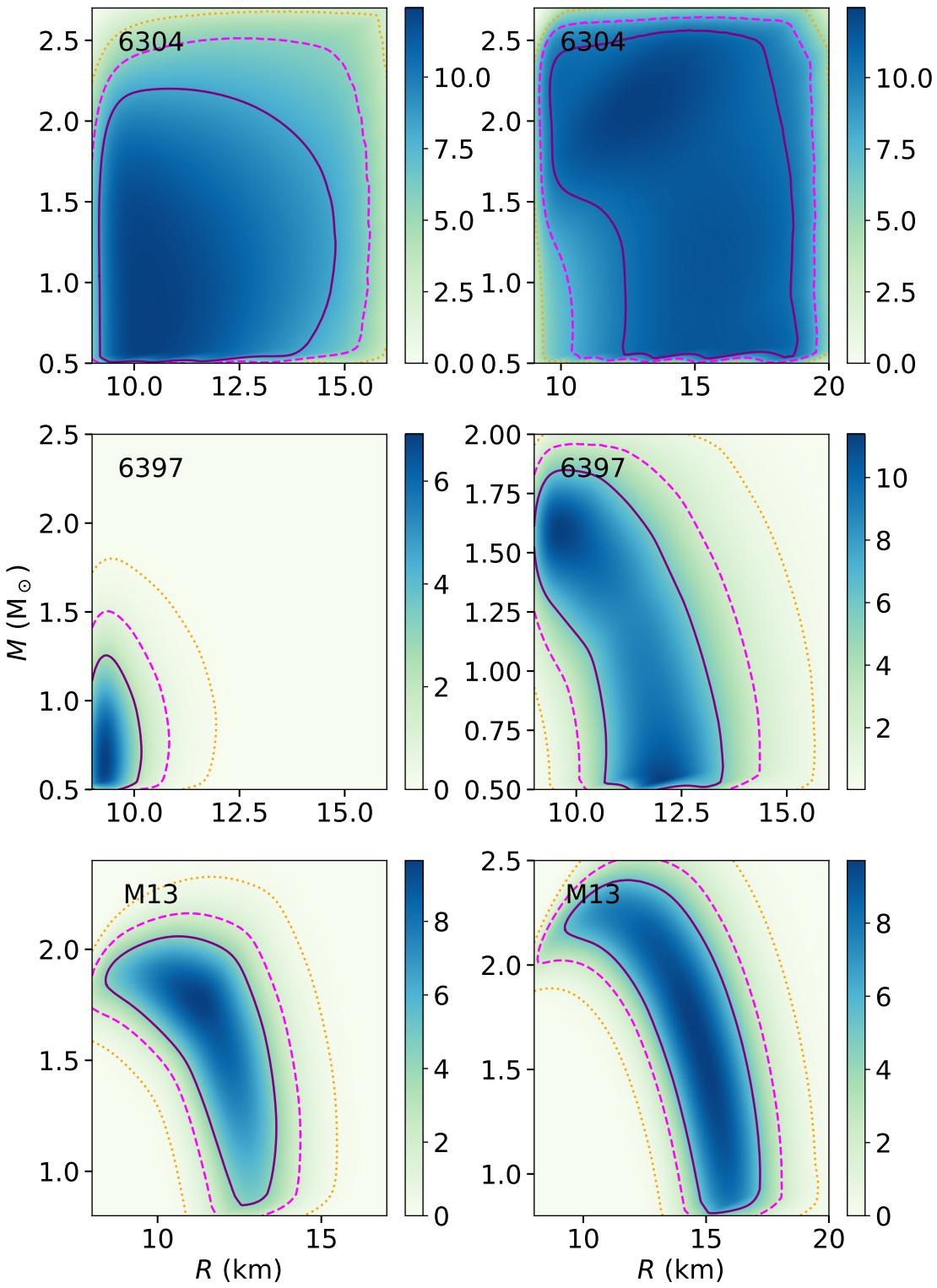


Figure 2.3: Mass-radius relationship of the quiescent low mass X-ray binary stars in the globular clusters from Ref. [120]. The density plots show the hydrogen atmosphere on the left and the helium atmosphere on the right. The contours show 68%, 90%, and 99% confidence intervals. The helium atmosphere supports a larger radius.

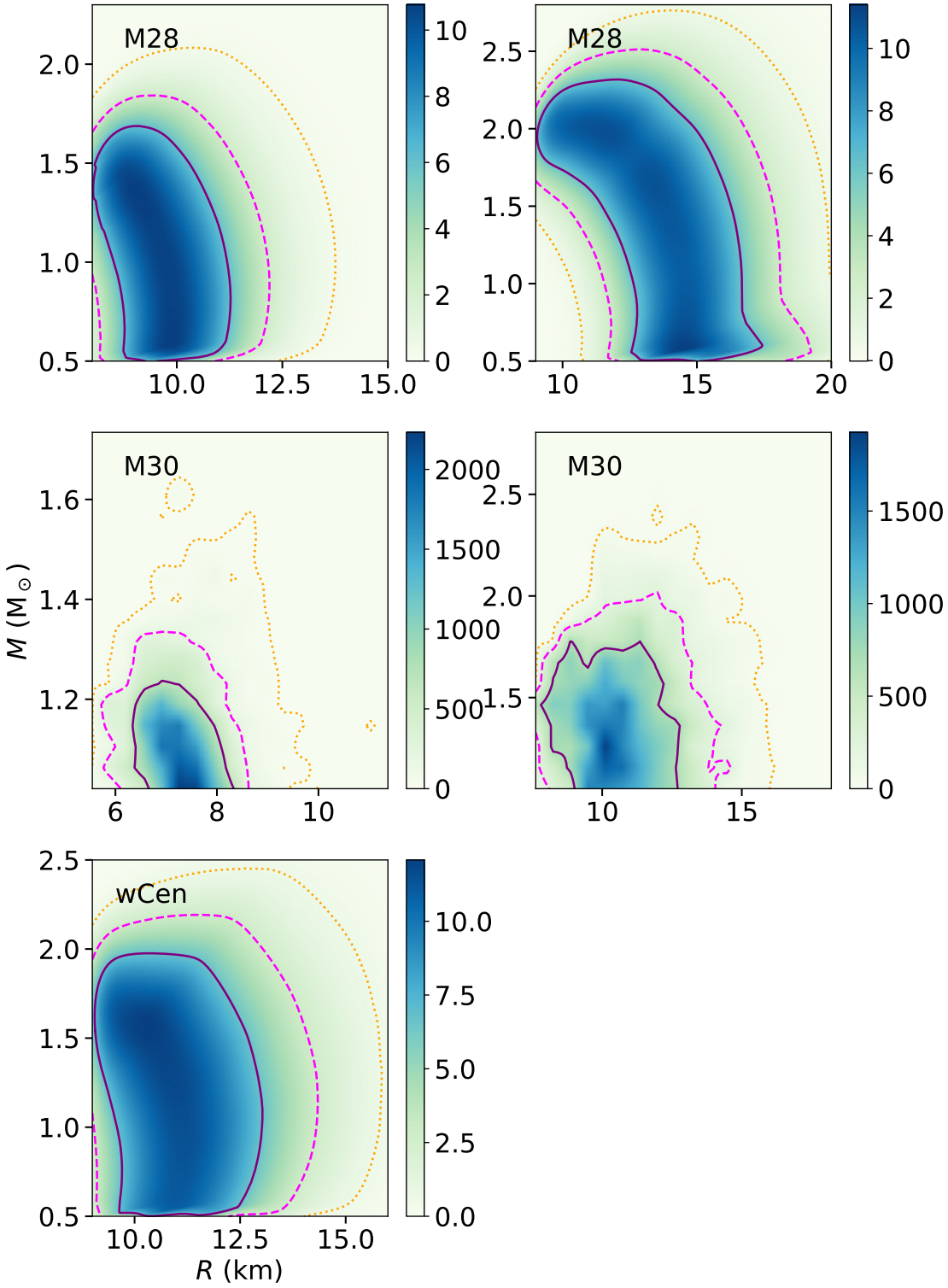


Figure 2.4: Quiescent low mass X-ray binary stars from [120]. The QLMXB in ωCen globular cluster only has hydrogen atmosphere data available.

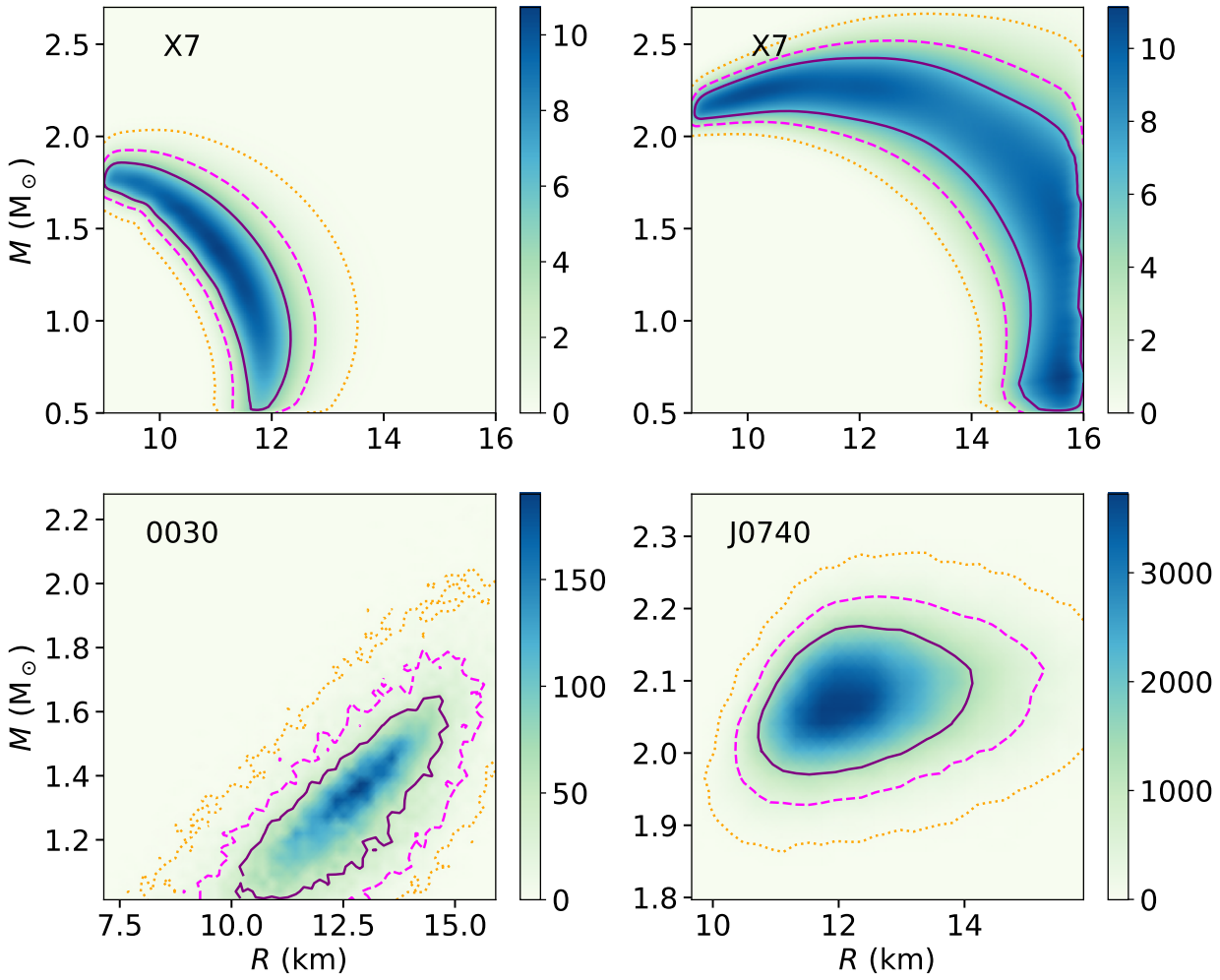


Figure 2.5: Mass-radius relationship of the quiescent low mass X-ray binary star X7 from Ref. [120] in the upper half with hydrogen atmosphere on the left and helium atmosphere on the right. Lower panels are from the NICER stars PSR J0030+0451 [104, 76] and PSR J0740+6620 [105, 77] both with hydrogen atmospheres.

The same likelihood is used as in Ref. [12] (see Eq. 102 of Ref. [68]). The masses and the atmosphere of the stars are parameterized as m_f and ζ_i in the MCMC. This ζ is a random number between 0 and 1 for each star. If $\zeta < 2/3$ a hydrogen atmosphere is chosen for the star and if $\zeta > 2/3$ a helium atmosphere is preferred. Their masses range from 1 $M_\odot$ to the maximum mass predicted by the TOV solver for our EoS.

The total likelihood function for the stars with mass-radius measurements is thus

$$\begin{aligned}\mathcal{L}_{\rm QLMXB} \times \mathcal{L}_{\rm NICER} \quad = \quad & \prod_{i=1}^{9} \{\theta(2/3-\zeta_i)\mathcal{D}_{i,\rm H}[R(M_i), M_i] \\ & +\theta(\zeta_i - 2/3)\mathcal{D}_{i,\rm He}[R(M_i), M_i]\}\end{aligned} \tag{2.18}$$

where M_i is the mass of the ith star, ζ_i are the atmosphere parameter, R_i are the radius, and $\mathcal{D}_{i,\rm H}$ and $\mathcal{D}_{i,\rm He}$ are the probability distributions considering either a hydrogen or a helium atmosphere (see Ref. [12] for details).

Gravitational Waves

Einstein first predicted the existence of ripples through spacetime in his theory of relativity in 1916. Massive accelerating objects send out these ripples known as gravitational waves at the speed of light and carry vital information about the source of their origin. Relative to X-rays or photons, these gravitational waves (GW) seldom interact with matter and hence have less systematic uncertainties when detected. The first proof of the existence of GW was given by Hulse and Taylor in 1974 when they detected a binary system that matched the radiation patterns of GW. In 2015 Laser Interferometer Gravitational-wave Observatory (LIGO) observed the first GWs from a binary black hole merger, a pivotal moment in human history. LIGO-VIRGO collaboration detected GW signal from a binary NS merger in 2017 [2] and made precise measurements of the chirp mass $M_{\rm chirp} \equiv (m_1 m_2)^{3/5}/(m_1+m_2)^{1/5}$ and the tidal deformabilities, a measurement of how tidal forces from one star deforms the other one. Since the tidal deformability Λ is directly correlated to the stellar radius, observations of more GW sources would be vital in mass-radius measurements and constraining the EoS.

For the neutron stars in GW170817 [2], we use kernel density estimation to convert the Monte Carlo samples from Ref. [3] to a three-dimensional probability distribution over the chirp mass $M_{\rm chirp}$, the mass ratio q, and the tidal deformability $\tilde{\Lambda}$ (see fig. 2.6, [5]). The masses of the two neutron stars involved in the merger are sampled from a uniform distribution from 1 solar mass to the maximum mass. The tidal deformability for the two neutron stars is computed from the moment of inertia using the Yagi-Yunes correction [139] as formulated in Ref. [138].

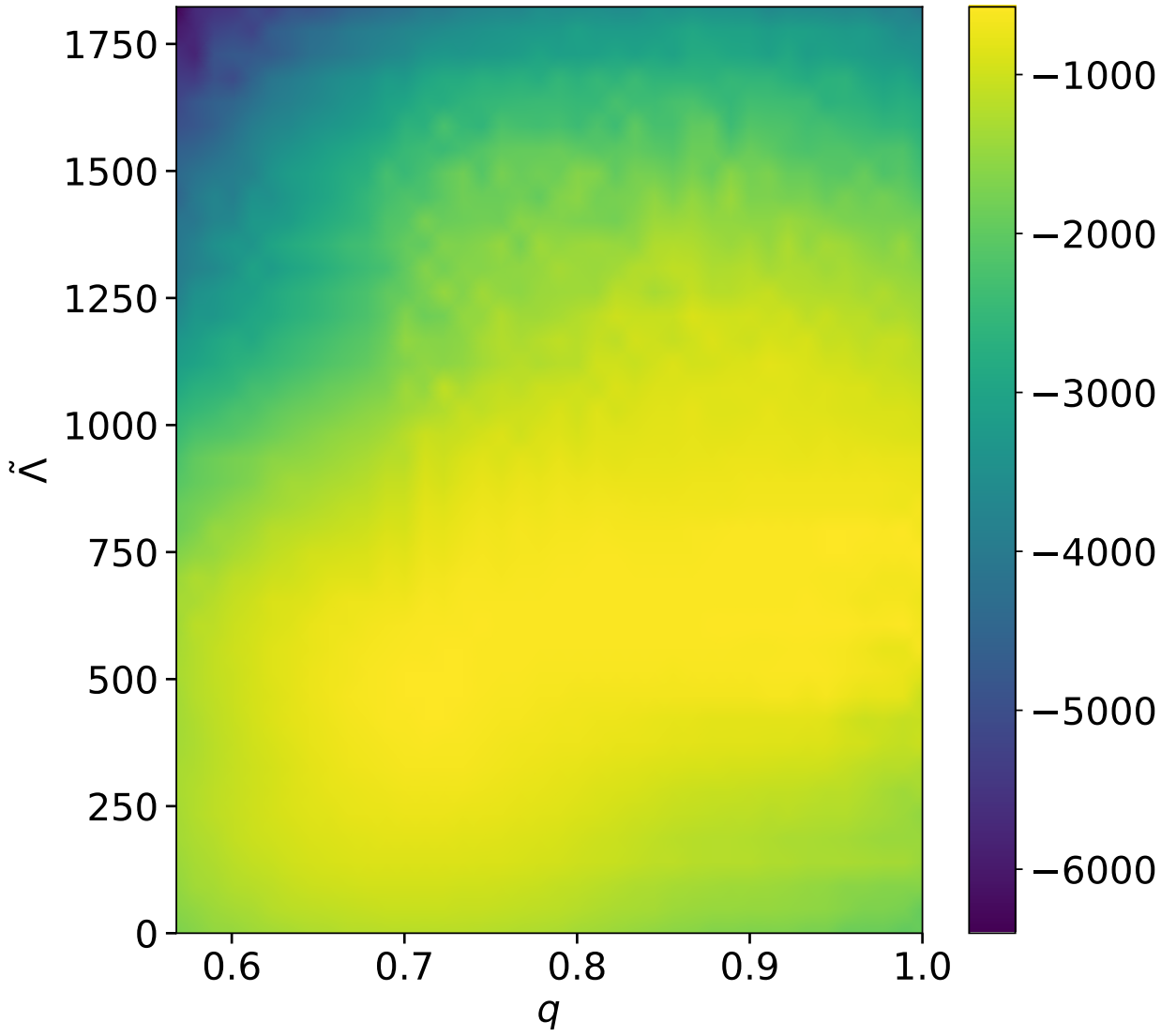


Figure 2.6: Probability distribution of mass ratio q and tidal-deformability $\tilde{\Lambda}$ of GW170817 [2] using Kernel density estimation [5].

$$m_1 = M_{\rm chirp} \times \frac{(1+q)^{1/5}}{q^{3/5}}$$
$$m_2 = M_{\rm chirp} \times \frac{q^{2/5}}{(1+q)^{1/5}} \tag{2.19}$$

where m_1 and m_2 are the individual masses of the binary. Now the moment of inertia is

$$\bar{I}_1 = I_1/g^2 m_1^3$$
$$\bar{I}_2 = I_2/g^2 m_2^3 \tag{2.20}$$

using the fit parameters from eq. 25 in Ref. [122]

$$\begin{aligned}\ln \lambda_1 = -30.5395 + 38.3931 \ln \bar{I}_1 - 16.3071(\ln \bar{I}_1)^2 \\ +3.36972(\ln \bar{I}_1)^3 - 0.26105(\ln \bar{I}_1)^4 \\ \ln \lambda_2 = -30.5395 + 38.3931 \ln \bar{I}_2 - 16.3071(\ln \bar{I}_2)^2 \\ +3.36972(\ln \bar{I}_2)^3 - 0.26105(\ln \bar{I}_2)^4\end{aligned} \tag{2.21}$$

Finally, the tidal deformability is

$$\tilde{\Lambda} = \frac{16}{13} \frac{(m_1 + 12m_2)m_1^4 \lambda_1 + (m_2 + 12m_1)m_2^4 \lambda_2}{(m_1 + m_2)^5} \tag{2.22}$$

We parameterize $M_{\rm chirp}$ and q in our MCMC and compute $\tilde{\Lambda}$. The probability distribution from Ref. [5] then gives us the likelihood for GW170817 from the values of $M_{\rm chirp}$ and q.

2.3 Model Summary

The EoS has 17 parameters. For each neutron star, we add a parameter for its mass to locate that object on the neutron star mass-radius curve (60 parameters). These are typically taken from uniform distributions except in the case of GW170817, where the masses are taken from uniform priors in $M_{\rm chirp}$ and the mass ratio, q. For INSs and SXRTs, each neutron star also has an additional parameter to describe the composition of the neutron star envelope (40 parameters). For INSs, we have 17 stars with additional age parameters because only an upper limit to their age is known. Also, we have a parameter for the time-averaged accretion rate of 1H 1905 ($\dot{M}_{1905}$) because the observations provide only an upper limit to this accretion rate. For the QLMXBs, we have an additional parameter to describe the composition of the neutron star atmosphere, either hydrogen or helium (6 parameters), as in Ref. [119]. We have

six parameters for neutron superfluidity and proton superconductivity. As in Ref. [47], we add a parameter (Q) to the model for the amount of deep crustal heating and an additional parameter (α) to model the broadening of the threshold of the direct Urca process by nuclear many-body effects. We thus have a total of 151 parameters (see Table. 2.1).

Table 2.1: Parameter set for our MCMC and their brief descriptions

Parameter	Description
$\log_{10} T_{c,\mathrm{peak},n}$	Critical temperature for neutrons
$k_{F,\mathrm{peak},n}$ (fm^{-1})	Peak Fermi-momenta for neutrons
$\Delta k_{F,n}$ (fm^{-1})	Width of the Gaussian for neutrons
$\log_{10} T_{c,\mathrm{peak},p}$	Critical temperature for protons
$k_{F,\mathrm{peak},p}$ (fm^{-1})	Peak Fermi-momenta for protons
$\Delta k_{F,p}$ (fm^{-1})	Width of the Gaussian for protons
c_ρ, c_σ, c_ω	the meson-nucleon couplings
m_σ	the σ meson mass
b, c, ζ, ξ	meson couplings from Ref. [78]
$b_{1,2,3}$ and $a_{1,2,3,4,5,6}$	higher-order meson couplings from Ref. [124]
α	The direct Urca broadening parameter
Q	The heating parameter
M_{chirp}, q	The chirp mass and mass ratio from GW 170817
$\hat{\dot{M}}_{1905}$	Accretion rate of 1H 1905
$m_{f,i}$	masses of the stars parameterized as mass fraction
$\log_{10} \eta_i$	atmosphere parameter of the INS and SXRTs
ζ_i	atmosphere parameter for QLMXB stars

2.4 Bayesian Inference

We employ Bayesian inference with uniform prior distributions for our parameters, as detailed below. We also presume that all the neutron star observations are statistically independent. With the individual likelihood contributions in place, our full likelihood function looks like

$$\mathcal{L} = \mathcal{L}_{\rm nuclei}\mathcal{L}_{\rm LIGO}\mathcal{L}_{\rm INS}\mathcal{L}_{\rm QLMXB}\mathcal{L}_{\rm NICER}\mathcal{L}_{\rm SXRT} \tag{2.23}$$

Given the prior distributions $P(M)$ of our 151 parameters, the likelihood function is the probability of the data given the model $P(D|M)$. Once we compute the likelihood for a model, the Bayesian equation gives us the probability of the model given the data [12].

$$P(M|D) \propto P(D|M)P(M) \tag{2.24}$$

We use the Markov chain Monte Carlo (MCMC) method to sample from this distribution of our large dimensional parameter space. At each MCMC point, we perform a grid of cooling simulations over several neutron star masses and three envelope compositions and then interpolate the cooling curves to obtain the cooling curve for each neutron star. We use affine-invariant sampling [43] to construct a training set computing the likelihood, satisfying all the physics constraints, and use this to construct a kernel density estimator (KDE) for the full likelihood and use that KDE as the distribution in an independent Metropolis-Hastings run to compute the final results. Because the full code is used to compute the final posterior distribution and the KDE is used only for the proposal distribution, inaccuracies in the KDE have less of an impact on the final posterior.

2.5 Kernel Density Estimation

Kernel Density Estimation (KDE) is a non-parametric method for estimating the probability density function of a random variable. Given a data set, it smooths the data points to create a continuous density curve, which can provide insights into the underlying distribution of the data without making strong assumptions about its shape.

The fundamental idea behind KDE is to place a kernel function K, typically a Gaussian, at each data point and sum these kernels to produce the overall density estimate. Generally, the KDE of a dataset $\{x_1, x_2, \ldots, x_n\}$ can be described as:

$$\hat{f}(x) = \frac{1}{nh}\sum_{i=1}^{n} K\left(\frac{x - x_i}{h}\right) \tag{2.25}$$

Where $\hat{f}(x)$ is the estimated density at point x, h is the bandwidth parameter that controls the degree of smoothing, and n is the number of data points. The choice of bandwidth h is crucial, as a small bandwidth may lead to overfitting (too much noise), while a large bandwidth may oversmooth the data, obscuring important features. For our problem, the KDE implementation from Scikit-learn [94] with Gaussian kernel was used to probe the posterior after generating around 150000 unique data points that sufficiently explored the parameter space.

Chapter 3

Results

Fig. 3.1 shows the values inferred from observations and posterior distributions for the luminosity for each of the INSs as a function of time. The lower-right panel of Fig. 3.2 shows the values inferred from observations and posterior distributions for luminosity as a function of the time-averaged mass accretion rate for each of the SXRTs.

Less-luminous isolated neutron stars like J0007, B1727, J1957 and the low-luminosity SXRTs like J1808 are difficult to explain without a large contribution from the direct Urca process, which, in turn, requires a large proton fraction. Fig. 3.3 shows the extensive range of proton fractions explored in our MCMC and the very tightly constrained posterior distribution. The proton fraction must exceed the $\sim 10\%$ requirement at about twice the nuclear saturation density.

Fig. 3.4 shows the posterior distributions for several other quantities of interest. The peak critical temperatures associated with the proton singlet gap and the neutron triplet gap shown in the upper-left panel, both match the results obtained in the previous works analyzing the neutron star cooling data [91, 93]. The specific heat of 1.4 solar mass stars is strongly constrained to be around 1.0×10^{38} erg K^{-1}, within the expected range [25, 71]. Note that the specific heat drops precipitously for stars with masses larger than 1.4 $\mathrm{M}_{\odot}$, to partially (but not fully) quench the direct Urca process with pairing from the neutron triplet superfluid.

Fig. 3.5 shows luminosity vs. gravitational mass posteriors for the INSs and SXRTs. The luminosity is nearly flat for $M < 1.4\ M_{\odot}$. For larger masses, the luminosity drops, principally because of the direct Urca process. The Fig. 3.6 shows the mass posterior distribution for INSs. The uncertainties shown here are likely an underestimate because there are not enough observations at each mass to provide an accurate probability distribution. Nevertheless, except for selection effects, this mass distribution should be similar to the NS mass distribution generated by core-collapse supernovae.

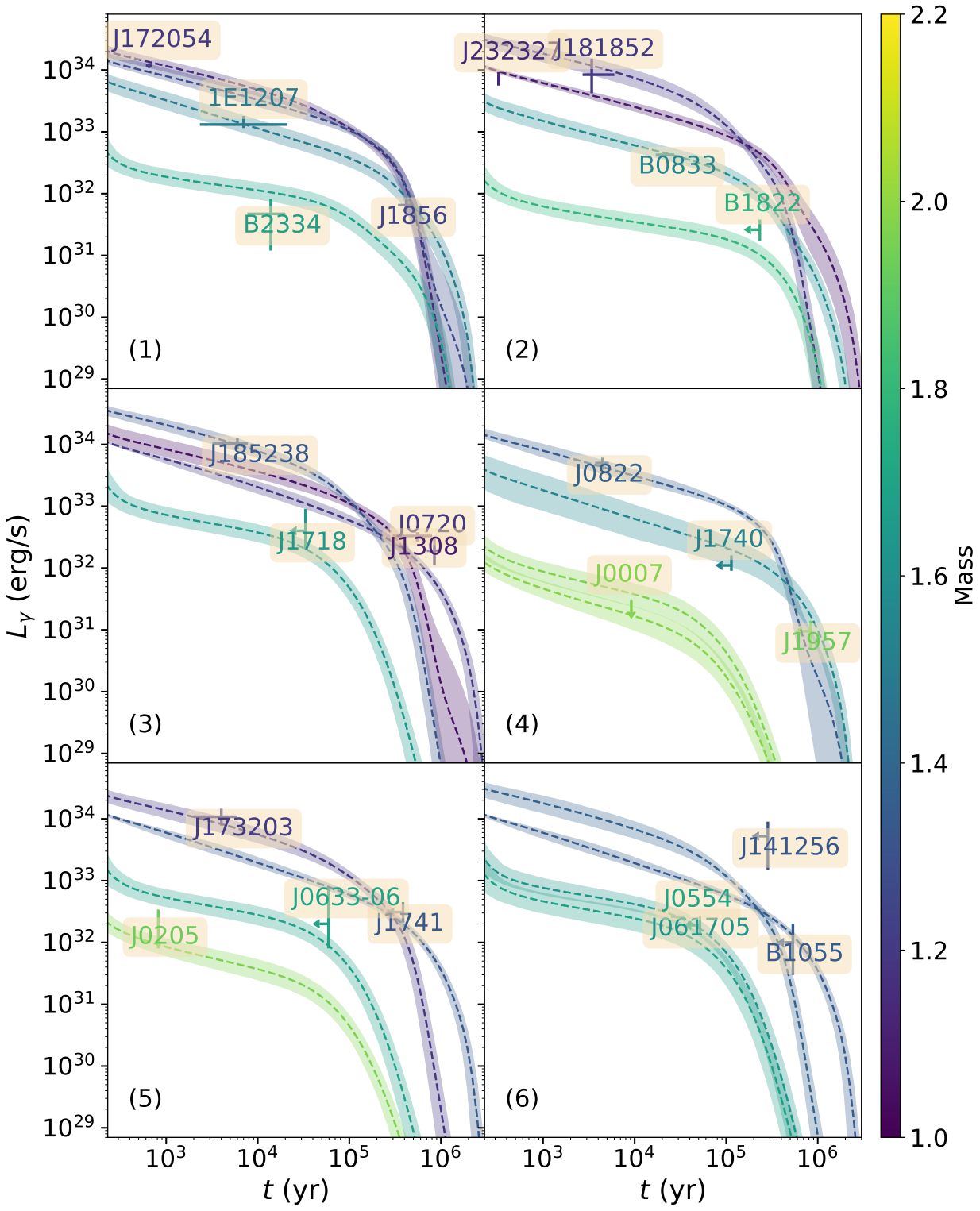


Figure 3.1: Cooling curves and their 68% credible intervals for the isolated neutron stars (panels 1-11). The luminosities and ages inferred from observations are given, along with the bands for the posterior distributions. The color of the bands gives the posterior neutron star mass. Most of the stars cool via slower cooling processes and have a cooling curve that is flatter in the early stages.

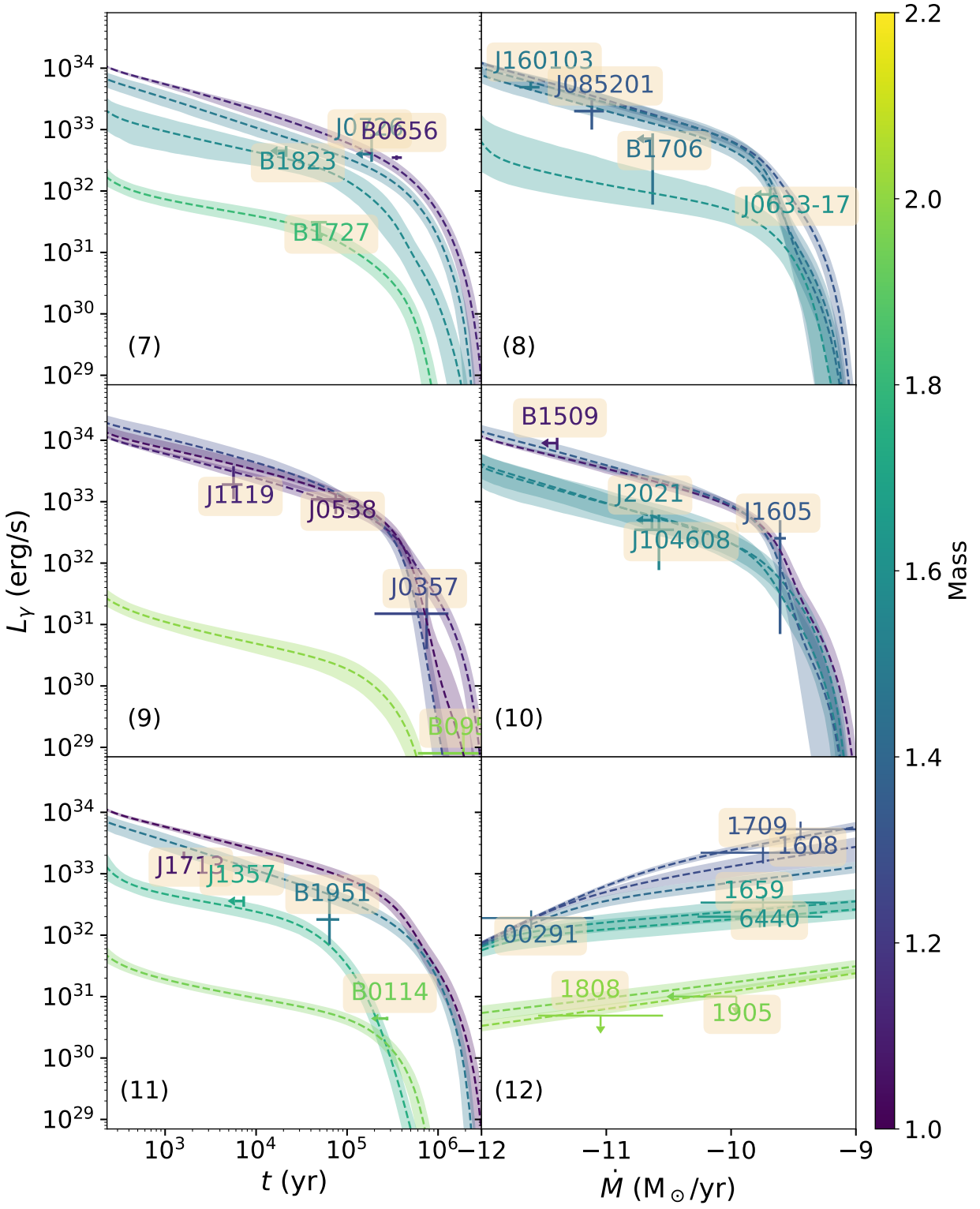


Figure 3.2: Some stars, like J0007 (panel 4) and B1727 (panel 7) are cooling partially via the direct Urca process and thus cool much faster at earlier times. Panel 12 shows the SXRT luminosity as a function of their inferred time-averaged accretion rate.

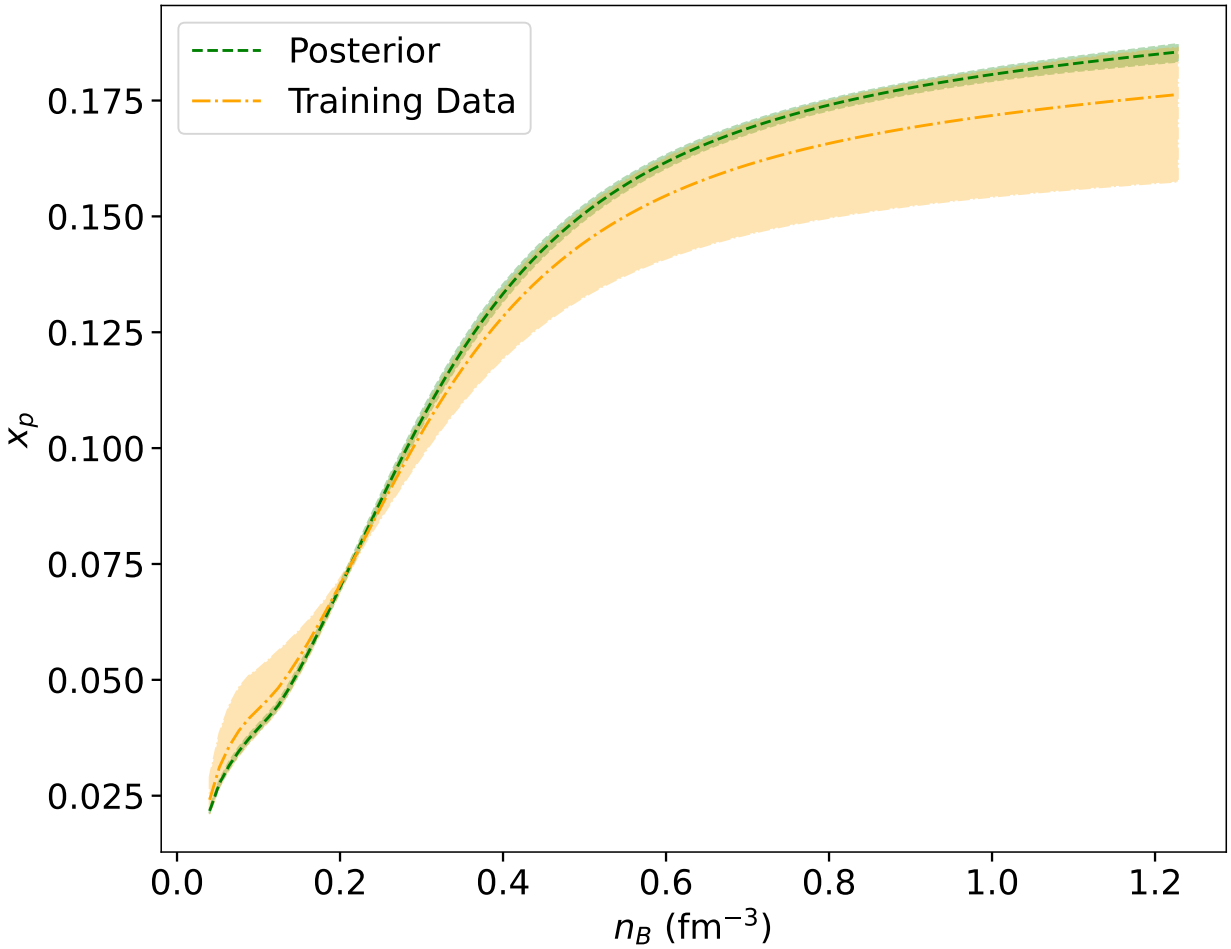


Figure 3.3: The range between the minimum and maximum proton fraction of the KDE training set and 68% credible intervals for the number of protons per baryon, x_p, as a function of the baryon number density n_B. We find a very tight constraint on the composition of dense matter.

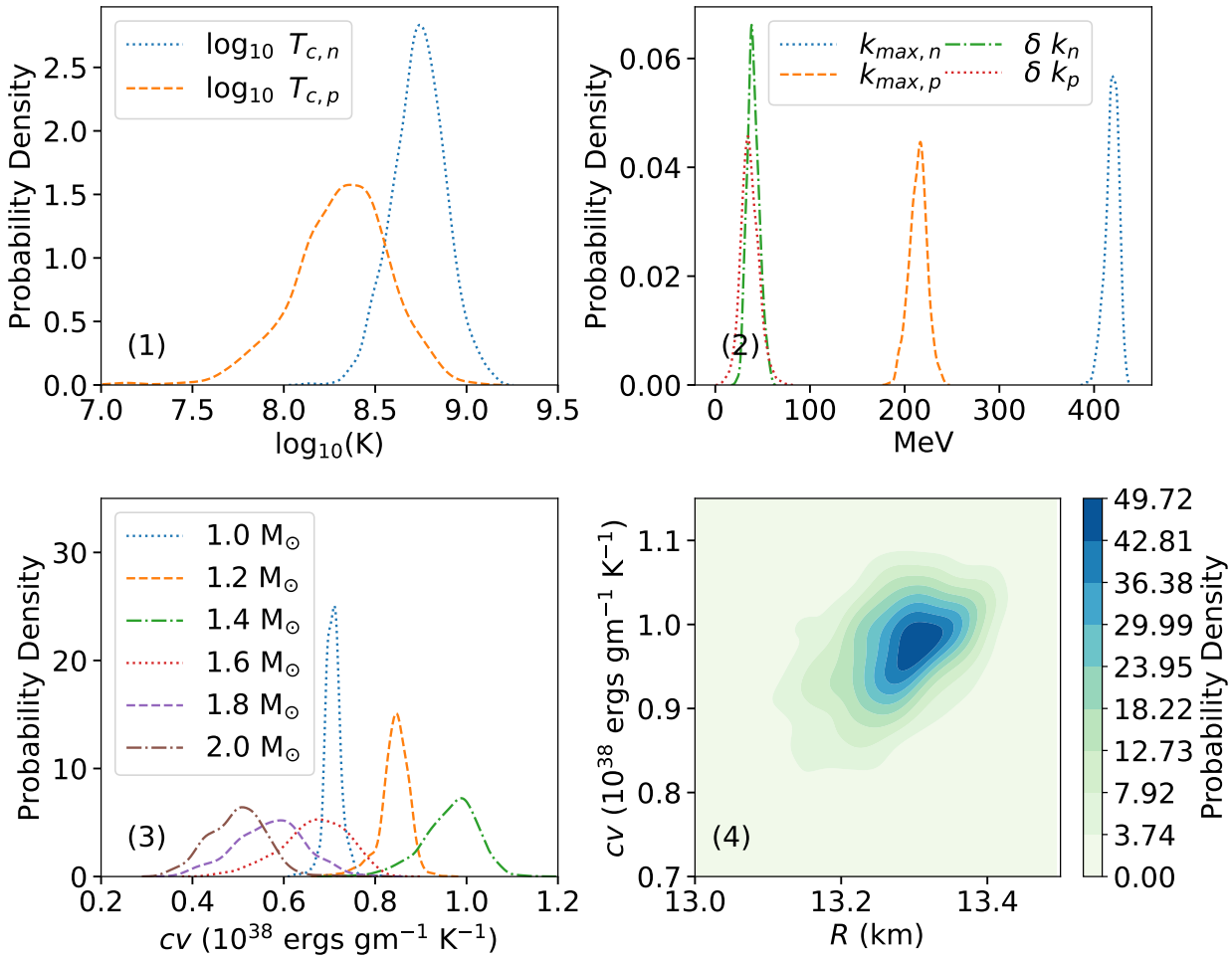


Figure 3.4: Panel (1) shows the posterior distribution for the maximum critical temperatures. Panel (2) shows the posterior distributions for the remaining superfluid parameters. Panel (3) shows the posterior for the specific heat as a function of mass and panel (4) shows the correlation between neutron star radius and specific heat of a 1.4 $M_\odot$ neutron star. This correlation is broken for higher masses because of the neutron triplet superfluid.

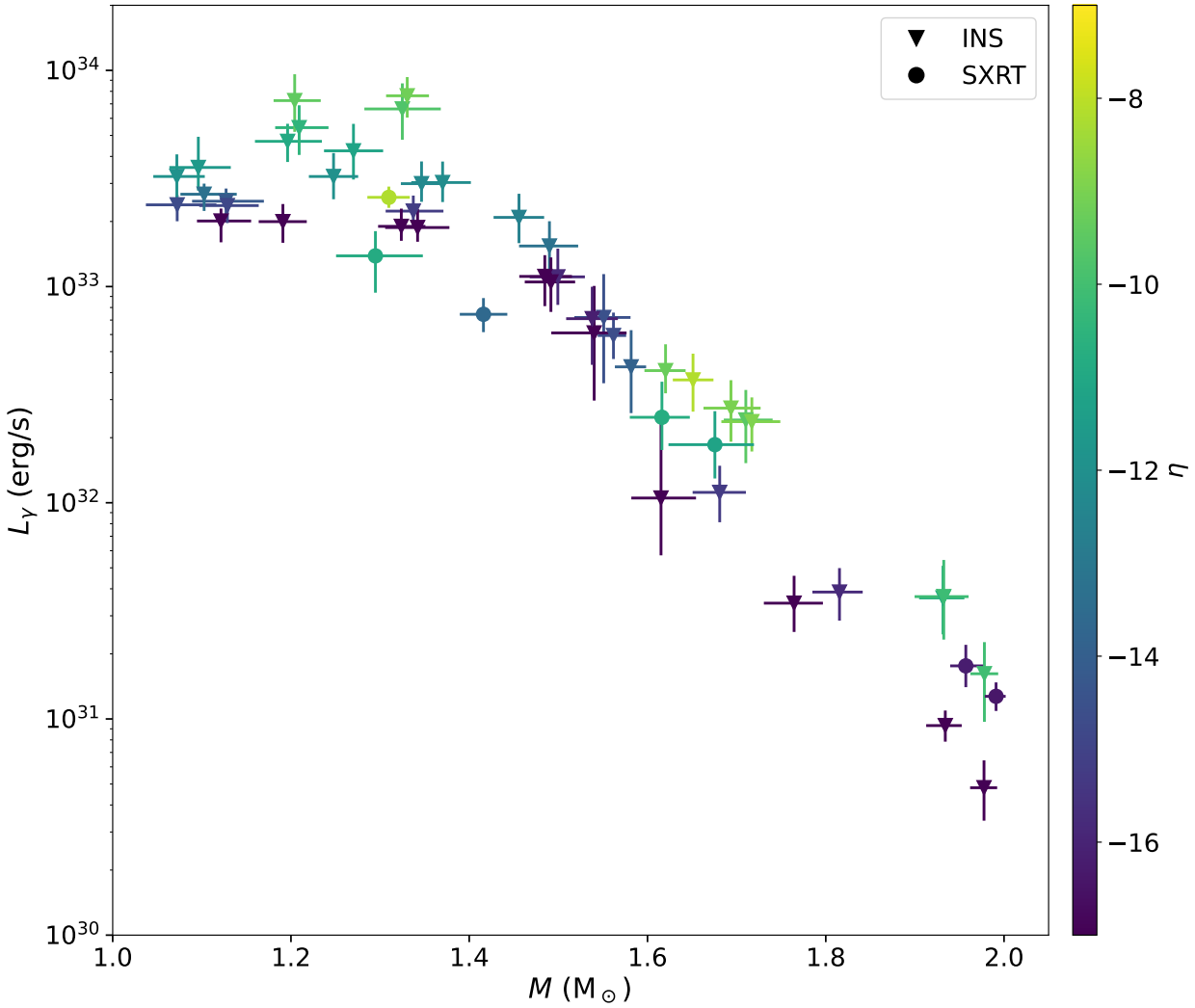


Figure 3.5: Approximate posterior distributions for the mass and luminosity of each of the INSs (triangles) and SXRTs (circles) with uncertainties. η represents the amount of light elements in the envelope. Below 1.4 $M_\odot$ luminosity has less dependence on stellar mass. Above 1.4 $M_\odot$, enhanced cooling processes are active, and the luminosity drops as a function of mass almost linearly.

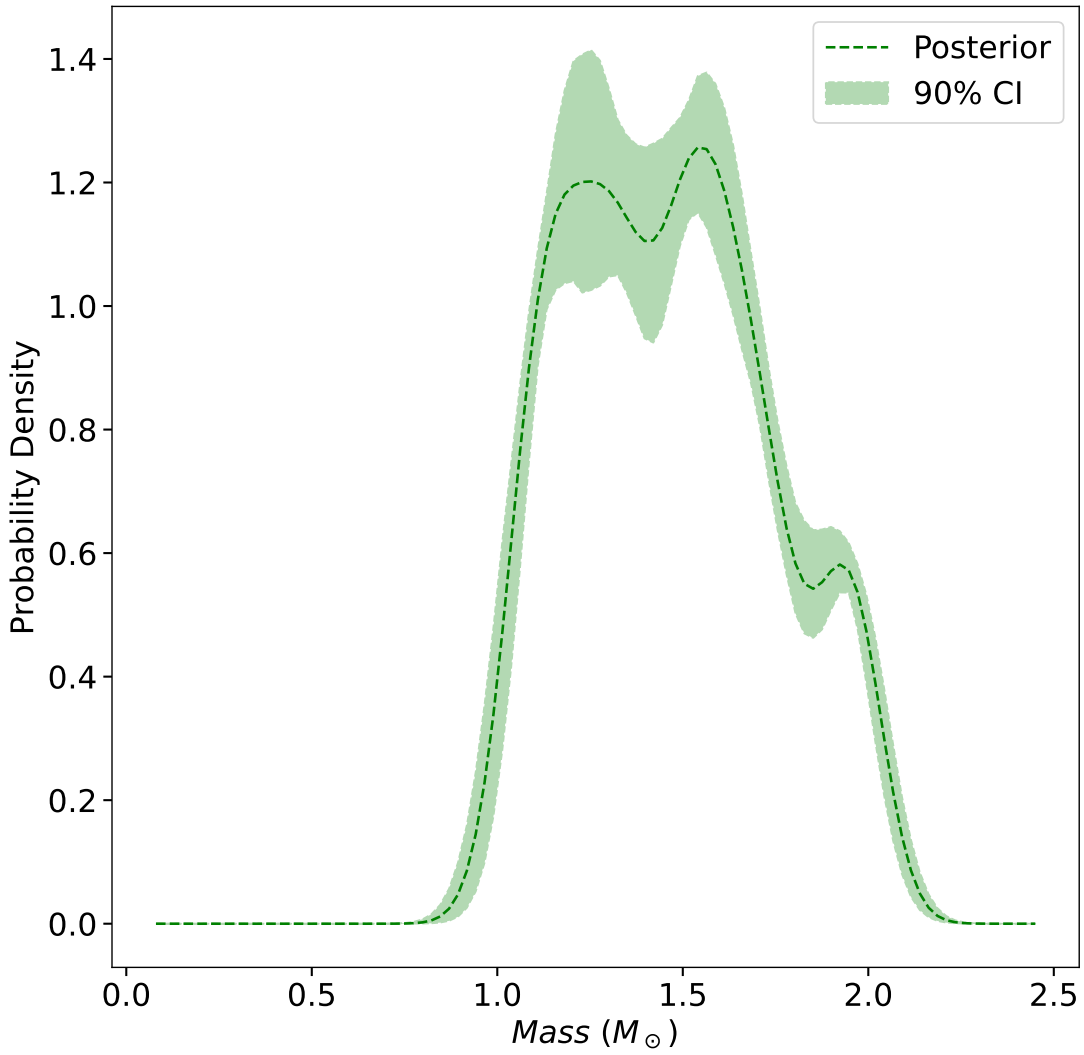


Figure 3.6: The posterior INS neutron star mass function as approximated by a kernel density estimator applied to the INS mass posteriors. A bulk of NS is around the canonical mass of 1.4 $M_\odot$. The colder NS supports a larger mass $\sim 2\ M_\odot$.

3.1 Discussion

Our work tries to constrain RMF-EoS and superfluidity parameters quantitatively given the current observations from multi-messenger astronomy and nuclear experiments. The likelihood function we employ can produce full posterior for the parameter values in contrast to previous works [13]. The choice to utilize Bayesian analysis enables us to use the least amount of constraints while fitting the models to the data. Ref [106] studied proto-neutron star (PNS) cooling directly after a supernova and found a direct connection between convection and symmetry energy at higher densities.

Cooling models beyond the "minimal cooling" have been previously explored by Ref. [131] that had hyperons in the stellar core and deduced strong superfluidity is necessary otherwise the hyperonic direct Urca channels cool the stars beyond their observed luminosities. Ref. [144] studied NS cooling with nucleon and hyperon cores and concluded that hotter NS have lower mass and colder NS have higher mass. However, they couldn't quantitatively comment on the nature of superfluidity with the observations they had available, and they hinted at including other observations to get better results. Our model is more encompassing as we take thermal emissions from quiescent stars into account and have constraints arising from the X-ray emissions from the QLMXBs and gravitational waves on the mass-radius relation. Ref. [28] explored the possibility of direct Urca processes from neutrons and protons being able to explain the observations without the need for exotic particles and concluded that apart from a few stars, most stars are explainable by "minimal cooling" as long as different envelope compositions are taken into account. Ref. [98] studied the thermal evolution of a magnetized NS of 1.4 $M_\odot$ with standard nuclear matter and hydrogen and iron envelopes to produce a fit to the observed data. However, they used a static description of the magnetic field that was decoupled from the cooling. Ref. [73] provides an extensive review of magnetars that discuss this relationship in full detail. Ref. [13] analyzed the thermal evolution of INS and SXRTs in a statistical way much like ours and put constraints over the direct Urca threshold broadening. Their result showed a distinct separation in the NS population by the threshold mass $M_{\rm Durca} = 1.72\ M_\odot$ above which direct Urca was permitted. A careful envelope composition with different amounts of light elements can close this gap without incorporating threshold broadening. However, they used a fixed EoS model for demonstration purposes. In contrast to this, we use an EoS model that can be varied to fit the data better. Recent studies in Ref. [108] have also incorporated the PREX-2 results of larger symmetry energy with INS cooling that allows larger proton fraction for direct Urca inside the star. While they have used canonical NS masses with an iron envelope, in our model, the NS masses and the envelope composition are parameterized to fit the data and produce a posterior that can be insightful (see Fig. 3.5 and Fig. 3.6). Ref. [26] has recently done a combined analysis of NS cooling and mass distributions with nuclear matter, V18 BHF EoS, and proton superfluidity.

While there is still some systematic uncertainties, their result aligns with ours on the need for "enhanced cooling" for current observations.

Individual cooling NS have garnered some attention like Cas A where Ref. [55] performed a χ^2 fit to the data assuming an iron or a thin carbon envelope with BSk21 EoS and a phenomenological superfluidity model to explain this rapidly cooling NS. Ref. [81] employs a quark color superconducting (CSC) phase with a large energy gap to explain Cas A cooling. XMMU J1731 was analyzed by Ref. [85] assuming a superconducting stellar core and a carbon atmosphere to put constraints on the mass-radius of the star. Our EoS and superfluidity parameters are independent by design which is different from this approach.

The isolated neutron star cooling observations strongly favor larger radii. The origin of this constraint appears to lie in part due to the specific heat: the specific heat must be sufficiently large to ensure a sufficiently flat cooling curve at early times for lower-mass stars. This may indicate a tension with gravitational wave observations, which suggest a smaller radius for GW 170817. There are three ways to resolve this tension, either (i) GW 170817 is an outlier and future GW constraints will suggest larger radii, (ii) there are some unaccounted for systematic uncertainty in the isolated neutron star observations, (iii) the assumption of purely nucleonic matter is incorrect. With regard to the possibility of systematic uncertainty, there are three possibilities covered in the literature: (i) the surface temperature is non-uniform (e.g., Refs. [96, 133]), (ii) magnetic fields play an important role (e.g., Ref. [97]), or (iii) there is a strong many-body correction to the neutrino emissivities which explains the data (e.g., Ref. [15]). Because we have restricted our data set to objects for which $B < 10^{14}$ G, we minimize the direct impact of magnetic fields on the cooling curve, but even smaller fields can cause polar hot spots that lead to nonuniform surface temperatures. Surface temperature variations can shift the luminosities (and thus the requirements on the specific heat), but they cannot fully explain low-luminosity neutron stars without a contribution from the direct Urca process (even if the temperature variations came from a magnetic field). The extant many-body corrections that could modify the neutrino emissivity would require other degrees of freedom (such as significant contributions from pions), and thus violate our original model assumption.

Another possibility is that our original assumption of only neutron and proton degrees of freedom is false (e.g., Ref. [7]). There are models [112] that incorporate axion (light pseudoscaler dark matter particles) cooling through pair breaking formation without direct Urca however their models are limited to 1.8 $M_\odot$ which is lower than the currently observed maximum NS mass. Nevertheless, we have shown for the first time that neutron star cooling observations are unmatched in their ability to provide quantitative information on the composition and specific heat of dense matter.

Chapter 4

Modular Unified Solver of the Equation of State (MUSES)

As we continue to explore the thermal evolution of neutron stars to put constraints on dense matter physics, several EoS models exist that have tried to answer the same questions that we have. Combining these EoS models and comparing them with each other can provide greater detail and create a broader picture in this field. This is especially useful for those doing supernova simulations or heavy-ion collisions, who rely on the EoSs to explain the underlying physics. Modular Unified Solver of the Equation of State (MUSES) is an important initiative in this regard. It is an NSF-funded collaboration project working on creating a cyberinfrastructure to bring all EoS efforts together under one umbrella. This includes EoS theories like chiral mean field theory, chiral effective field theory, or crust density functional theory. The goal is to provide a general proposed solution for those in different scientific communities that are interested in dense matter EoS.

This is done primarily by converting old EoS codes to new standards that are easily understandable, well documented, and can be run without being concerned about prerequisites. Over time, this will help communications between different branches of EoS interested parties be much easier. MUSES relies on a cloud-native deployment system based on the latest container technologies. A reproducible environment can be created either in the cloud or on an individual user's local machine giving the user full control over their computing and data. For a more in-depth look, see Ref. [33].

4.1 Calculation Engine

The calculation Engine (CE) is the backbone of the MUSES infrastructure that integrates all EoS modules while providing an interface (API) for running workflows that involve one or

multiple EoS modules. It is built on a RESTful HTTP API server, an SQL database, a task queue system, and an object store. Registering an EoS module into the CE requires a few steps [33]. The EoS module needs to have a container image with built-in dependencies and the main executable. This image needs to be public and tagged. The source code repository needs to be public and there must be a CI/CD pipeline that builds the container image. The module must be well documented and Sphinx compatible. The execution command needs to be specified and the inputs and the outputs of the EoS module require explicit paths and descriptions.

4.2 Crust Density Functional Theory

Crust Density Functional Theory (Crust-DFT) constructs EoSs for homogeneous nuclear matter with an ensemble of nuclei to be used in astrophysical simulations (e.g. core-collapse supernovae, neutron star mergers, etc.). Crust-DFT is guided by microscopic many-body theory calculations and is empirically constrained by nuclear mass measurements, proton-proton scattering phase shifts, and neutron star observations. Originally described in Ref. [30] and improved upon in Ref. [32] with nuclei, the source code is available on GitHub [31]. There are some prerequisites (see Ref. [31] documentation for more details) that are necessary to compile the code and generate/analyze EoS tables. Some precomputed EOS tables are available to download at Ref. [118] (see Fig. 4.1).

There are several physical regimes inside a neutron star ranging over a large range of baryon density (n_{B}), electron fraction (Y_{e}), and temperature (T) each constrained by different measurements and theoretical approaches. Instead of using a single nucleon-nucleon interaction model everywhere, Crust-DFT delivers a phenomenological free energy density that is consistent in each regime by treating every regime with its underlying assumptions separately. This approach is also better when computing uncertainties, as it can be varied independently in different regimes and is consistent everywhere.

4.2.1 Crust-DFT Integration

MUSES collaboration is working on the properties of dense matter in the zero-temperature limit generated by a collection of different EoS models like Crust-DFT, Chiral Effective Field Theory, and Chiral Mean Field Model, which are more robust than one another at different densities. Lepton contributions are added to each EoS and different matching approaches are used to connect these EoS. Then the combined EoSs are used to compute neutron star properties, its time evolution, and bulk viscosity. For, this project, Crust-DFT $\rightarrow$ Lepton workflow is constructed which gets merged with the other EoS modules to provide

the necessary physics that can be used to obtain the neutron star properties. This is a work in progress.

Docker is a collection of products that utilize OS-level virtualization to provide software in packages known as images and containers. To build an optimal image for Crust-DFT, a multi-stage docker image was built from scratch. There are benefits of using a multi-stage build where the necessary files from building stages can be copied over to the runtime stage and the final image. This keeps the image size small and maintaining the image becomes far easier. The Dockerfile [31] builds have 3 stages. The first stage is built upon Ubuntu-24.04 with the necessary prerequisites installed. Crust-DFT is compiled here. The second stage is built upon the Python3.11-slim image that installs the software packages needed for CE. The third stage is built upon another Python3.11-slim image. Some necessary packages are installed to handle downloads and some specific file types. All the necessary files are copied over from the first and the second stage and the environment parameters are set with the entry point specified. The final image is small and is uploaded to the docker hub for further use.

A new branch 'muses' is created in the Crust-DFT repository [31]. The source code is organized according to MUSES standard with a manifest that specifies the structure of the repository. Physics and source code documentation for Crust-DFT is publicly available and sphinx-compatible. However, containerized execution was new, and proper documentation was added for that in the muses branch. Older documentation was streamlined to be MUSES compatible [33].

Crust-DFT is built with a command line interface (CLI) and Makefile in mind whereas MUSES relies on configuration files. The input configuration of the executable is specified by the user through an input file. The code is executed through a script that reads the input file contents and runs the compiled code with the desired configuration. For MUSES, our primary goal was to make sure MUSES and all of its users can use precomputed EoS tables from Ref. [32]. After some modifications, now the users can generate the tables themselves if they want.

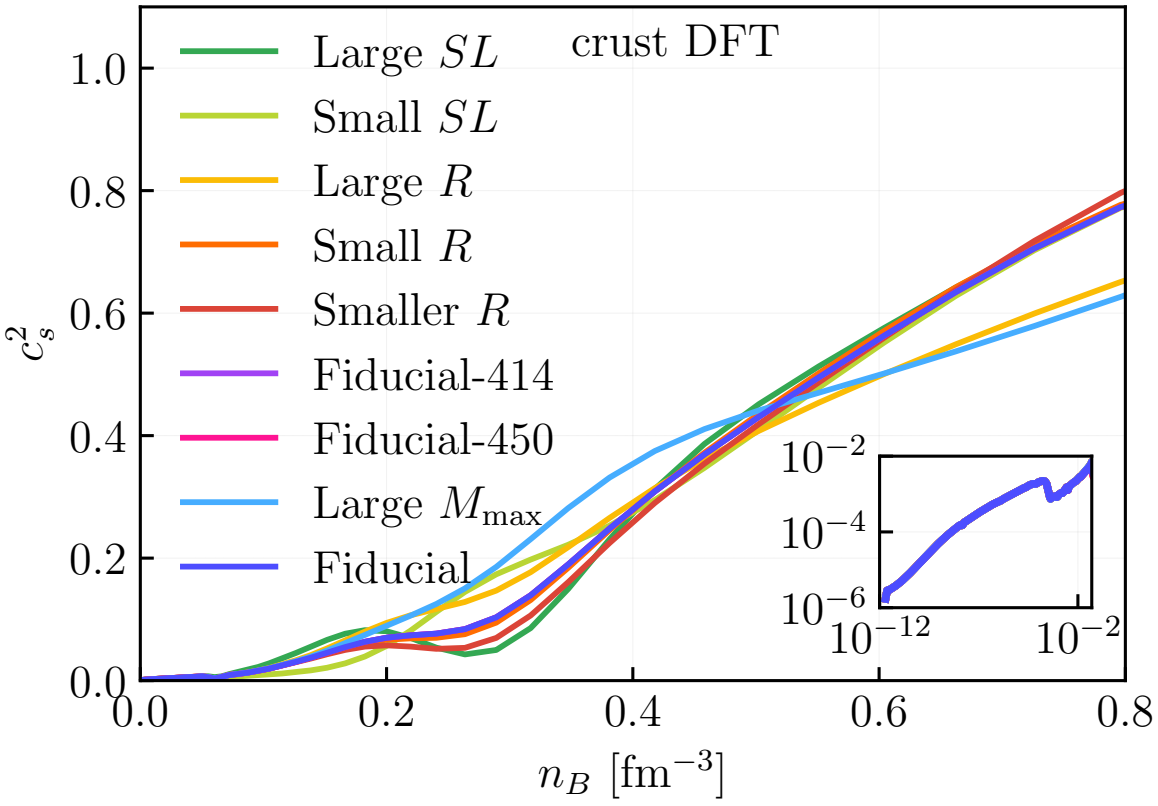


Figure 4.1: Speed of sound comparison from different EoS models of Crust-DFT. The Fiducial model has a kink in the speed of sound near 10^{-2} fm^{-3} which corresponds to the appearance of nuclei. The large $M_{\max}$ model has a higher speed of sound in lower densities, resulting in supporting a larger maximum mass.

Chapter 5

Status and Outlook

5.1 Machine Learning for Astrophysics

While we used KDE to generate posterior distributions for our cooling project, another approach to faster MCMC convergence can be machine learning-based emulators. Traditional numerical techniques for simulating physical systems in the context of astrophysical simulations like computing the thermal evolution of a neutron star can frequently be computationally demanding. Regression models, especially those based on machine learning, have become effective instruments for speeding up physical computations. This is particularly helpful in situations like ours, where the higher dimensionality of the problem necessitates exceptional processing capacity to arrive at a stationary posterior distribution in a reasonable amount of time. A regression model, by learning from existing data, enables quick predictions that can significantly reduce computation time and achieve faster convergence for MCMC.

5.1.1 Gaussian Process Regression

Gaussian Process Regression (GPR) [102, 137] is a non-parametric approach that uses supervised learning to solve regression problems. A complex physics problem can be approximated by a Gaussian process that is characterized as a set of variables, any finite subset of which follows a joint Gaussian distribution. This is due to the central limit theorem that says that if you take enough samples from any distribution, the means will always be normally distributed. Taking this idea to higher dimensions, the probability density function of a D-dimensional multi-variate Gaussian distribution model can be defined as [134]

$$\mathcal{N}(x|\mu,\Sigma) = \frac{1}{(2\pi)^{D/2}|\Sigma|^{1/2}} \exp\left[-\frac{1}{2}(x-\mu)^T\Sigma^{-1}(x-\mu)\right] \tag{5.1}$$

Where x is the variable $(x_1, x_2, ..., x_D)$, μ is the mean and Σ is the $D \times D$ covariance matrix between all the variables. This covariance function captures the correlation between different points and is crucial for the Gaussian distribution function to be smooth when trying to match a function for regression. We can model a function using a multivariate Gaussian distribution, given a set of data X where the desired function f can be written as [134]

$$\begin{aligned} f(x)|X &\sim \mathcal{N}(\mu, \Sigma) \\ \text{or } f(x) &\sim \mathcal{GP}(\mu, \Sigma) \end{aligned} \tag{5.2}$$

When it comes to choosing a kernel, the Radial Basis Function (RBF) kernel is a good starting point as it is widely used for regression tasks for its smoothness and infinite differentiability.

$$\Sigma(x, x') = \sigma^2 \exp\left(-\frac{d(x_i, x_j)^2}{2l^2}\right) \tag{5.3}$$

Where d is the distance between two points x_i and x_j, l is the length scale that determines the correlation between two points and σ is the scale factor that indicates the span of the function. After optimizing these two hyperparameters for a specific problem, the final distribution often matches the desired function's behaviors. We use Scikit-learn's Gaussian process regression [111] for our problem. The implementation is based on Algorithm 2.1 of Ref. [102]. See Ref. [134] for an excellent summary of the Gaussian process.

Once we have enough data with a set of training inputs X and corresponding outputs $\mathbf{y}$, where $\mathbf{y} = f(X)$, the joint distribution of the observed outputs $\mathbf{y}$ and the function values at new inputs X_* can be expressed as:

$$\begin{bmatrix} \mathbf{y} \\ f(X_*) \end{bmatrix} \sim \mathcal{N}\left(\begin{bmatrix} \mu(X) \\ \mu(X_*) \end{bmatrix}, \begin{bmatrix} K(X, X) & K(X, X_*) \\ K(X_*, X) & K(X_*, X_*) \end{bmatrix}\right) \tag{5.4}$$

The data set is scaled to a uniform distribution to match the length scale of the RBF kernel and is split into two groups for training and testing purposes. The hyperparameters of the kernel are optimized during model fitting on the training data using the 'lbfgs' method with a metric of the mean squared error to cross-validate the accuracy of the model on the test data. GPR offers a unique advantage for uncertainty quantification in predictions, but the training process is slow and memory consumption of the process is quite high for a high dimensional problem such as ours. With 151 parameters one can accommodate only about 6000 points on a 32 GB RAM machine. This is not enough data for acceptable accuracy if we want inference to be included in this process. Multiple sub-models of GPR were tried to keep the overall size of the covariance matrices manageable. However, the best practice turned

out to be modeling the cooling process with only the EoS and superfluidity parameters. We will discuss this later.

5.1.2 Decision Tree Regression

Decision Tree Regression (DTR) is another non-parametric supervised learning method for regression tasks [17, 101, 48]. Given the variables ("features" in terms of the decision tree) $x = (x_1, x_2, ..., x_D)$ and the corresponding function we want to model $y = f(x)$, a decision tree is a tree-like model (see Fig. 5.1) in which the variables x_i from the root node and leaf nodes relate to the function $f(x)$. In this tree-like structure, internal nodes represent feature tests and branching identifies test results. The tree is created by iteratively partitioning the dataset based on feature values to reduce variation within each resulting subgroup. This procedure continues until a stopping point is reached, such as a maximum tree depth or a minimum amount of samples in a leaf node. Let Q_m represent the data at node m with

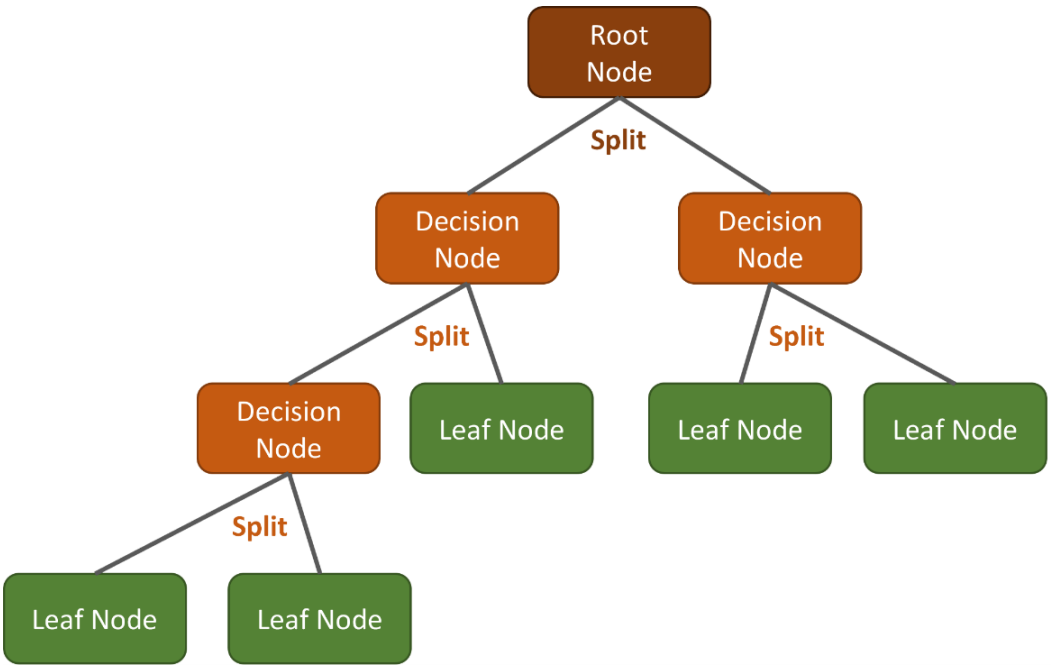


Figure 5.1: A Decision tree example [Image Credit: Quelle: FU Berlin, RESEDA, https://blogs.fu-berlin.de/reseda/random-forest].

n_m samples. Divide the data into $Q_m^{\text{left}}(\theta)$ and $Q_m^{\text{right}}(\theta)$ subsets for each candidate split $\theta = (j, t_m)$ that consists of a feature j and threshold t_m.

$$\begin{aligned} Q_m^{\text{left}}(\theta) &= \{(x, y) | x_j \leq t_m\} \\ Q_m^{\text{right}}(\theta) &= Q_m \backslash Q_m^{\text{left}}(\theta) \end{aligned} \tag{5.5}$$

For a regression problem, a common criterion to minimize the impurity for future splits is through an impurity function or loss function H, like mean squared error (MSE) or mean absolute error (MAE). Depending on the chosen criteria, either the mean μ_y or the median$(y)_m$ are set as the terminal node values [110].

$$H(Q_m)_{\text{MSE}} = \frac{1}{n_m} \sum_{y \epsilon Q_m} (y - \mu_y)^2$$
$$H(Q_m)_{\text{MAE}} = \frac{1}{n_m} \sum_{y \epsilon Q_m} |y - \text{median}(y)_m| \tag{5.6}$$

Then the loss function H is used to calculate the quality of a potential split of node m.

$$G(Q_m, \theta) = \frac{n_m^{left}}{n_m} H(Q_m^{left}(\theta)) + \frac{n_m^{right}}{n_m} H(Q_m^{right}(\theta)) \tag{5.7}$$

Determine which parameters minimize the impurity.

$$\theta^* = \text{argmin}_\theta G(Q_m, \theta) \tag{5.8}$$

For the subsets $Q_m^{\text{left}}(\theta^*)$ and $Q_m^{\text{right}}(\theta^*)$, recurse until either $n_m = 1$ or $n_m < \text{min}_{\text{samples}}$, the maximum permitted depth, is reached [110].

Following the construction of the decision tree, predictions are made by traversing the tree from the root to a leaf node in accordance with the input features. The average of the target values of the training samples that made it to that leaf node is the predicted value for a particular input.

Decision Tree Regression offers several advantages. The resulting model is easy to visualize and understand, allowing for a straightforward interpretation of how decisions are made. Decision trees can model complex, non-linear relationships without requiring transformation of the input features which is great for us as our input and output parameters often have different ranges that differ by many orders of magnitudes. We choose to use Scikit-learn's decision tree regression [110] which is an extension of the Classification and Regression Trees (CART) algorithm. After we have generated our data set, similarly to GPR, we break this data set into training and testing subsets. After initial training to see how the model performs, an exhaustive grid search is performed over the hyperparameter space of the regression model to find the best model. The best model is then trained on the full training set and is compared with the test subset to check for accuracy.

5.1.3 Neural Network Regression

Deep Neural Network Regression

Deep neural networks (DNN) are an emerging field of supervised learning methods that can be used for regression purposes [50, 14]. These networks are formed of nodes or neurons that are linked with one another specifying the inherent connection between them. Oftentimes, these networks are structured in layers (see Fig. 5.2). On one side, the very first layer takes the set of variables as input. This input layer consists of individual neutrons that represent each of the variables $\{x_i|x_1, x_2, ...x_D\}$ and the last layer on the other side of this network holds the output quantities or the function $f(x)$ that is to be modeled. Between the input and the output layer, there can be several hidden layers each made of some neurons. Each neuron in the hidden layer uses a weighted linear summation $w_1x_1 + w_2x_2 + ... + w_Dx_D$ and a non-linear activation function $g(.) : R \to R$ to convert the values from the previous layer. The values from the last hidden layer are sent to the output layer, which converts them into output values y.

For example, a typical DNN model with $\{x_i|x_1, x_2, ...x_D\}$ inputs and the output $f(x)$ with one hidden layer with m neurons fully connected, we have weights $W^{(1)} = \{W_1^{(1)}, W_2^{(1)}, ..., W_m^{(1)}\}$ and biases $b^{(1)} = \{b_1^{(1)}, b_2^{(1)}, ..., b_m^{(1)}\}$ for the hidden layer. Furthermore, the output layer also have its respective weights $W^{(2)}$ and biases $b^{(2)}$ matching the dimensionality of our output function $f(x)$. Then the calculation for this model goes as follows:

$$\begin{aligned} H &= xW^{(1)} + b^{(1)} \\ f(x) &= HW^{(2)} + b^{(2)} \end{aligned} \tag{5.9}$$

With an activation function σ in the hidden layer, the first equation transforms into

$$H = \sigma(xW^{(1)} + b^{(1)}) \tag{5.10}$$

The training of a DNN involves optimizing the weights of the connections between neurons to match the predicted and actual target values as well as possible. This process is iterative, and it has a few steps. Given an initial weight and activation function, the input data is processed by the network giving the output layer a prediction. Now a loss function (typically MSE) computes the error of the predicted outputs compared to the actual outputs. When we have N samples, and the predicted function is $f'(x)$, the loss is defined by

$$\mathcal{L}_{\text{MSE}} = \frac{1}{N}\sum_{i=1}^{N}(f(x)_i - f'(x)_i)^2 \tag{5.11}$$

The error is then transmitted back [80, 69, 107] through the network, adjusting the weights using optimization algorithms like Stochastic Gradient Descent (SGD) [16] or Adam [62]. This adjustment aims to reduce the loss in subsequent iterations. The forward propagation, loss calculation, and back-propagation steps are repeated until the model converges or the desired performance is achieved.

However, DNNs also have limitations. DNNs can have an overfitting problem, particularly when the model is complex. Careful use of dropout or decaying weights can help mitigate this issue. Training DNNs can be computationally intensive, especially for large networks or datasets, requiring careful tuning of hyperparameters. We use Scikit-learn's Multi-Layer Perceptron Regressor (MLPR) method 'MLPRegressor' and TensorFlow's DNN libraries that let us build our network suitable to our needs. The DNN model from Tensorflow is currently a `sequencial` model with three hidden layers with 'ReLU' and one output layer with linear activation functions and the 'adam' optimizer. A grid search is performed over both models' hyperparameter space to construct the best possible model. While they have large success rates and good accuracies, they have issues with physically improbable points and can predict them wrong at times. We hope to fix this in the near future. They also suffer the typical problems of overfitting that we are trying to mitigate using early stopping and adaptive learning rates, but the models require a large amount of data to have an acceptable accuracy.

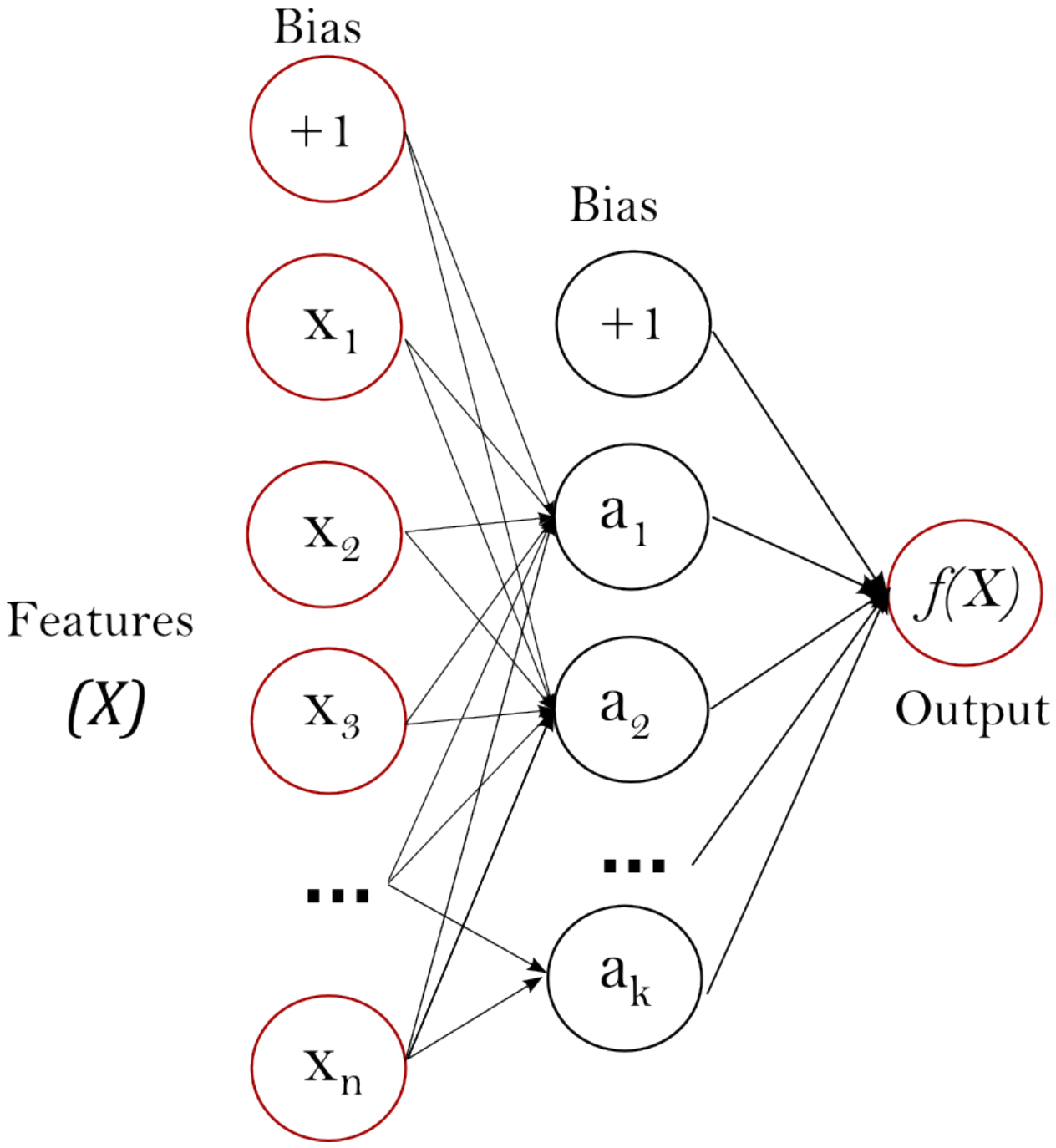


Figure 5.2: A DNN with one hidden layer example [Image Credit: https://scikit-learn.org/1.5/modules/neural_networks_supervised.html]

5.2 Preliminary results

The machine learning algorithms prove useful when predicting all successful points given we have enough training data. Fig. 5.4 shows the predicted likelihood vs the actual likelihood of the QLMXBs with only 2000 training data. The test is performed on a different data set as a test set to make sure we have no overlap. While this is reasonably accurate, something like predicting the likelihood of INS has larger uncertainties, as can be seen in Fig. 5.3. The radius prediction in Fig. 5.5 shows promise, but it's not accurate enough for the precision we are looking for. Further optimization through grid search and/or using a larger training set may alleviate this issue, so it can be used to replace physical calculations. This is something that we are currently working on.

The main problem we are currently trying to solve is when the proposed point in parameter space is physically inaccurate and must be rejected as a valid point. The rejections arise when we are testing our computed outputs with observed nuclear or multi-messenger astronomy data. Emulating these using a machine learning algorithm is proving quite difficult as using these in the regression models along with the successful points reduces the accuracy of predictions for the valid points. Using classification models to separate these points from the valid points is not good enough in its current state and for the scope of this project, we must find a compromise.

One way to solve this issue would be that we don't try to emulate these rejections and use simple checks that we already have in our codes. Instead, to make the process of traversing the parameter space faster, we just try to replace parts of the code that take up the longest amount of time to calculate. A good first starting point would be emulating the cooling calculations and the TOV solver. These take up about 90% of the time it takes to compute a single point.

Fig. 5.6 shows some selected cooling curves for 1, 1.4, and 2.0 $M_\odot$ stars for different EoS parameterizations. In fig. 5.7 we try to use DTR to emulate cooling on a test data set. The overall results are promising, but there are a few quirks we need to address. First, for lower-mass stars, the initial temperatures show a greater uncertainty compared to higher-mass stars. Second, the onset of direct Urca is sometimes incorrectly predicted for medium-mass stars where the emergence of the enhanced cooling processes is sensitive to the EoS parameters and can go either way. Again, through hyperparameter optimization and more data, we hope to overcome this problem.

There are advantages to this approach as all the physics checks are performed normally, so there is less chance of errors and for failed points to appear as valid points in the outputs. All the rest of the calculations like LIGO or nuclear properties are done normally, so they are always accurate. The only way a successful point achieved this way can be wrong is if the cooling calculations do not satisfy a physical check which is unlikely at this point.

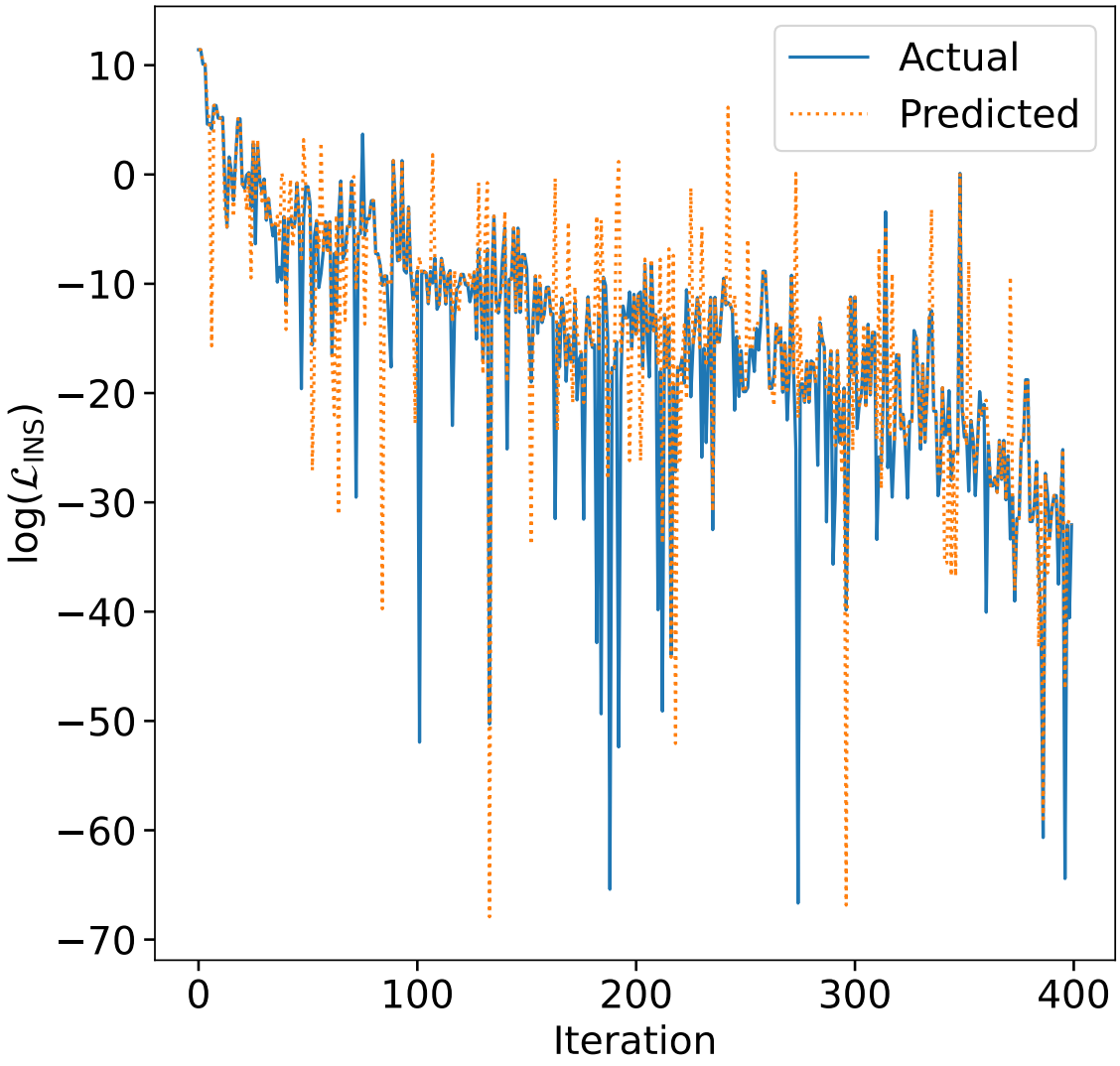


Figure 5.3: A Decision tree regression comparison of predicted vs actual likelihood of INS. While the predicted values follow the real function's overall trend, the individual inaccuracies are large and affect the overall likelihood function negatively. This is due to the large number of INS in our population whose individual likelihoods add up to the sum.

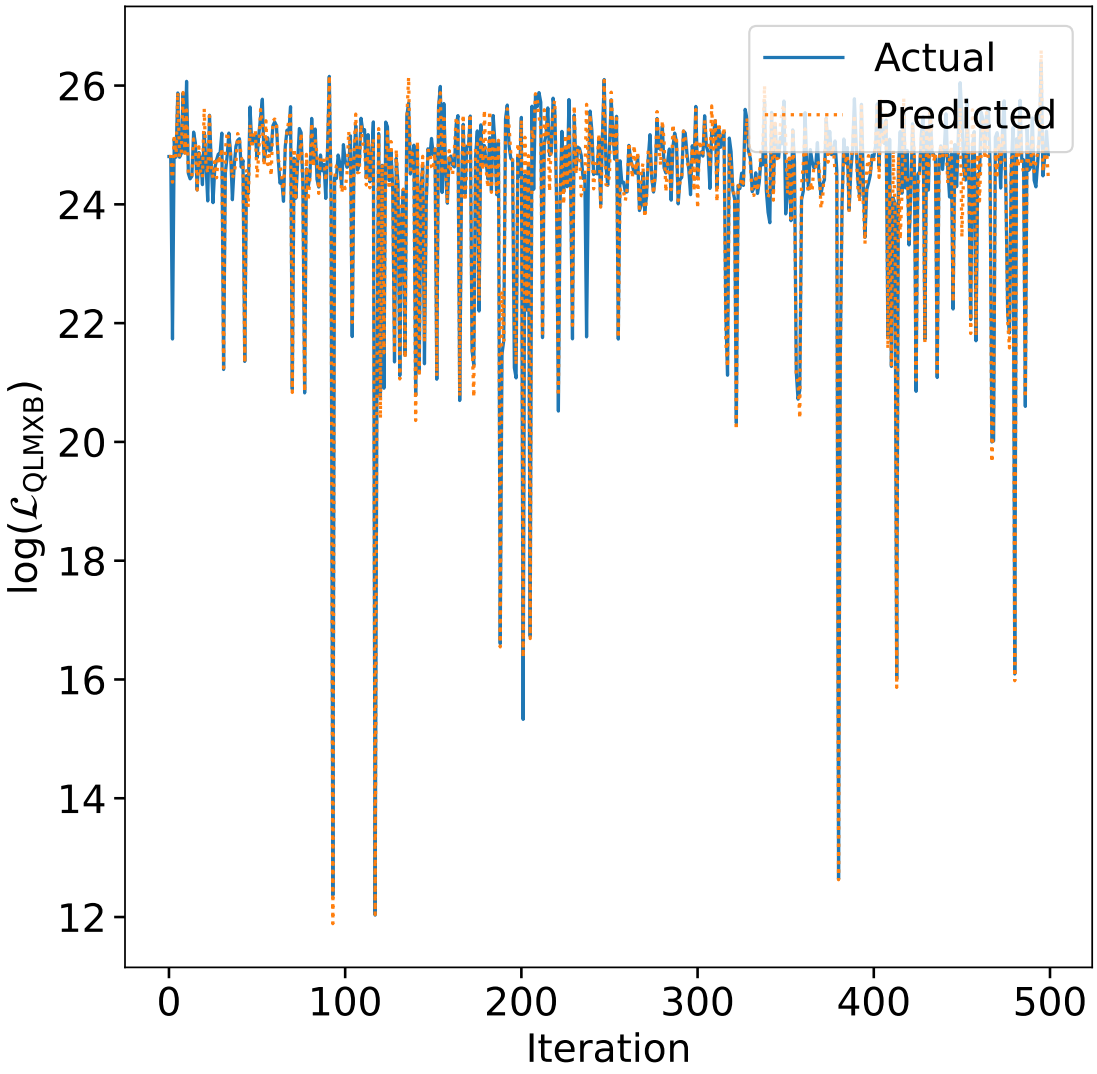


Figure 5.4: A Decision tree regression comparison of predicted likelihood of all low mass X-ray binaries to computed likelihood. The likelihood is computed from partially known mass-radius relations. This is a far more accurate description of the likelihood function due to the smaller population of QLMXBs.

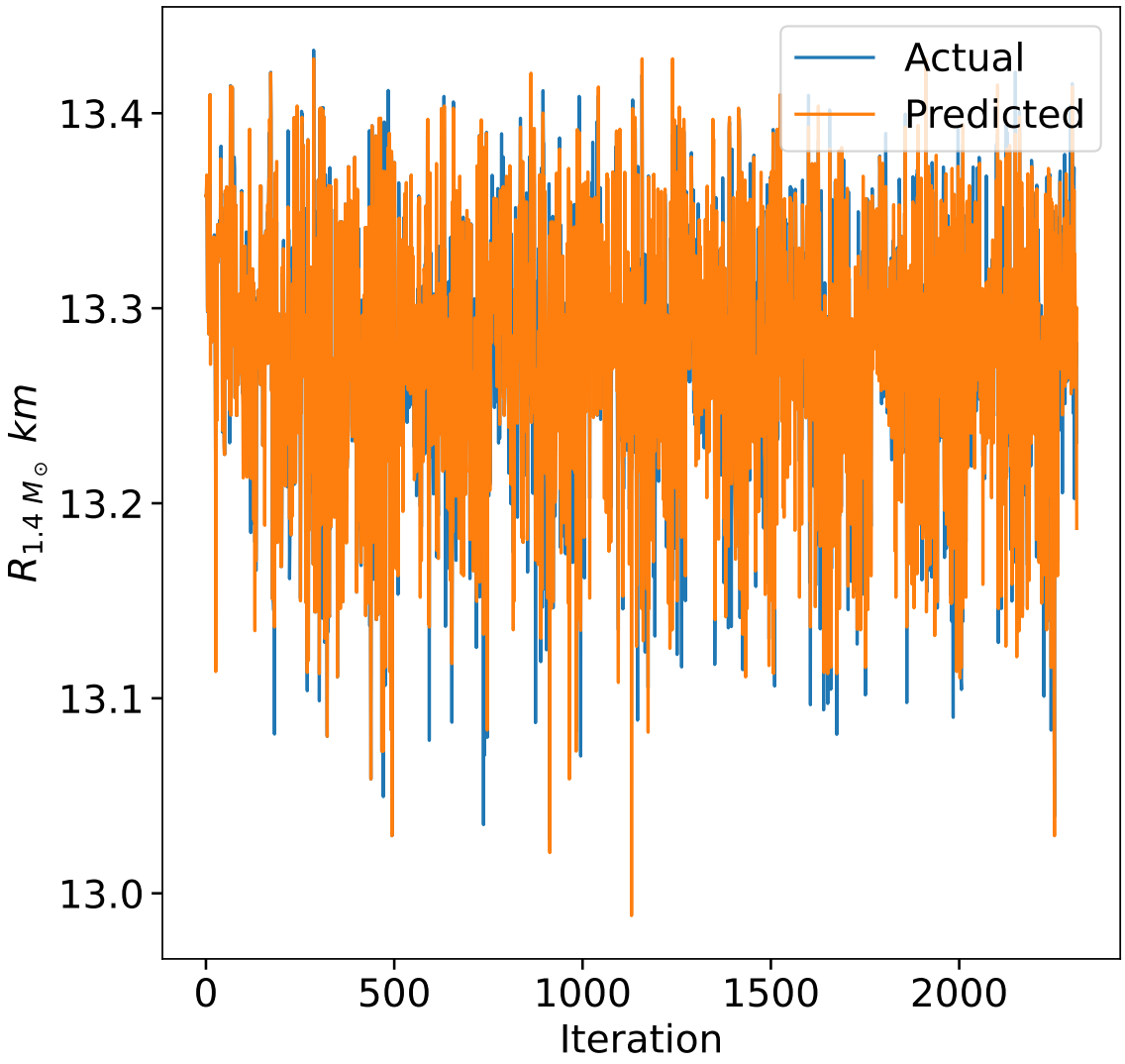


Figure 5.5: A Decision tree regression comparison of the radius of a 1.4 $M_\odot$ star predictions vs. the radius from TOV equations.

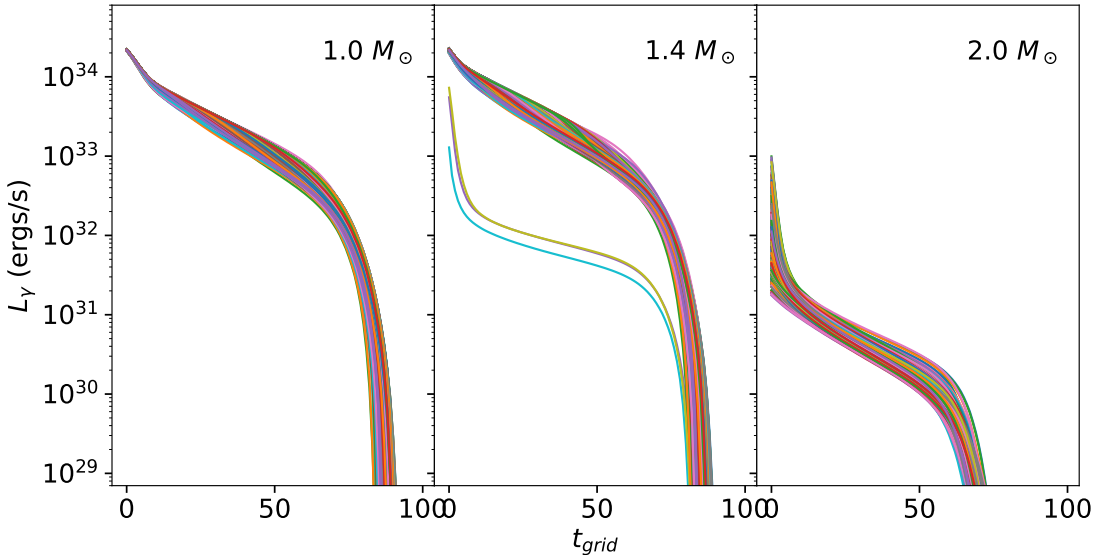


Figure 5.6: Computed cooling curves for 1, 1.4 and 2.0 $M_\odot$ stars. Note that 1.4 $M_\odot$ already has direct-Urca depending on the EoS making the cooling faster at times.

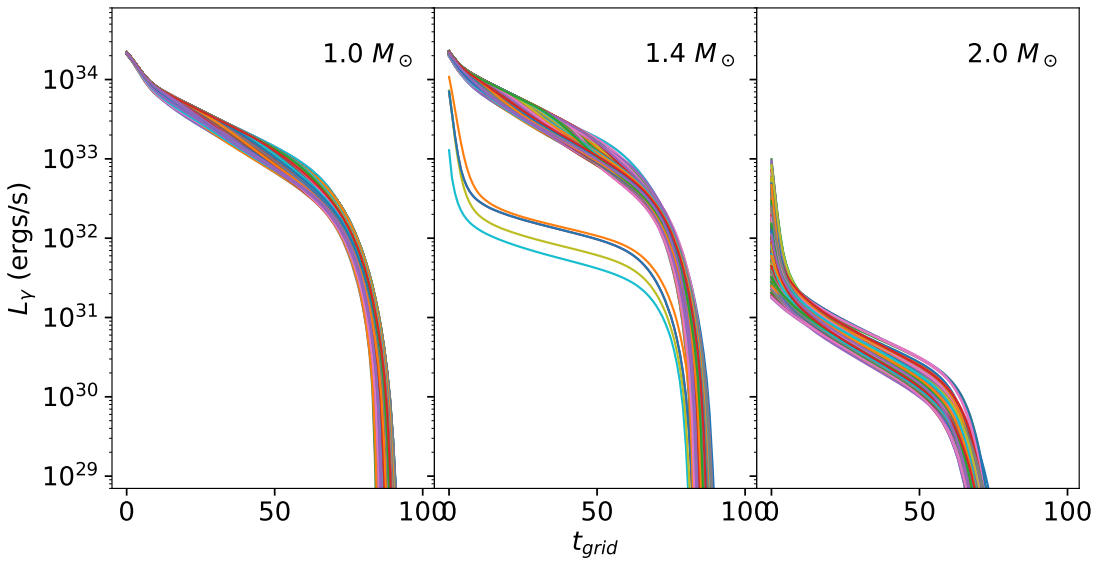


Figure 5.7: Predicted cooling curves 1, 1.4, and 2.0 $M_\odot$ stars. Stars with a mass on either end of the mass grid are quite accurate. Most of the inaccuracies lie in the cooling curves for 1.4 and 1.6 $M_\odot$ stars where the onset of direct Urca is sensitive to the EoS parameterizations.

Nevertheless, this can significantly (approximately 10 times) improve the computation times for each point, so the parameter space can be explored a lot faster. Once the MCMC has equilibrated, the posterior distribution can be sampled, and running the full code on these selected points can verify the validity before reaching conclusions.

5.3 Future work

When the nucleon chemical potentials increase sufficiently ($\rho_B = 2\rho_0$), to offset the mass disparities between nucleons and hyperons, hyperons can develop in neutron star cores. Ref. [9] discusses the presence and roles of hyperons in neutron stars in a detailed manner. The presence of hyperons softens the EoS compared to a pure nuclear-matter EoS [40]. The creation of hyperons as an additional species inside a NS relieves some Fermi pressure of the nucleons and acts like a "pressure control" mechanism in high-density matter. [9]. Hyperons also affect the maximum mass of an EoS by making it lower. Having hyperons inside the core affects the cooling process significantly as well by opening up the hyperonic direct-Urca channels. This might help explain the extremely low luminosity stars in our studies like SAX J1808 or 1H 1905.

In our current work, we have assumed that the stellar surface temperature is uniform. Non-uniform surfaces and incorporating evolving larger magnetic fields can be beneficial in future studies along with the inclusion of exotic particles like hyperons. Furthermore, for thermally evolving stars, mass-radius measurements and atmosphere data are missing in the current observations. Including future observations on these will significantly improve the current constraints.

Furthermore, The increase in the number of variables and the complexity of the future models demands a machine-learning approach to explore the posterior distribution in a reasonable amount of time and find EoS parameters that are well-suited to explain the current and emerging multi-messenger observations with chosen degrees of freedoms. Most importantly we want to create a framework that is scalable into the future, so we can add new observations with minimal efforts to update the results.

Chapter 6

Conclusions

In this work, we have proposed a framework for exploring dense matter physics from both laboratory data and astrophysical data through established theoretical models. X-ray observations from neutron stars and their cooling provide excellent information on the composition of the stellar core while gravitational wave observations provide better constraints on the mass-radius relation. Nuclear properties constrain the underlying physics that binds this all together. The cold and young neutron stars require direct Urca process in their core to reach their low luminosities. While the old and hotter neutron stars need some form of reheating or surface hot spots or larger magnetic fields to explain their higher luminosities. Observations of mass-radius information of the accreting neutron stars can provide crucial information on the EoS that will propel the state of this field by a lot. Similarly, spectral information of the envelope composition of more stars to constrain the $T_e - T_b$ relationship would constrain and simultaneously guide future analysis. This is a field of science that is intricately correlated to the advancements of technology. As we continue to get more astronomical data, these models of dense matter will only get better with time. As an example, GW170817 is just one sample of data from gravitational waves. With more of these events discovered, we will have a better understanding of the inner physics of neutron stars from improved mass-radius constraints. Similarly, improvements to computation technologies will enable these studies to be rendered much faster.

We have shown that as of now, minimal cooling is not enough to explain every astronomical observable we currently have, and we must explore enhanced cooling processes and the possibilities of exotic matter. We have established the importance of different EoS models and the importance of combining EoS models to explain neutron star properties better. This multipronged approach is beneficial to reach our final goal of finding the correct EoS. Furthermore, we have shown how emerging machine learning methods can be useful in the field of nuclear astrophysics in hopes that they will be used in future studies.

Bibliography

[1] (1965). On the theory of stars. In Ter Haar, D., editor, Collected Papers of L.D. Landau, page 60. Pergamon. 1

[2] Abbott, B. P. et al. (2017a). GW170817: Observation of Gravitational Waves from a Binary Neutron Star Inspiral. Phys. Rev. Lett., 119:161101. ix, xi, 1, 18, 20, 32, 33, 92

[3] Abbott, B. P. et al. (2017b). Properties of the binary neutron star merger GW170817. LIGO Document P1800061-v11. 32

[4] Adhikari, D. and others (PREX Collaboration) (2021). Accurate determination of the neutron skin thickness of ^{208}Pb through parity-violation in electron scattering. Phys. Rev. Lett., 126:172502. 20

[5] Al-Mamun, M., Steiner, A. W., Nättilä, J., Lange, J., O'Shaughnessy, R., Tews, I., Gandolfi, S., Heinke, C., and Han, S. (2021). Combining electromagnetic and gravitational-wave constraints on neutron-star masses and radii. Phys. Rev. Lett., 126:061101. ix, 32, 33, 34

[6] Ambartsumyan, V. A. and Saakyan, G. S. (1960). The Degenerate Superdense Gas of Elementary Particles. Sov. Astron., 4:187. 1

[7] Annala, E., Gorda, T., Hirvonen, J., Komoltsev, O., Kurkela, A., Nättilä, J., and Vuorinen, A. (2023). Strongly interacting matter exhibits deconfined behavior in massive neutron stars. Nat. Commun., 14. 47

[8] Baade, W. and Zwicky, F. (1934). Supernovae and cosmic rays. Phys. Rev., 45:138. 2, 5

[9] Balberg, S. and Lichtenstadt, I. (1999). Roles of Hyperons in Neutron Stars. Astrophys. J. Suppl. Ser., 121:515. 64

[10] Baym, G. and Campbell, D. K. (1978). Mesons in Nuclei. 6

[11] Beloin, S., Han, S., Steiner, A. W., and Odbadrakh, K. (2019). Simultaneous Fitting of Neutron Star Structure and Cooling Data. Phys. Rev. C, 100:055801. 20, 21

[12] Beloin, S., Han, S., Steiner, A. W., and Page, D. (2018). Constraining Superfluidity in Dense Matter from the Cooling of Isolated Neutron Stars. Phys. Rev. C, 97:015804. 18, 20, 24, 32, 37

[13] Beznogov, M. V. and Yakovlev, D. G. (2015). Statistical theory of thermal evolution of neutron stars. Mon. Not. R. Astron. Soc., 447:1598. viii, 18, 25, 26, 46

[14] Bishop, C. M. (2006). Pattern Recognition and Machine Learning. Springer. 56

[15] Blaschke, D., Grigorian, H., Voskresensky, D. N., and Weber, F. (2012). Cooling of the neutron star in Cassiopeia A. Phys. Rev. C, 85:022802. 47

[16] Bottou, L. (2010). Stochastic gradient descent. http://leonbottou.com/stochastic_gradient_descent. 57

[17] Breiman, L., Friedman, J. H., Olshen, R. A., and Stone, C. J. (1986). Classification and regression trees. In Wadsworth Statistics/Probability Series. Wadsworth and Brooks/Cole, Belmont, CA. 54

[18] Burgio, G. F. and Vidaña, I. (2020). The Equation of State of Nuclear Matter: From Finite Nuclei to Neutron Stars. Universe, 6. 4

[19] Campana, S., Stella, L., Gastaldello, F., Mereghetti, S., Colpi, M., Israel, G. L., Burderi, L., Di Salvo, T., and Robba, R. N. (2002). An XMM-Newton Study of the 401 Hz Accreting Pulsar SAX J1808.4-3658 in Quiescence. Astrophys. J., 575:L15. 25

[20] Chandrasekhar, S. (1935). The Highly Collapsed Configurations of a Stellar Mass. (Second Paper.). Mon. Not. R. Astron. Soc., 95:207. 6

[21] Chiu, H.-Y. and Salpeter, E. E. (1964). Surface x-ray emission from neutron stars. Phys. Rev. Lett., 12:413. 10

[22] Collins, J. C. and Perry, M. J. (1975). Superdense matter: Neutrons or asymptotically free quarks? Phys. Rev. Lett., 34:1353. 1

[23] Colpi, M., Geppert, U., Page, D., and Possenti, A. (2001). Charting the Temperature of the Hot Neutron Star in a Soft X-Ray Transient. Astrophys. J., 548:L175. 25

[24] Cooper, L. N. (1956). Bound electron pairs in a degenerate fermi gas. Phys. Rev., 104:1189. 12

[25] Cumming, A., Brown, E. F., Fattoyev, F. J., Horowitz, C. J., Page, D., and Reddy, S. (2017). Lower limit on the heat capacity of the neutron star core. Phys. Rev. C, 95:025806. 39

[26] Das, H. C., Wei, J.-B., Burgio, G. F., and Schulze, H.-J. (2024). Neutron star cooling and mass distributions. Phys. Rev. D, 109:123018. 46

[27] de Carvalho, S. M. (2013). Finite Temperature Effects in the White Dwarf Structure and Neutron Star Cooling in General Relativity. Thesis (PhD. (Physics)). 16

[28] de Carvalho, S. M., Negreiros, R., Orsaria, M., Contrera, G. A., Weber, F., and Spinella, W. (2015). Thermal evolution of hybrid stars within the framework of a nonlocal nambu–jona-lasinio model. Phys. Rev. C, 92:035810. 46

[29] Diener, J. P. W. (2008). Relativistic Mean-Field Theory Applied To The Study Of Neutron Star Properties. Thesis (MSc (Physics)). 8, 9

[30] Du, X., Steiner, A. W., and Holt, J. W. (2019). Hot and dense homogeneous nucleonic matter constrained by observations, experiment, and theory. Phys. Rev. C, 99:025803. 49, 101

[31] Du, X., Steiner, A. W., and Holt, J. W. (2022a). Eos for multi-messenger astrophysics (e4mma). https://github.com/np3m/e4mma/. 49, 50

[32] Du, X., Steiner, A. W., and Holt, J. W. (2022b). Hot and dense matter equation of state probability distributions for astrophysical simulations. Phys. Rev. C, 105:035803. 49, 50

[33] et. al., M. A. T. (2024). Muses documentation. https://musesframework.io/docs/. 48, 49, 50

[34] Fiorella Burgio, G. and Fantina, A. F. (2018). Nuclear Equation of State for Compact Stars and Supernovae, pages 255–335. Springer International Publishing. 6

[35] Fore, B. and Reddy, S. (2020). Pions in hot dense matter and their astrophysical implications. Phys. Rev. C, 101. 96, 97, 101

[36] Gamow, G. (1938). Structure of Atomic Nuclei and Nuclear Transformations, volume 141. Oxford: Clarendon Press. 1

[37] Garg, U. and Colò, G. (2018). The compression-mode giant resonances and nuclear incompressibility. Prog. Part. Nucl. Phys., 101:55–95. 21

[38] Gelman, A. and Rubin, D. B. (1992). Inference and monitoring convergence. Stat. Sci., 7:457. 85

[39] Glen, G. and Sutherland, P. (1980). On the cooling of neutron stars. Astrophys. J., 239:671. 11

[40] Glendenning, N. K. (1996). Compact Stars. Springer. 2, 64

[41] Glendenning, N. K. (2000). Compact Stars. Springer, 2 edition. 8, 9, 16, 21

[42] Gnedin, O. Y., Yakovlev, D. G., and Potekhin, A. Y. (2001). Thermal relaxation in young neutron stars. Mon. Not. R. Astron. Soc., 324:725. 16

[43] Goodman, J. and Weare, J. (2010). Ensemble samplers with affine invariance. Commun. Appl. Math. Comput. Sci., 5:65. 37, 84

[44] Gudmundsson, E. H., Pethick, C. J., and Epstein, R. I. (1983). Structure of neutron star envelopes. Astrophys. J., 272:286. 14, 81

[45] Haensel, P. and Zdunik, J. L. (1990). Non-equilibrium processes in the crust of an accreting neutron star. Astron. Astrophys., 227:431. 17

[46] Haensel, P. and Zdunik, J. L. (2003). Nuclear Composition and Heating in Accreting Neutron-Star Crusts. Astron. Astrophys., 404:L33. 2, 4, 17

[47] Han, S. and Steiner, A. W. (2017). Cooling of Neutron Stars in Soft X-ray Transients. Phys. Rev. C, 96:035802. viii, 17, 18, 20, 25, 26, 27, 35

[48] Hastie, T., Friedman, J., and Tibshirani, R. (2001). The Elements of Statistical Learning: Data Mining, Inference, and Prediction. Springer Series in Statistics. Springer New York, NY, 1 edition. 54

[49] Hastings, W. K. (1970). Monte carlo sampling methods using markov chains and their applications. Biometrika, 57:97. 84

[50] Haykin, S. (1999). Neural Networks: A Comprehensive Foundation. International edition. Prentice Hall. 56

[51] Heidelberger, P. and Welch, P. D. (1981). A spectral method for confidence interval generation and run length control in simulations. Commun. ACM, 24:233. 85

[52] Heinke, C. O., Altamirano, D., Cohn, H. N., Lugger, P. M., Budac, S. A., Servillat, M., Linares, M., Strohmayer, T. E., Markwardt, C. B., and Wijnands, R. (2010). Discovery of a Second Transient Low-Mass X-ray Binary in the Globular Cluster NGC 6440. Astrophys. J., 714:894. 25

[53] Heinke, C. O., Jonker, P. G., Wijnands, R., and Taam, R. E. (2007). Constraints on Thermal X-ray Radiation from SAX J1808.4-3658 and Implications for Neutron Star Neutrino Emission. Astrophys. J., 660:1424. viii, 12, 17, 18, 25, 26

[54] Hewish, A., Bell, S. J., Pilkington, J. D. H., Scott, P. F., and Collins, R. A. (1968). Observation of a Rapidly Pulsating Radio Source. Nature, 217:709. 1

[55] Ho, W. C. G., Elshamouty, K. G., Heinke, C. O., and Potekhin, A. Y. (2015). Tests of the nuclear equation of state and superfluid and superconducting gaps using the cassiopeia a neutron star. Phys. Rev. C, 91:015806. 47

[56] Horowitz, C. and Serot, B. D. (1981). Self-consistent hartree description of finite nuclei in a relativistic quantum field theory. Nuc. Phys. A, 368:503. 9

[57] Horowitz, C. J. and Piekarewicz, J. (2001). Neutron star structure and the neutron radius of ^{208}pb. Phys. Rev. Lett., 86:5647. 8

[58] Initiative, O. (2020). Openapi specification. Version 3.0.3. 95

[59] Initiative, O. (2021). OpenAPI Specification: Version 3.0.3. OpenAPI Initiative. Accessed: 2021-10-10. 95

[60] Instituto de Astronomía, Universidad Nacional Autónoma de México (2024). The Neutron star picture gallery. https://www.astroscu.unam.mx/neutrones/NS-Picture/NStar/NStar.html. Accessed: 2024-11-24. viii, 3

[61] Jonker, P. G., Steeghs, D., Chakrabarty, D., and Juett, A. M. (2007). The Cold Neutron Star in the Soft X-Ray Transient 1H 1905+000. Astrophys. J., 665:L147. 25

[62] Kingma, D. P. and Ba, J. (2017). Adam: A method for stochastic optimization. 57

[63] Lattimer, J. M., Pethick, C. J., Prakash, M., and Haensel, P. (1991). Direct urca process in neutron stars. Phys. Rev. Lett., 66:2701. 11

[64] Lattimer, J. M. and Prakash, M. (2001). Neutron Star Structure and the Equation of State. Astrophys. J., 550:426. 2, 6

[65] Lattimer, J. M. and Prakash, M. (2004). Neutron star equations of state. Astrophys. J., 613:L105–L108. 16

[66] Lattimer, J. M. and Prakash, M. (2007). Neutron star observations: Prognosis for equation of state constraints. Phys. Rep., 442:109. 2, 4, 9

[67] Lattimer, J. M. and Prakash, M. (2016). The equation of state of hot, dense matter and neutron stars. Phys. Rep., 621:127–164. 6

[68] Lattimer, J. M. and Steiner, A. W. (2014). Constraints on the symmetry energy using the mass-radius relation of neutron stars. Eur. Phys. J. A, 50:40. 21, 32

[69] LeCun, Y. A., Bottou, L., Orr, G. B., and Müller, K.-R. (2012). Efficient BackProp, page 9. Springer, Berlin, Heidelberg. 57

[70] Leinson, L. (2002). Direct urca processes on nucleons in cooling neutron stars. Nuc. Phys. A, 707. 18

[71] Mendes, M., Fattoyev, F. J., Cumming, A., and Gale, C. (2022). Fast Neutrino Cooling in the Accreting Neutron Star MXB 1659-29. Astrophys. J., 938:119. 39

[72] Menzes, K. M. and et al. (2007). Investigating non-perturbative treatments of quark matter in neutron stars. Phys. Rev. C, 76:055805. 6, 16

[73] Mereghetti, S., Pons, J. A., and Melatos, A. (2015). Magnetars: Properties, origin and evolution. Space Sci. Rev., 191:315. 46

[74] Metropolis, N., Rosenbluth, A., Rosenbluth, M., Teller, A., and Teller, E. (1953). Equations of state calculated by fast computing machines. J. Chem. Phys., 21:1087. 84

[75] Migdal, A. B. (1959). Superfluidity and Moment of Inertia of Nuclei. Nuc. Phys., 13:655. 12, 18

[76] Miller, M. C., Lamb, F. K., Dittmann, A. J., Bogdanov, S., Arzoumanian, Z., Gendreau, K. C., Guillot, S., Harding, A. K., Ho, W. C. G., Lattimer, J. M., Ludlam, R. M., Mahmoodifar, S., Morsink, S. M., Ray, P. S., Strohmayer, T. E., Wood, K. S., Enoto, T., Foster, R., Okajima, T., Prigozhin, G., and Soong, Y. (2019). PSR J0030+0451 Mass and Radius from NICER Data and Implications for the Properties of Neutron Star Matter. Astrophys. J. Lett., 887:L24. ix, 18, 20, 28, 31

[77] Miller, M. C., Lamb, F. K., Dittmann, A. J., Bogdanov, S., Arzoumanian, Z., Gendreau, K. C., Guillot, S., Ho, W. C. G., Lattimer, J. M., Loewenstein, M., Morsink, S. M., Ray, P. S., Wolff, M. T., Baker, C. L., Cazeau, T., Manthripragada, S., Markwardt, C. B., Okajima, T., Pollard, S., Cognard, I., Cromartie, H. T., Fonseca, E., Guillemot, L., Kerr, M., Parthasarathy, A., Pennucci, T. T., Ransom, S., and Stairs, I. (2021). The Radius of PSR J0740+6620 from NICER and XMM-Newton Data. Astrophys. J. Lett., 918:L28. ix, 18, 20, 28, 31

[78] Muller, H. and Serot, B. D. (1996). Relativistic Mean-Field Theory and the High-Density Nuclear Equation of State. Nuc. Phys. A, 606:508. 19, 36

[79] Negele, J. W. and Vautherin, D. (1973). Neutron star matter at sub-nuclear densities. Nuc. Phys. A, 207:298–320. 4

[80] Ng, A., Ngiam, J., Foo, C. Y., Mai, Y., and Suen, C. (2011). Backpropagation. http://cs229.stanford.edu/. 57

[81] Noda, T., Hashimoto, M.-a., Yasutake, N., Maruyama, T., Tatsumi, T., and Fujimoto, M. (2013). Cooling of compact stars with color superconducting phase in quark-hadron mixed phase. Astrophys. J., 765:1. 47

[82] Nomoto, K. and Tsuruta, S. (1986). Confronting x-ray observations of young supernova remnants with neutron star cooling models. Astrophys. J., 305:19. 11

[83] Nomoto, K. and Tsuruta, S. (1987a). Cooling of neutron stars: Effects of the finite time scale of thermal conduction. Astrophys. J., 312:711. 11

[84] Nomoto, K. and Tsuruta, S. (1987b). Neutron star cooling and the vela pulsar. 11

[85] Ofengeim, D. D., Kaminker, A. D., Klochkov, D., Suleimanov, V., and Yakovlev, D. G. (2015). Analysing neutron star in hess j1731-347 from thermal emission and cooling theory. Monthly Notices of the Royal Astronomical Society, 454(3):2668. 47

[86] Oppenheimer, J. R. and Volkoff, G. M. (1939). On massive neutron cores. Phys. Rev., 55:374. 1, 4

[87] Ozel, F. and Freire, P. (2016). The Equation of State of Neutron Stars: Constraints and Implications. Annu. Rev. Astron. Astrophys., 54:401. 6

[88] Page, D. (2016). NSCool: Neutron star cooling code. Astrophysics Source Code Library, record ascl:1609.009. 11, 12, 14, 81

[89] Page, D., Geppert, U., and Weber, F. (2006). The cooling of compact stars. Nuc. Phys. A, 777:497. Special Issue on Nuclear Astrophysics. vii, 15

[90] Page, D., Lattimer, J. M., Prakash, M., and Steiner, A. W. (2004). Minimal Cooling of Neutron Stars: A New Paradigm. Astrophys. J., 155:623. 10, 11, 14, 17, 18, 20, 21

[91] Page, D., Lattimer, J. M., Prakash, M., and Steiner, A. W. (2009). Neutrino Emission from Cooper Pairs and Minimal Cooling of Neutron Stars. Astrophys. J., 707:1131. 12, 20, 39

[92] Page, D., Lattimer, J. M., Prakash, M., and Steiner, A. W. (2014). Stellar Superfluids, chapter 21. 12, 14, 18

[93] Page, D., Prakash, M., Lattimer, J. M., and Steiner, A. W. (2011). Rapid Cooling of the Neutron Star in Cassiopeia A Triggered by Neutron Superfluidity in Dense Matter. Phys. Rev. Lett., 106:081101. 39

[94] Pedregosa, F., Varoquaux, G., Gramfort, A., Michel, V., Thirion, B., Grisel, O., Blondel, M., Prettenhofer, P., Weiss, R., Dubourg, V., Vanderplas, J., Passos, A., Cournapeau, D.,

Brucher, M., Perrot, M., and Duchesnay, E. (2011). Scikit-learn: Machine learning in Python. J. Mach. Learn. Res., 12:2825. 38

[95] Pethick, C. J., Ravenhall, D. G., and Lorenz, C. P. (1995). The Inner Boundary of a Neutron-Star Crust. Nuc. Phys. A, 584:675. 4

[96] Pons, J. A., Walter, F. M., Lattimer, J. M., Prakash, M., Neuhäuser, R., and An, P. (2002). Toward a Mass and Radius Determination of the Nearby Isolated Neutron Star RX J185635-3754. Astrophys. J., 564:981. 47

[97] Potekhin, A. Y. and Chabrier, G. (2018). Magnetic neutron star cooling and microphysics. Astron. Astrophys., 609:A74. 47

[98] Potekhin, A. Y., Pons, J. A., and Page, D. (2015). Neutron stars—cooling and transport. Space Sci. Rev., 191:239. 46

[99] Potekhin, A. Y., Zyuzin, D. A., Yakovlev, D. G., Beznogov, M. V., and Shibanov, Y. A. (2020a). Thermal luminosities of cooling neutron stars. Mon. Not. R. Astron. Soc., 496:5052. vii, 22, 93, 94

[100] Potekhin, A. Y., Zyuzin, D. A., Yakovlev, D. G., Beznogov, M. V., and Shibanov, Y. A. (2020b). Thermal Luminosities of Cooling Neutron Stars. Mon. Not. R. Astron. Soc., 496:5052. viii, 18, 20, 21, 22, 23

[101] Quinlan, J. R. (1986). Induction of decision trees. Machine Learning, 1:81. 54

[102] Rasmussen, C. E. and Williams, C. K. I. (2006). Gaussian processes for machine learning. In Adaptive Computation and Machine Learning. MIT Press, Cambridge, MA. 52, 53

[103] Reinhard, P. G., Roca-Maza, X., and Nazarewicz, W. (2021). Information Content of the Parity-Violating Asymmetry in ^{208}Pb. Phys. Rev. Lett., 127:232501. 18

[104] Riley, T. E., Watts, A. L., Bogdanov, S., Ray, P. S., Ludlam, R. M., Guillot, S., Arzoumanian, Z., Baker, C. L., Bilous, A. V., Chakrabarty, D., Gendreau, K. C., Harding, A. K., Ho, W. C. G., Lattimer, J. M., Morsink, S. M., and Strohmayer, T. E. (2019). A NICER View of PSR J0030+0451: Millisecond Pulsar Parameter Estimation. Astrophys. J. Lett., 887:L21. ix, 2, 6, 18, 20, 28, 31

[105] Riley, T. E., Watts, A. L., Ray, P. S., Bogdanov, S., Guillot, S., Morsink, S. M., Bilous, A. V., Arzoumanian, Z., Choudhury, D., Deneva, J. S., Gendreau, K. C., Harding, A. K., Ho, W. C. G., Lattimer, J. M., Loewenstein, M., Ludlam, R. M., Markwardt, C. B., Okajima, T., Prescod-Weinstein, C., Remillard, R. A., Wolff, M. T., Fonseca, E., Cromartie, H. T., Kerr, M., Pennucci, T. T., Parthasarathy, A., Ransom, S., Stairs, I., Guillemot, L., and Cognard, I. (2021). A NICER View of the Massive Pulsar PSR J0740+6620 Informed by Radio Timing and XMM-Newton Spectroscopy. Astrophys. J. Lett., 918:L27. ix, 18, 20, 28, 31

[106] Roberts, L. F., Shen, G., Cirigliano, V., Pons, J. A., Reddy, S., and Woosley, S. E. (2012). Protoneutron star cooling with convection: The effect of the symmetry energy. Phys. Rev. Lett., 108(6). 46

[107] Rumelhart, D. E., Hinton, G. E., and Williams, R. J. (1986). Learning representations by back-propagating errors. Nature, 323:533. 57

[108] Sarkar, T., Thapa, V. B., and Sinha, M. (2023). Fast neutron star cooling in light of the prex-2 experiment. Phys. Rev. C, 108:035801. 46

[109] Schutz, B. (2011). A First Course in General Relativity. Cambridge University Press. 5

[110] Scikit-learn (2021a). Decision Tree Regression. https://scikit-learn.org/1.5/auto_examples/tree/plot_tree_regression.html. 55

[111] Scikit-learn (2021b). Gaussian Processes. https://scikit-learn.org/stable/modules/gaussian_process.html. 53

[112] Sedrakian, A. (2016). Axion cooling of neutron stars. Phys. Rev. D, 93. 47

[113] Serot, B. D. and Walecka, J. D. (1986). Relativistic Nuclear Many-Body Problem. In Negele, J. W. and Vogt, E., editors, Adv. Nuc. Phys., volume 16, page 1. Plenum Press. 6, 7, 19

[114] Shapiro, S. L. and Teukolsky, S. A. (1983). Black holes, white dwarfs and neutron stars. The physics of compact objects. 10

[115] Sharma, S. (2017). Markov chain monte carlo methods for bayesian data analysis in astronomy. Annu. Rev. Astron. Astrophys., 55:213–259. 83, 84, 85

[116] Skyrme, T. (1958). The effective nuclear potential. Nuc. Phys., 9:615. 6

[117] Steiner, A. W. (2014). O2scl: Object-oriented scientific computing library. Astrophysics Source Code Library, record ascl:1408.019. 5, 8, 9, 86

[118] Steiner, A. W. and Du, X. (2023). Eos tables crust-dft. 49

[119] Steiner, A. W., Heinke, C. O., Bogdanov, S., Li, C., Ho, W. C. G., Bahramian, A., and Han, S. (2018a). Constraining the Mass and Radius of Neutron Stars in Globular Clusters. Mon. Not. R. Astron. Soc., 476:421. 20, 34

[120] Steiner, A. W., Heinke, C. O., Bogdanov, S., Li, C. K., Ho, W. C. G., Bahramian, A., and Han, S. (2018b). Constraining the mass and radius of neutron stars in globular clusters. Mon. Not. R. Astron. Soc., 476:421. ix, 28, 29, 30, 31

[121] Steiner, A. W., Hempel, M., and Fischer, T. (2013). Core-collapse Supernova Equations of State Based on Neutron Star Observations. Astrophys. J., 774:17. 6

[122] Steiner, A. W., Lattimer, J. M., and Brown, E. F. (2016). Neutron star radii, universal relations, and the role of prior distributions. Eur. Phys. J. A, 52. 34

[123] Steiner, A. W., Prakash, M., Lattimer, J. M., and Ellis, P. J. (2005a). Isospin asymmetry in nuclei and neutron stars. Phys. Rep., 411:325. 8, 9, 19, 20

[124] Steiner, A. W., Prakash, M., Lattimer, J. M., and Ellis, P. J. (2005b). Isospin asymmetry in nuclei and neutron stars. Phys. Rep., 411:325. 19, 36

[125] Team, S. (2020). Swagger openapi specification. https://swagger.io/specification/. 95

[126] Thakur, V. and Dhiman, S. K. (2019). A study of charge radii and neutron skin thickness near nuclear drip lines. Nuc. Phys. A, 992:121623. 10

[127] Thorne, K. S. (1977). The relativistic equations of stellar structure and evolution. Astrophys. J., 212:825. 10

[128] Thorsett, S. E., Arzoumanian, Z., Camilo, F., and Lyne, A. G. (1999). The Triple Pulsar System PSR B1620-26 in M4. Astrophys. J., 523:763. 2

[129] Tolman, R. C. (1939). Static Solutions of Einstein's Field Equations for Spheres of Fluid. Phys. Rev., 55:364. 4

[130] Tsuruta, S. and Cameron, A. G. W. (1966). Cooling and detectability of neutron stars. Can. J. Phys., 44:1863. 10

[131] Tsuruta, S., Sadino, J., Kobelski, A., Teter, M. A., Liebmann, A. C., Takatsuka, T., Nomoto, K., and Umeda, H. (2009). Thermal evolution of hyperon-mixed neutron stars. Astrophys. J., 691(1):621. 46

[132] Vehtari, A., Gelman, A., and Gabry, J. (2016). Practical Bayesian model evaluation using leave-one-out cross-validation and WAIC. Stat. Comput., 27:1413. 85

[133] Walter, F., Pons, J., Burwitz, V., Lattimer, J., Lloyd, D., Wolk, S., Prakash, M., and Neuhäuser, R. (2004). Properties of the isolated neutron star RX J185635-3754. Adv. Space Res., 33:513. High-Energy Studies of Supernova Remnants and Neutron Stars. 47

[134] Wang, J. (2024). An Intuitive Tutorial to Gaussian Process Regression. 52, 53

[135] Weber, F., Negreiros, R., Rosenfield, P., and Stejner, M. (2007). Pulsars as Astrophysical Laboratories for Nuclear and Particle Physics. Prog. Part. Nucl. Phys., 59:94. 2, 8, 9

[136] Wheeler, J. A. (1957). On the nature of quantum geometrodynamics. Ann. Phys. (N. Y.), 2:604. 6

[137] Williams, C. K. I. and Rasmussen, C. E. (1996). Gaussian Processes for Regression. Adv. Neural Inf. Process. Syst., 8:514. 52

[138] Yagi, K. and Yunes, N. (2013). I-Love-Q Relations in Neutron Stars and their Applications to Astrophysics, Gravitational Waves and Fundamental Physics. Phys. Rev. D, 88:023009. 32

[139] Yagi, K. and Yunes, N. (2016). Approximate Universal Relations among Tidal Parameters for Neutron Star Binaries. Class. Quantum Gravity, 34:015006. 32

[140] Yakovlev, D. (2001). Neutrino emission from neutron stars. Phys. Rep., 354:1. 4

[141] Yakovlev, D. G., Levenfish, K. P., and Haensel, P. (2003). Thermal State of Transiently Accreting Neutron Stars. Astron. Astrophys., 407:265. 17, 25

[142] Yakovlev, D. G., Levenfish, K. P., Potekhin, A. Y., Gnedin, O. Y., and Chabrier, G. (2004). Thermal states of coldest and hottest neutron stars in soft X-ray transients. Astron. Astrophys., 417:169. 2, 4, 17

[143] Yakovlev, D. G., Levenfish, K. P., and Shibanov, Y. A. (1999). Cooling of neutron stars and superfluidity in their cores. Physics-Uspekhi, 42:737–778. 1

[144] Yakovlev, D. G. and Pethick, C. J. (2004). Neutron Star Cooling. Annu. Rev. Astron. Astrophys., 42:169. viii, 4, 10, 11, 13, 14, 17, 19, 46

Appendices

A The Neutron star cooling code

Our neutron star cooling code is based on "NSCool" [88], rewritten to allow for an arbitrary equation of state (EOS) and more general form for the superfluid or superconducting gaps. The effective surface temperature is determined by a parameter that describes the envelope composition using the parameterization from Ref. [44]. We presume a uniform surface temperature for all stars, except for the implicit temperature variation which was used to compute the probability distributions in mass-radius space for the NICER sources. We ignore any impact from the magnetic field, thus for the INSs, we choose only those objects that have an inferred magnetic field less than 10^{14} G. NSCool [88] solves the thermal evolution equations of a spherically symmetric star considering a fully general relativistic case with the necessary cooling and heating mechanisms giving the user the temperature or luminosity profiles of the star along with all the necessary physics outputs. It requires the initial boundary conditions, the physics inputs, and an initial temperature profile of the star. The star is discretized in the radial dimension from 0 to a value $i_{\max}$. While luminosities are defined at the even indices, temperatures are defined at the odd indices in an alternating manner. The energy balance and heat transport equations from earlier can be summarized as:

$$\begin{aligned} \frac{d\mathcal{T}}{dt} &= F\left(Q_h, Q_\nu, C_v; \frac{d\mathcal{L}}{dr}\right) \\ \mathcal{L} &= G\left(\kappa, \frac{d\mathcal{T}}{dr}\right) \end{aligned} \tag{1}$$

where

$$\mathcal{T} \equiv e^{\phi} T \text{ and } \mathcal{L} \equiv e^{2\phi} L \tag{2}$$

These partial differential equations are then provided with the boundary conditions: 1. At the center of the star there is no point source or sink of energy: $\mathcal{L}(r=0,t) \equiv 0$. 2. At the surface of the star: $\mathcal{L} = 4\pi R_\infty^2 \sigma_{SB} T_{e,\infty}^4$, where T_e is the surface temperature.

Then the star is evolved step by step in time through iterations and new $\mathcal{T}$ and $\mathcal{L}$ at time $t + dt$ are computed from old $\mathcal{T}^{\text{old}}$ and $\mathcal{L}^{\text{old}}$ at time t assuming we know them beforehand (this is why an initial temperature profile is needed).

$$\begin{aligned} \frac{d\mathcal{T}}{dt} = F\left(\mathcal{T}, \frac{d\mathcal{L}}{dr}\right) &\rightarrow \mathcal{T} = \mathcal{T}^{\text{old}} + dt.F\left(\mathcal{T}, \frac{d\mathcal{L}}{dr}\right) \\ \mathcal{L} = G\left(\mathcal{T}, \frac{d\mathcal{T}}{dr}\right) &\rightarrow \mathcal{L} = G\left(\mathcal{T}, \frac{d\mathcal{T}}{dr}\right) \end{aligned} \tag{3}$$

Doing this for every time step then gives us the thermal and luminosity evolution profile of the star that we are looking for

$$(\mathcal{T}_i^{(0)}, \mathcal{L}_i^{(0)}) \rightarrow (\mathcal{T}_i^{(1)}, \mathcal{L}_i^{(1)}) \rightarrow (\mathcal{T}_i^{(2)}, \mathcal{L}_i^{(2)}) \rightarrow ... \tag{4}$$

Where i is the appropriate even and odd indices for luminosities and temperatures. A guess value of $(\mathcal{T}_i, \mathcal{L}_i)$ is taken in to see if it solves the equations for $(\mathcal{T}_{i+1}, \mathcal{L}_{i+1})$, and they are corrected consecutively until the equations are solved. This gives us the k^{th} to $(k+1)^{th}$ iteration, with corrections $\delta\mathcal{T}_i^{(k)}$ and $\delta\mathcal{L}_i^{(k)}$:

$$\begin{aligned} \mathcal{T}_i^{(k)} \rightarrow \mathcal{T}_i^{(k+1)} &= \mathcal{T}_i^{(k)} + \delta\mathcal{T}_i^{(k)} [i = 1, 3, 5, ...] \\ \mathcal{L}_i^{(k)} \rightarrow \mathcal{L}_i^{(k+1)} &= \mathcal{L}_i^{(k)} + \delta\mathcal{L}_i^{(k)} [i = 0, 2, 4, ...] \end{aligned} \tag{5}$$

This entire brute force method is accelerated by using the Henyey scheme. Solving these equations at all of these indices is treated as a multidimensional problem that is solved using the Newton-Rhapson method. The energy balance and the heat transport equations can be rewritten as:

$$\begin{aligned} \phi(\mathcal{T}) &= \mathcal{T} - \mathcal{T}^{\text{old}} - dt.F\left(\mathcal{T}, \frac{d\mathcal{L}}{dr}\right) = 0 \\ \phi(\mathcal{L}) &= \mathcal{L} - G\left(\mathcal{T}, \frac{d\mathcal{T}}{dr}\right) = 0 \end{aligned} \tag{6}$$

and the iteration goes like:

$$X^{k+1} = X^k - [D\phi(X^k)]^{-1} \times \phi(X^k) \tag{7}$$

for luminosity and temperature alternatively (X stands for luminosity or temperature depending on the index k and D is the derivative matrix of ϕ).

These iterations are continued until the corrections are small enough:

$$\begin{aligned} \text{Max}_{i=1,3,5,...}\left(\frac{\delta\mathcal{T}_i^{(k)}}{\mathcal{T}_i^{(k)}}\right) &< \epsilon_T \text{ and} \\ \text{Max}_{i=0,2,4,...}\left(\frac{\delta\mathcal{L}_i^{(k)}}{\mathcal{L}_i^{(k)}}\right) &< \epsilon_L \end{aligned} \tag{8}$$

The code is really fast and an accuracy of the order of 10^{-10} can be achieved within 5 iterations.

B Markov Chain Monte Carlo

Markov Chain Monte Carlo (MCMC) is a class of algorithms used for sampling from a probability distribution. The concept behind MCMC is to construct a chain whose stationary distribution is the desired target distribution and over time, the chain will converge to that target distribution. After reaching the target distribution, we may calculate expectation values and integrals for various variables by taking samples from the chain. Similar to Monte Carlo integration. The term "Monte Carlo" in MCMC refers to the use of random numbers in the Markov process, which is similar to Monte Carlo integration techniques. In traditional Monte Carlo integration, random samples are statistically independent, but in MCMC, they are correlated [115].

Markov defined Markov chains in the early 20th century, which introduced stochastic processes in which future states rely only on the current state. Formally, the Markov property may be stated as follows. If X_t is the system's state at time t:

$$P(X_{t+1} = x | X_t = y, X_{t-1} = z, \ldots) = P(X_{t+1} = x | X_t = y) \tag{9}$$

This is often referred to as the transition probability from X_t to X_{t+1}:

$$K(x, y) = P(X_{t+1} = y | X_t = x) \tag{10}$$

A Markov chain has a stationary distribution τ if

$$\tau(y) = \int dx \; \tau(x) \; K(x, y) \tag{11}$$

Provided that the transition between x and y is possible through a finite number of steps, the chain is irreducible and has a unique stationary distribution. Then the law of large numbers implies that for a function $f(x)$, the expectation value over τ can be approximated by its average.

$$E_\tau[f(x)] = \int f(x)\tau(x)dx = \lim_{n\to\infty} \frac{1}{n} \sum_{i=1}^{n} f(x_i) \tag{12}$$

This lets us sample the posterior distribution for Monte Carlo estimates of our desired information. When the chain has equilibrated, the condition of detailed balance says the chain would be reversible [115] i.e.

$$P(X_n, X_{n+1}) = P(X_{n+1}, X_n) \tag{13}$$

B.1 Metropolis-Hastings Algorithm

Initially coined by Metropolis [74] and subsequently improved by Hastings [49], the Metropolis-Hastings algorithm consists of two steps to construct a transitional probability $K(x, y)$. Considering that we want to sample the distribution of a function $f(x)$, a proposal distribution is specified $q(y|x)$. Then points are drawn from $q(y|x)$ with an acceptance ratio $\alpha = \min\left[1, \frac{f(y)q(x|y)}{f(x)q(y|x)}\right]$. Hence, the transition probability is $K(x, y) = q(y|x)\alpha(x, y)$. A uniform random variable U is sampled at every step. If $U < \alpha$ then the step is accepted and $X_{t+1} = y$. Otherwise, the step is rejected, and the system stays in its current state $X_{t+1} = X_t$. There are multiple ways to select this proposal distribution $q(y|x)$ and depending on the method, the transition kernel takes a different shape [115]. For our problem, once we had an initial parameterization that led to a successful likelihood calculation, the Metropolis-Hastings algorithm was used to generate enough sample points that can be used as the initial configuration of affine-invariant sampling.

B.2 Affine Invariant Sampling

The affine invariant sampling algorithm, developed by Goodman and Weare [43] provides an elegant solution to the shortcomings of traditional MH algorithms such as poor mixing or convergence issues. In affine invariant sampling, multiple chains are run in parallel and can interact with others to change their proposal densities to satisfy the Markovian property simultaneously. These chains are called walkers. Consider we have an ensemble of walkers $W = (w_1, w_2, ..., w_L)$. Then the Markov chain that has the target distribution $\prod(W) = \pi(w_1)\pi(w_2)...\pi(w_L)$ must satisfy the detailed balance principle $p(y_i|w_i, w_{-i}) = p(w_i|y_i, w_{-i})$ [115]. Which means w_i is updated depending on the rest of the walkers $w_{-i} = \{w_1, ..., w_{i-1}, w_{i+1}, ...w_L\}$. Considering that walker w_i is in state x_i, the transition to a new state y can be written as:

$$y = x_i + (r - 1)(x_i - x_j) = x_j + r(x_i - x_j) \tag{14}$$

Where r is a scalar with density $g(r)$. To satisfy the detailed balance, we must have $g(1/r) = rg(r)$. The acceptance ratio is then $\min[1, r^{n-1}\frac{\pi(Y)}{\pi(X_i)}]$ [115]. Move and stretch are examples of affine transformations and by calculating the appropriate Jacobian, the target distribution can be effectively sampled.

An affine invariant sampling needs at least three times walkers compared to the number of variables. Since we have 151 parameters, 512 walkers were chosen for our affine invariant sampling run to generate enough samples for the KDE estimator. It is possible to probe the

posterior probability distribution from the results of the affine invariant runs. However, that is only possible/advisable once the MCMC has reached its stationary distribution.

B.3 Ensuring Convergence

Only after an MCMC has converged to its target distribution can we sample the distribution to make inferences over our choice of attributes. Several methods have been proposed in the literature. Autocorrelation calculations can give us an estimated length scale to isolate independent samples from the chains. Low effective sample size indicates that the samples are highly correlated and may not provide reliable estimates of the target distribution [132]. The Gelman-Rubin statistic compares the variance between multiple chains to the variance within each chain [38]. Heidelberger and Welch [51] proposed testing for the equality of the mean and variance over different segments of the chain. If the segments are statistically different, the chain has not yet converged.

Gelman-Rubin Diagnostic

The Gelman-Rubin diagnostic [38], provides a quantitative measure of whether multiple chains from an affine-invariant MCMC simulation have converged to the target distribution or not by comparing the variance of the samples between multiple parallel MCMC chains to the variance within each chain. As all chains are converging to the same stationary distribution, the intra-chain variance should be similar to the interchain variance [115].

For example, if we have m independent MCMC chains, each with n iterations. For each chain i, for a variable θ the mean $\bar{\theta}_i$ and the overall mean $\bar{\theta}$ is

$$\bar{\theta}_i = \frac{1}{n}\sum_{j=1}^{n}\theta_{ij}, \quad \bar{\theta} = \frac{1}{m}\sum_{i=1}^{m}\bar{\theta}_i \tag{15}$$

The intra-chain variance B and interchain variance W are

$$\begin{aligned} B &= \frac{n}{m-1}\sum_{i=1}^{m}(\bar{\theta}_i - \bar{\theta})^2 \\ W &= \frac{1}{m}\sum_{i=1}^{m}\frac{1}{n-1}\sum_{j=1}^{n}(\theta_{ij} - \bar{\theta}_i)^2 \end{aligned} \tag{16}$$

The total variance $\hat{\sigma}^2$ of θ can be written as

$$\hat{\sigma}^2 = W\frac{n-1}{n} + B \tag{17}$$

The pooled variance is then

$$V = \hat{\sigma}^2 + \frac{B}{m} = W\frac{n-1}{n} + B\frac{m+1}{m} \tag{18}$$

The Gelman-Rubin diagnostic is defined by $\hat{R} = \sqrt{V/W}$

If $\hat{R} \simeq 1$, this indicates that the chains have converged to the same distribution. A common threshold for convergence is $\hat{R} < 1.1$, which suggests that the chains are well-mixed and that further sampling is unlikely to yield substantially different results. While there are multiple packages exist (like pyMC), we chose to write our own GR test code for analyzing our data. Both Python and C++ versions are available at Ref. [117] (this is a work in progress).

C Extra plots

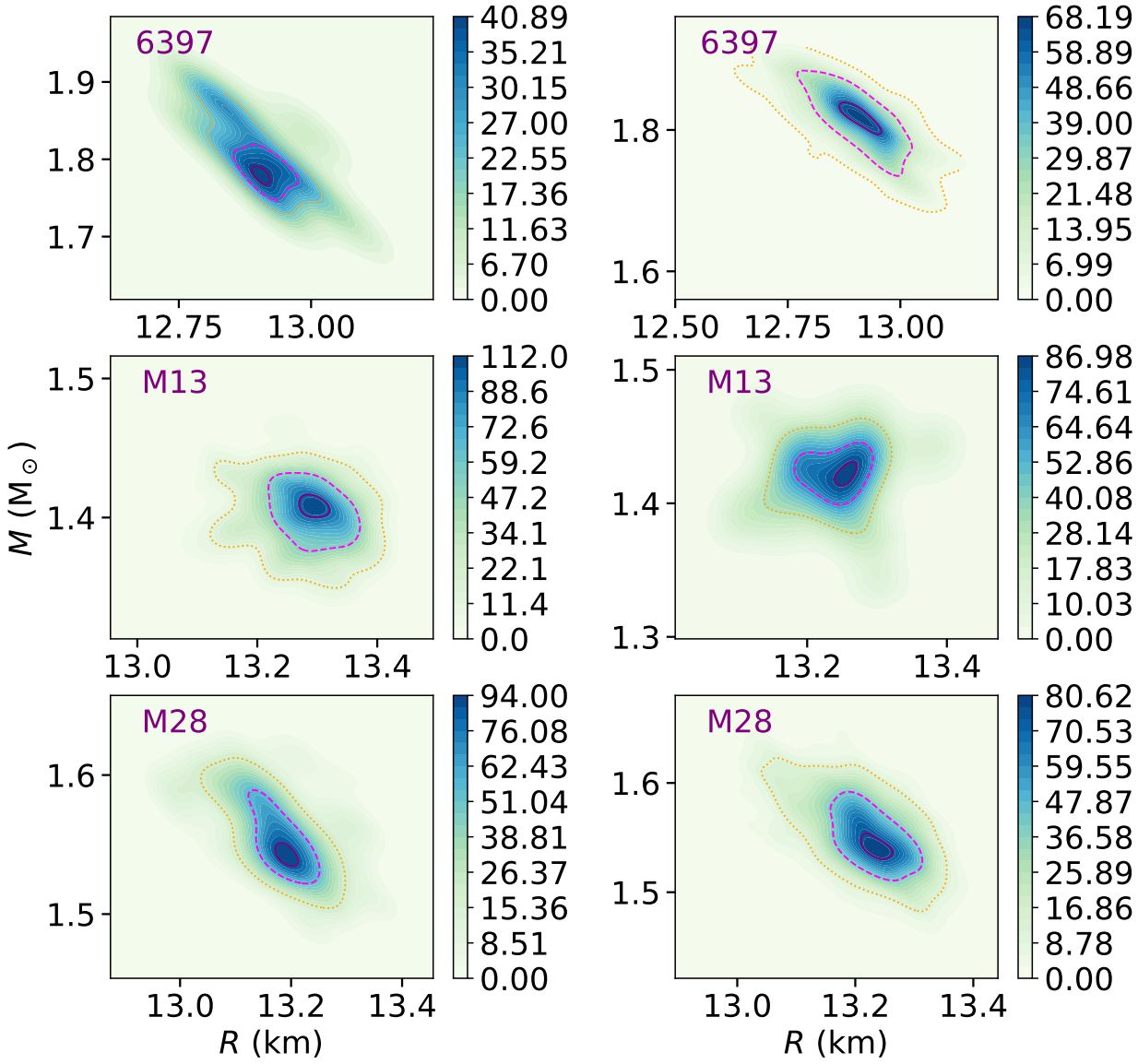


Figure 1: Posterior mass-radius distribution of QLMXBs from the globular clusters 6397, M13, and M28. Left panels denote hydrogen atmospheres and the right panels are helium atmospheres.

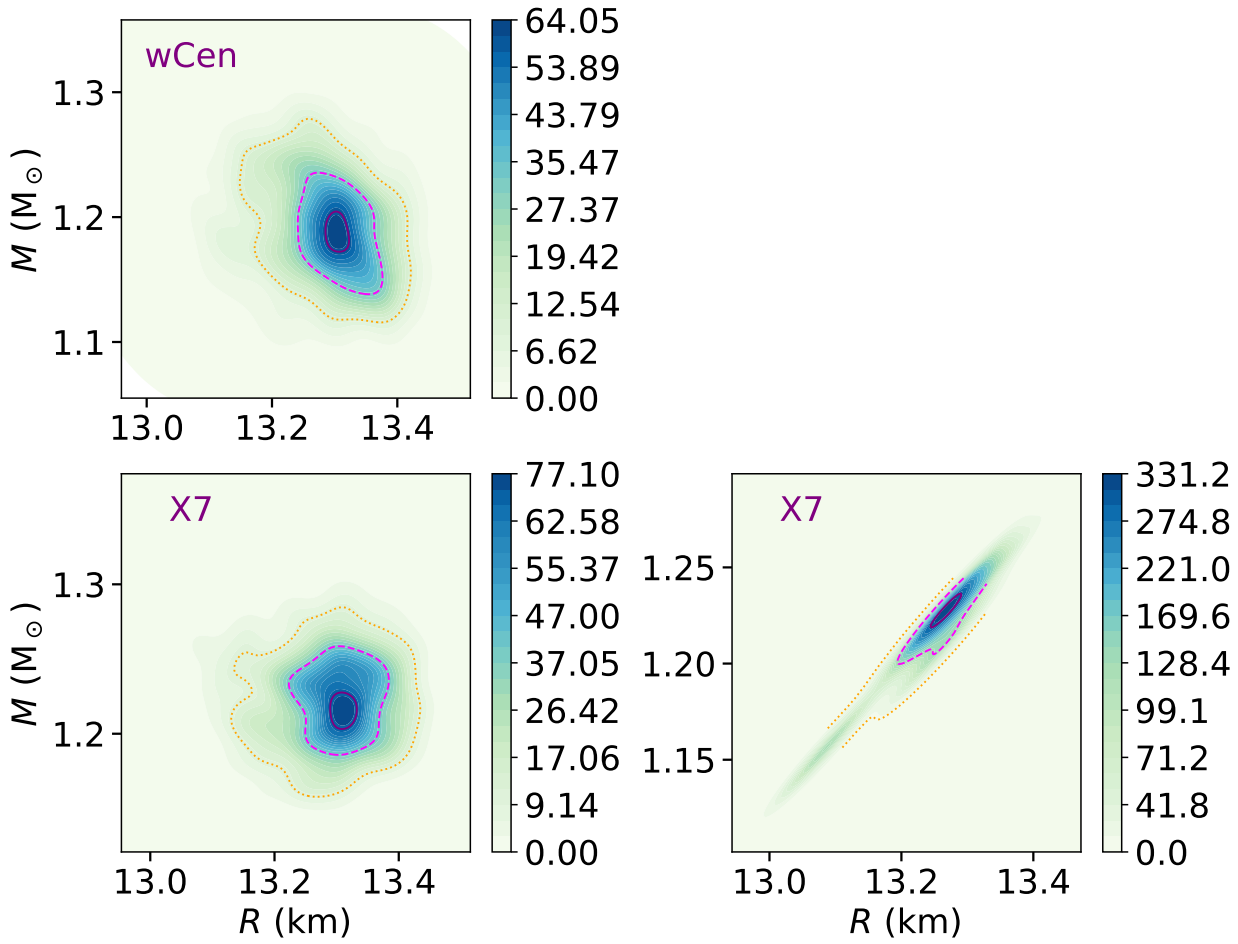


Figure 2: Posterior mass-radius distribution of QLMXBs from the globular clusters ω Cen and X7. Left panels denote hydrogen atmospheres and the right panel is helium atmospheres.

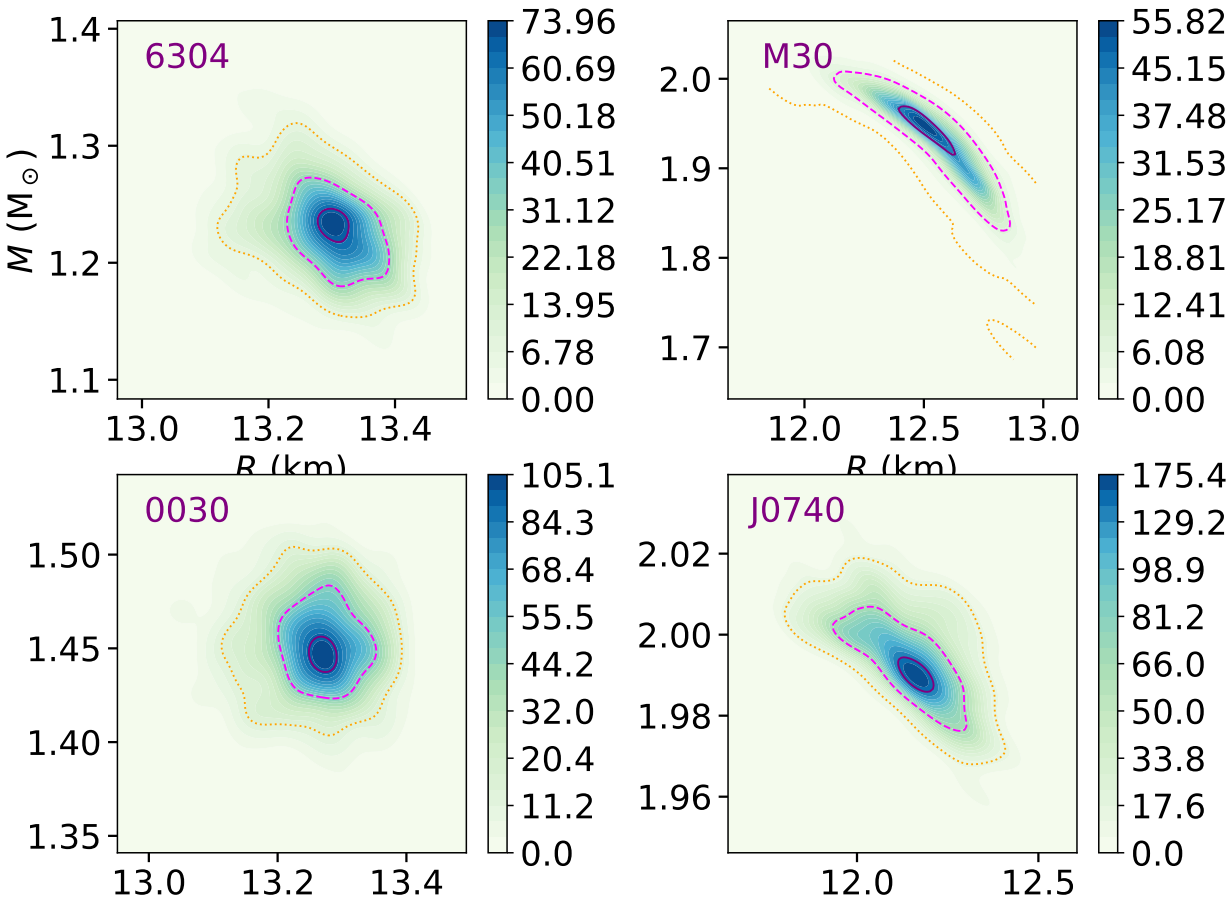


Figure 3: Posterior mass-radius distribution of QLMXBs from globular clusters 6304 and M30 and the NICER stars J0030 and J0740. Here only M30 has a helium atmosphere. J0030 and J0740 have hydrogen atmospheres and 6304 prefers a hydrogen atmosphere from our analysis.

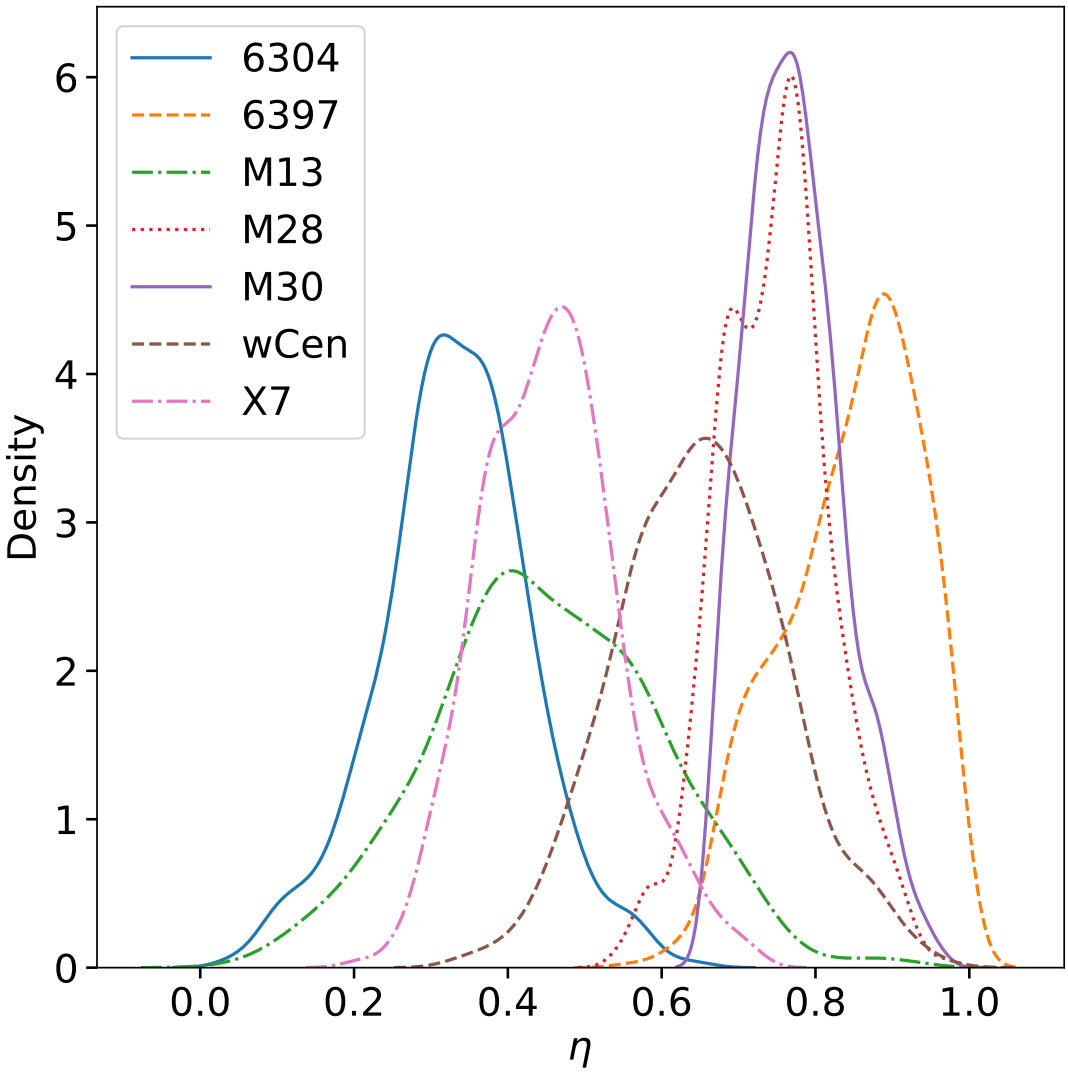


Figure 4: Posterior distribution of QLMXB atmospheres. 6304 (blue line) predominantly prefers a hydrogen atmosphere whereas M30 (purple line) and 6397 (orange dashed line) prefer helium atmospheres.

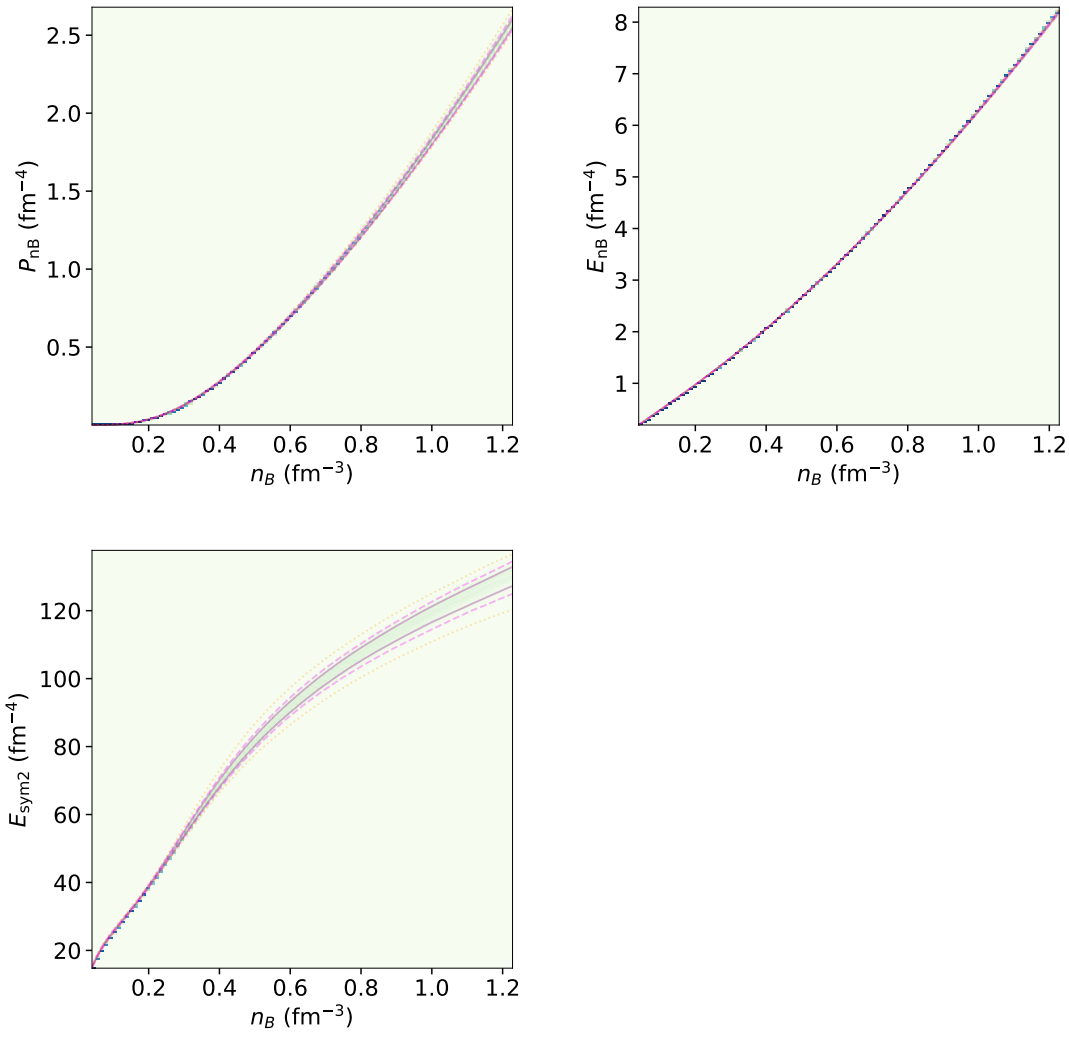


Figure 5: Posterior nuclear properties against baryon densities.

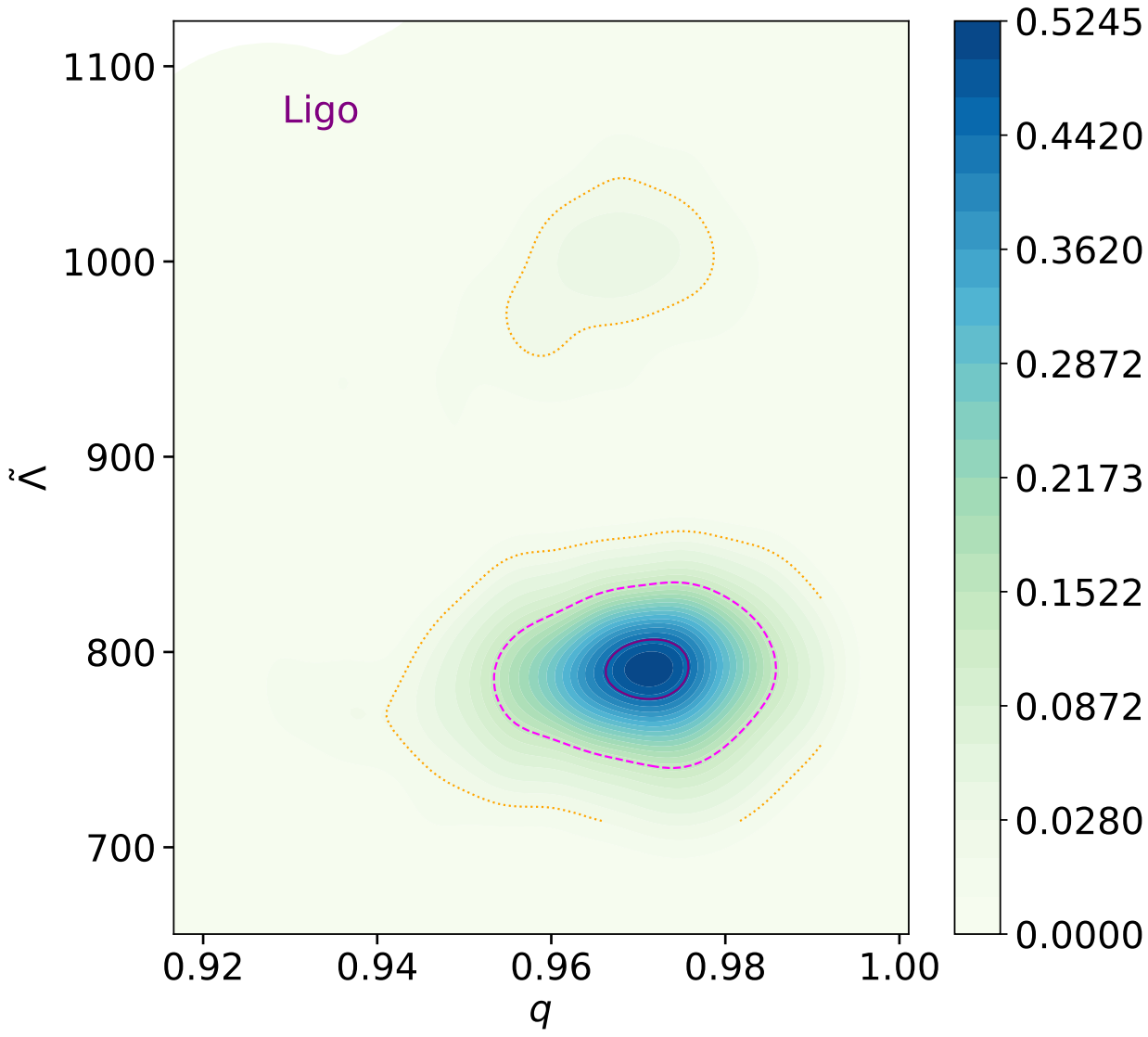


Figure 6: LIGO posterior for mass ratio q and tidal-deformability $\tilde{\Lambda}$. Here the stellar masses values of the NS-NS binary are quite close to one another. The tidal deformability $\tilde{\Lambda}$ has a value near 800 which is the low-spin prior from Ref. [2].

D INS Observations

Table 1: INS observations from Ref. [99].

Name	t_c	$t_{k,\text{low}}$	t_k	$t_{k,\text{high}}$	L_{low}	L	L_{high}	kT_{low}	kT	kT_{high}	η
J0822	2.54×10^{8}	3.70×10^{3}	4.45×10^{3}	5.20×10^{3}	3.9	5	6.1	240	0.0	475	true
J085201	0.0	2.40×10^{3}	0.0	5.10×10^{3}	1	2	3	80	90	100	true
J104608	0.0	1.10×10^{4}	0.0	3.00×10^{4}	0.077	0.0	0.62	40	0.0	70	true
1E1207	3.01×10^{8}	2.33×10^{3}	7.00×10^{3}	2.10×10^{4}	1.15	1.31	1.8	90	0.0	250	true
J141256	2.85×10^{5}	0.0	0.0	0.0	1.5	0.0	9	101	0.0	110	true
J160103	0.0	600	800	1.00×10^{3}	4.4	4.9	6.3	125	133	147	true
J1713	0.0	1.61×10^{3}	0.0	1.61×10^{3}	1.7	2.0	2.3	128	136	145	true
J172054	0.0	600	0.0	700	10.8	11.8	12.8	156	162	168	true
J173203	0.0	2.00×10^{3}	0.0	6.00×10^{3}	7.8	10.8	14.5	150	156	162	true
J181852	0.0	2.70×10^{3}	3.40×10^{3}	6.00×10^{3}	4.2	8.4	15.2	110	130	150	true
J185238	1.92×10^{8}	3.20×10^{3}	6.00×10^{3}	7.80×10^{3}	8.4	10.4	12.8	132	133	134	true
J232327	0.0	319.5	326.2	338.7	5.6	0.0	9.3	120	0.0	128	true
J0205	5.37×10^{3}	819.4	819.5	819.6	0.08	0.19	0.34	43	49	54	true
J0357	5.41×10^{5}	2.00×10^{5}	0.0	1.30×10^{6}	0.004	0.015	0.04	30	36	45	true
J0538	6.20×10^{5}	4.00×10^{4}	0.0	1.10×10^{5}	0.63	1.09	1.36	86	91	96	true
J0554	5.17×10^{4}	0.0	0.0	0.0	0.14	0.19	0.27	45	48	51	true
J061705	0.0	2.50×10^{4}	3.00×10^{4}	3.50×10^{4}	0.25	0.26	0.27	58	58.4	59	true
J0633-06	5.92×10^{4}	0.0	0.0	0.0	0.08	0.2	0.8	49	53	57	true
J0633-17	3.43×10^{5}	0.0	0.0	0.0	0.049	0.088	0.109	40	42	44	false
B0656	1.11×10^{5}	3.10×10^{5}	3.50×10^{5}	4.00×10^{5}	0.32	0.35	0.38	67	68	69	false
B0833	1.13×10^{4}	1.70×10^{4}	0.0	2.70×10^{4}	0.412	0.424	0.436	56	57	60	true
B0950	1.75×10^{7}	6.00×10^{5}	1.90×10^{6}	7.60×10^{6}	2.00×10^{-5}	8.00×10^{-5}	2.30×10^{-4}	5	7	11	false

Table 2: INS observations from Ref. [99] continued.

Name	t_c	$t_{k,\mathrm{low}}$	t_k	$t_{k,\mathrm{high}}$	L_{low}	L	L_{high}	kT_{low}	kT	kT_{high}	η
B1055	5.35×10^5	0.0	0.0	0.0	0.03	0.1	0.2	65	68	71	false
J1357	7.31×10^3	0.0	0.0	0.0	0.29	0.36	0.43	60	64	68	true
B1706	1.75×10^4	0.0	0.0	0.0	0.06	0.71	0.87	40	70	230	true
J1740	1.14×10^5	0.0	0.0	0.0	0.09	0.11	0.16	70	0.0	140	false
J1741	3.86×10^5	0.0	0.0	0.0	0.21	0.31	0.45	58	60	62	false
B1822	2.33×10^5	0.0	0.0	0.0	0.017	0.026	0.038	79	83	87	false
B1823	2.14×10^4	0.0	0.0	0.0	0.36	0.45	0.54	92	97	101	true
B1951	1.07×10^5	4.60×10^4	6.40×10^4	8.20×10^4	0.07	0.18	0.48	110	130	150	false
J1957	8.40×10^5	0.0	0.0	0.0	0.005	0.0	0.014	20.1	0.0	25.3	true
J2021	1.72×10^4	0.0	0.0	0.0	0.35	0.5	0.73	58	63	69	true
B2334	4.06×10^4	7700	0.0	2.00×10^4	0.012	0.047	0.082	30	46	52	true
J0726	1.86×10^5	0.0	0.0	0.0	0.3	0.4	0.84	63	74	80	false
J1119	1.60×10^3	4.20×10^3	0.0	7.10×10^3	1.1	1.9	3.8	80	0.0	210	true
B1509	1.56×10^3	0.0	0.0	0.0	7	9	11	133	142	149	true
J1718	3.32×10^4	0.0	0.0	0.0	0.2	0.4	0.9	57	0.0	200	true
J0720	1.90×10^6	7.00×10^5	8.50×10^5	1.00×10^6	0.11	0.19	0.32	91.4	92.4	93.3	false
J1308	1.46×10^6	3.00×10^5	5.50×10^5	8.00×10^5	0.26	0.33	0.38	50	0.0	90	true
J1605	0.0	3.80×10^5	4.40×10^5	5.10×10^5	0.007	0.0	0.5	35	0.0	120	true
J1856	3.72×10^6	3.40×10^5	4.20×10^5	5.00×10^5	0.05	0.0	0.08	36	0.0	63	true
J0007	1.39×10^4	9.10×10^3	9.20×10^3	9.30×10^3	0.0	0.0	0.03	0.0	0.0	200	true
B1727	8.05×10^4	4.00×10^4	5.00×10^4	6.00×10^4	0.0	0.0	0.035	0.0	0.0	33	true
B0114	2.75×10^5	0.0	0.0	0.0	0.0041	0.0044	0.0047	150	170	190	false

E OpenAPI 3.0 For Crust-DFT

OpenAPI 3.0 (formerly known as Swagger [125]) is a specification for creating APIs that is useful to outline the structure and functionality of their software in a standardized format [58, 59]. MUSES CE uses OpenAPI to interact with the individual modules. This requires an OpenAPI specifications file and a manifest file that gets registered in CE specifying paths and requirements of the input and output files.

Each API endpoint is defined as a path, with operations such as GET, POST, PUT, and DELETE specified for each path. This provides a clear mapping of HTTP methods to their corresponding functions. All the inputs and outputs of a software module can be specified with their corresponding schemas holding the necessary information for the end user. Depending on these schemas, the inputs and outputs can be validated for safer and more comprehensive operation of the module.

Adding OpenAPI specifications for Crust-DFT included creating an input and output schema and putting the possible CLI functions necessary for MUSES where different EoS models can be accessed and analyzed at zero temperature. Furthermore, the functionality to generate tables based on a user configuration was added with MPI capabilities on CE. A table and an input configuration file are usually mounted to the running container of Crust-DFT and the output EoS file and a status update file are generated and stored for later use.

F Pion Integration in Crust-DFT

Crust-DFT contains homogeneous nuclear matter with nucleons. In order to add hadronic resonances, the first task is to compute pion interactions. This boils down to solving the equation

$$f(n_n, n_p, \{n_i\}, \{n_r\}, n_e, n_\mu, n_\pi, T) = m_n n_n + m_p n_p + f_{np} + \sum_i f_i + \sum_r f_r + f_{\rm Coul} + f_e + f_\mu + f_\gamma + f_\pi \quad . \tag{19}$$

Here our variable is the proton number density $n_p = n_e + n_\pi$. To solve the pion interaction and get pion properties at a given n_B, Y_e, and T, we will start with guessing the proton number density n_p first. Given Y_e, we know n_e and we can compute the fermionic EOS to get electron chemical potential μ_e and hence the pion chemical potential μ_π as $\mu_e = \mu_\pi$.

Using the pion-nucleon phase shifts, pion self-energy is calculated. Now we can calculate single-particle energy for pions and check for condensation. If condensation happens, we set new μ_π as the minimum of the single-particle energy for pions. Given the μ_π, we can compute the number density of pions n_π. Next, we go ahead and compute the pion properties namely the pressure P_π, the energy density ϵ_π, and entropy s_π of pions.

Bose-Einstein distribution function is used for pions instead of Boltzmann distribution [35]

$$f_\pi(E_\pi) = \frac{1}{\exp[-\beta(E_\pi - \mu_\pi)] - 1} \tag{20}$$

The pion dispersion relation gives the energy of pions

$$E_\pi(p) = \sqrt{p^2 + m_\pi^2} + \Sigma_\pi(p) \tag{21}$$

as a function of the pion momentum p, pion mass m_π and the pion self-energy $\Sigma_\pi(p)$ which is

$$\Sigma_\pi(p) = \int \frac{d^3k}{(2\pi)^3} \sum_{N=n,p} f_N[E_N(k)] V_{N\pi}^{ps}(p_{\rm cm}) \tag{22}$$

Where $f_N[E_N(k)]$ is the distribution function of the nucleons and $V_{N\pi}^{ps}(p_{\rm cm})$ is the pseudo-potential.

$$\begin{aligned} f_N[E_N(k)] &= \frac{1}{\exp -\beta[E_N(k) - \mu_N] + 1} \\ V_{N\pi}^{ps}(p_{\rm cm}) &= -\alpha \sum_{I,l,\nu} (2l+1) \frac{2\pi \delta_{l,\nu}^I}{\bar{m} p_{\rm cm}} \end{aligned} \tag{23}$$

where, p_{cm} is the center of mass momentum between pions and nucleons (pion momentum p and nucleon momentum k with θ being the angle between them).

$$p_{\text{cm}} = \bar{m}\sqrt{\frac{p^2}{m_\pi^2} + \frac{k^2}{m_N^2} - \frac{2pk}{m_\pi m_N}\cos\theta} \tag{24}$$

$$\bar{m} = m_\pi m_N/(m_N + m_\pi) \tag{25}$$

is the reduced mass. The pion-nucleon interaction is directly proportional to the phase shifts, $\delta^I_{l,\nu}$, which depend on the isospin I, the angular momentum l and nucleon spin-projections ν [35].

Only $l = 0, 1$, i.e, the s-wave and p-wave contributions are dominant at the energies of interest. For neutrons, since $n - \pi$ scattering only involves the isospin $I = 3/2$ state, only the pion-nucleon phase shift in the isospin $I = 3/2$ channel denoted by $\delta^{3/2}_{l,\nu}$ contributes to the second-virial coefficient for the $n - \pi$ system $b_2^{n\pi}$.

$$\delta^{3/2}_{\text{sum},n} = \alpha_0^{3/2} 2\delta_0^{3/2} + \alpha_1^{3/2} 3(\delta_{1+}^{3/2} + \delta_{1-}^{3/2}) \tag{26}$$

for proton-pion scattering, it has two reaction channels.

$$\pi p \to \pi p \text{ and } \pi p \to \pi^0 n \tag{27}$$

which implies these reactions do not have definite isospin.

$$\begin{aligned}\delta_{\text{sum},p} = 2(&\alpha_0^{3/2}\delta_0^{3/2} + \alpha_0^{1/2}\delta_0^{1/2}) \\ &+3[\alpha_1^{3/2}(\delta_{1+}^{3/2} + \delta_{1-}^{3/2}) \\ &+\alpha_1^{1/2}(\delta_{1+}^{1/2} + \delta_{1-}^{1/2})]\end{aligned} \tag{28}$$

so the total phase shifts for a given center of mass momentum for neutrons and protons

$$\delta^{3/2}_{\text{sum},n} = \sum_{I,l,\nu} \alpha_l^I (2l+1)\delta^I_{l,\nu} \tag{29}$$

$$\delta_{\text{sum},p} = \sum_{I,l,\nu} \alpha_l^I (2l+1)\delta^I_{l,\nu} \tag{30}$$

To compute the energy of the pions, we need to compute the self-energy first. This is a two-dimensional integral. One integral is over p_{cm} and the other is over k. p_{cm} is dependent on p, k and θ. So for a particular p and k we have to integrate over θ to find the pseudo-potential contribution to the integration. Then we integrate over k. Since $-1 \leq \cos\theta \leq 1$ the limits of p_{cm} becomes $\bar{m}(\frac{p}{m_\pi} - \frac{k}{m_N})$ to $\bar{m}(\frac{p}{m_\pi} + \frac{k}{m_N})$.

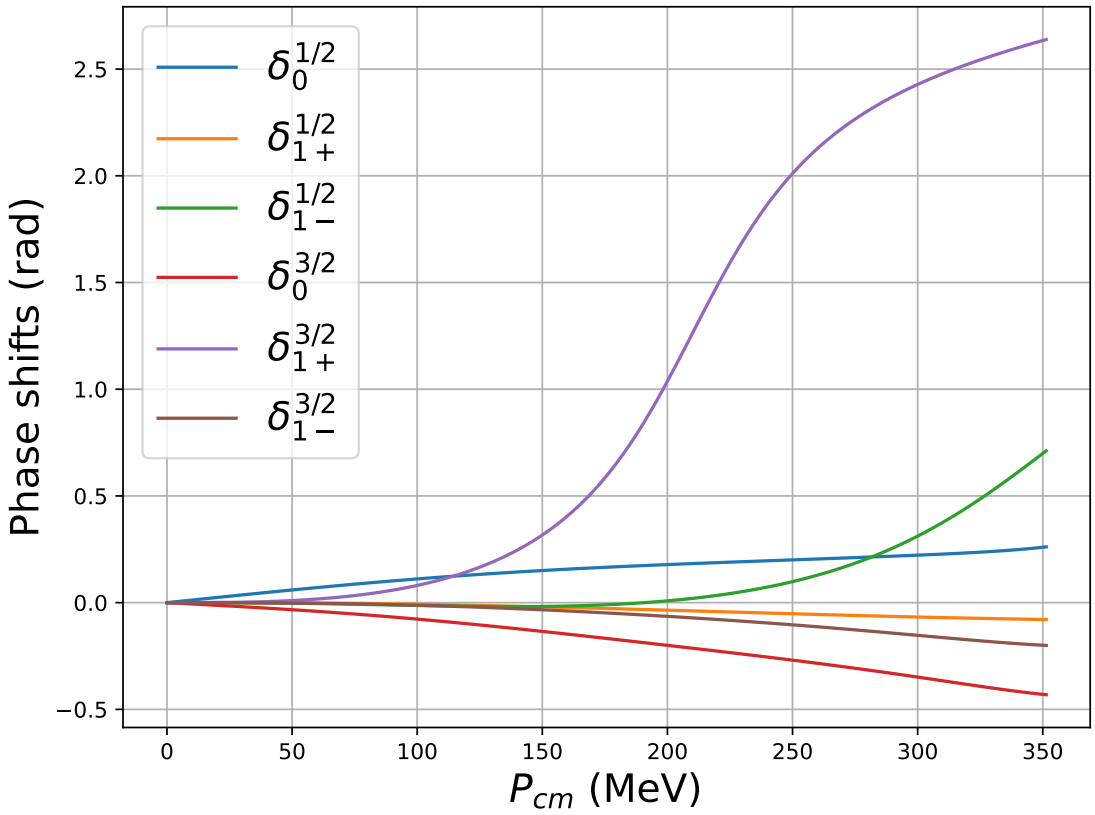


Figure 7: Phase shift vs Center of mass momentum

$$
\begin{aligned}
\Sigma_\pi(p) &= \int \frac{d^3k}{(2\pi)^3} \sum_{N=n,p} f_N[E_N(k)] V^{ps}_{N\pi}(p,k,\theta) \\
\Sigma_\pi(p) &= \int \frac{2\pi k^2 dk}{(2\pi)^3} \sum_{N=n,p} f_N[E_N(k)] \\
&\quad \int_0^\pi V^{ps}_{N\pi}(p,k,\theta) \sin\theta d\theta \\
\Sigma_\pi(p) &= \int \frac{2\pi k^2 dk}{(2\pi)^3} \sum_{N=n,p} f_N[E_N(k)] \\
&\quad \int_{\bar{m}(\frac{p}{m_\pi}-\frac{k}{m_N})}^{\bar{m}(\frac{p}{m_\pi}+\frac{k}{m_N})} V^{ps}_{N\pi}(p_{\rm cm}) \sin\theta \frac{d\theta}{dp_{\rm cm}} dp_{\rm cm} \\
\Sigma_\pi(p) &= \int \frac{2\pi k^2 dk}{(2\pi)^3} \sum_{N=n,p} f_N[E_N(k)] \\
&\quad \int_{\bar{m}(\frac{p}{m_\pi}-\frac{k}{m_N})}^{\bar{m}(\frac{p}{m_\pi}+\frac{k}{m_N})} \frac{2\pi}{\bar{m} p_{\rm cm}} \delta_{\rm sum}(p_{\rm cm}) \sin\theta \frac{d\theta}{dp_{\rm cm}} dp_{\rm cm}
\end{aligned}
\tag{31}
$$

$$
\begin{aligned}
\Sigma_\pi(p) &= \sum_{N=n,p} \int \frac{2\pi k^2 dk}{(2\pi)^3} f_N[E_N(k)] \\
&\quad \int_{\bar{m}(\frac{p}{m_\pi}-\frac{k}{m_N})}^{\bar{m}(\frac{p}{m_\pi}+\frac{k}{m_N})} \frac{2\pi}{\bar{m} p_{\rm cm}} \delta_{\rm sum}(p_{\rm cm}) \frac{p_{\rm cm} m_\pi m_N}{\bar{m}^2 pk} dp_{\rm cm} \\
\Sigma_\pi(p) &= \sum_{N=n,p} \frac{m_\pi + m_N}{\pi p \bar{m}^2} \int k dk f_N[E_N(k)] \\
&\quad \int_{\bar{m}(\frac{p}{m_\pi}-\frac{k}{m_N})}^{\bar{m}(\frac{p}{m_\pi}+\frac{k}{m_N})} \delta_{\rm sum}(p_{\rm cm}) dp_{\rm cm}
\end{aligned}
\tag{32}
$$

The first integration is done over $p_{\rm cm}$ for neutrons and protons separately. The second integration is done over k to get $\Sigma_\pi(p)$.

In our case the interaction term is absorbed into the distribution function as self energy and the energy density becomes

$$
\epsilon_\pi = \int \frac{p^2}{2\pi^2} E_\pi(p) f_\pi[E_\pi(p)] dp \tag{33}
$$

where $f_\pi[E_\pi(p)]$ is the distribution function for pions.

Entropy of a gas of bosons/fermions has the following covariant form.

$$\begin{aligned} S &= (2J+1)\int \frac{d\sigma^\mu p_\mu d^3p}{(2\pi)^3 p^0}\{-(2\pi)^3 f \ln[(2\pi)^3 f] \\ &\pm [1\pm(2\pi)^3 f]\ln[1\pm(2\pi)^3 f]\} \end{aligned} \tag{34}$$

this in our case becomes

$$\begin{aligned} S_\pi &= -\frac{1}{2\pi^2}\int p^2 dp\,(f_\pi[E_\pi(p)]\ln f_\pi[E_\pi(p)] \\ &- (1+f_\pi[E_\pi(p)])\ln\{1+f_\pi[E_\pi(p)]\}) \end{aligned} \tag{35}$$

The interaction term is absorbed into the distribution function as self-energy and the number density in our case is.

$$n_\pi = \int \frac{p^2 dp}{2\pi^2} f_\pi(E_\pi(p)) \tag{36}$$

depending on interacting or non-interacting pions, self-energy is included in the distribution function. For us, pions are interacting. For nucleons, the number density is

$$n_i = \int \frac{dk}{k^2}\frac{1}{\{1+e^{\beta[\epsilon_i(k)-\mu_i]}\}} \tag{37}$$

For non-interacting pions, a Bose-Einstein condensate would appear when $\mu_e > m_\pi$where $m_\pi = 139.6$ MeV. In the case of interacting pions, the situation is a bit different and in a medium governed by pseudo-potential, we have to minimize the self-energy in order to check for pion condensation. The current self-energy as a function of pion momentum p tends to have a single minimum in the hundreds of MeV. This translates to a minimum in the pion energy either at $p = 0$ or near the minimum of Σ_π. So we will search for the location of the potential minimum at finite momentum starting the minimum function near the minimum of Σ_π which should only have one minimum and another to search near zero.

If the minimum of $E_\pi(p)$ is less than μ_π, condensation occurs.

F.1 Pion Properties

For a given n_B and T, guess the n_p (proton density before considering interaction). Single particle nucleon energies are computed.

$$\epsilon_i(k) = m_i + \frac{k^2}{2m_i^*} + U_i(n_i, n_p, T) \tag{38}$$

Here $U_i(n_i, n_p, T)$ is the mean-field potential energy in eq. 5 of Ref. [35]. The chemical potentials μ_n and μ_p are obtained. For our case [30]

$$\nu_n = -\mu_n + U_n \text{ and } \nu_p = -\mu_p + U_p \tag{39}$$

The ν_i in Ref. [30] and U_i in Ref. [35] are the same.

The number densities n_e, n_μ, n_π are obtained from Fermi-Dirac distributions and Boltzmann distributions. Then the charge neutrality condition

$$n_p = n_e + n_\mu + n_\pi \tag{40}$$

is used to update the n_p value afterwards.

After computing n_π, ϵ_π and s_π are computed. The pion contribution to the pressure in our case is

$$P_\pi = Ts_\pi - \epsilon_\pi + n_\pi \mu_\pi \tag{41}$$

Vita

Satyajit Roy is the firstborn son of Sibdas and Mandira Roy. Satyajit was born and raised in West Bengal, India. Satyajit got his bachelor's and master's in physics when he was attending the Indian Institute of Science Education and Research (IISER), Kolkata. After coming to the United States, he joined the Department of Physics and Astronomy at the University of Tennessee, Knoxville (UTK) as a graduate student and a teaching assistant. In 2019, Satyajit joined Dr. Andrew Steiner's research group on nuclear astrophysics as a research assistant and has carried out analysis of neutron star cooling ever since. He recently earned his doctorate in nuclear physics.